Spring 2022

CRYSTAL PLASTICITY MODELING FOR PREDICTING LOAD REVERSALS IN DUAL PHASE STEELS AND ALUMINIUM ALLOYS: APPLICATIONS TO PREDICTING SPRINGBACK BEHAVIOR

Sowmya Daroju
University of New Hampshire, Durham

CRYSTAL PLASTICITY MODELING FOR PREDICTING LOAD REVERSALS IN DUAL
PHASE STEELS AND ALUMINIUM ALLOYS: APPLICATIONS TO PREDICTING
SPRINGBACK BEHAVIOR

BY

Sowmya Daroju

B.Tech in Mechanical Engineering, Jawaharlal Nehru Technological University, 2013

THESIS

Submitted to the University of New Hampshire

in Partial Fulfillment of

the Requirements for the Degree of

Master of Science

in

Mechanical Engineering

May, 2022

This thesis was examined and approved in partial fulfillment of the requirements for the degree of Master of Science in Mechanical Engineering by:

Marko Knezevic, Professor (Mechanical Engineering)

Igor Tsukrov, Professor (Mechanical Engineering)

Todd S. Gross, Professor (Mechanical Engineering)

Approval signatures are on file with the University of New Hampshire Graduate School

Table of Contents

ACKNOWLEDGEMENTS

I thank my advisor, Professor Marko Knezevic, for his continuous support, and guidance throughout my Master's research. I would also like to thank Professor Igor Tsukrov, and Professor Todd Gross for teaching me along the way and agreeing to be a part of my Master's defense committee. I would like to thank Professor Kuwabara for carrying out the load reversal experiments and providing the data, the major part of my thesis.

I would like to thank, Adnan Eghtesad, Feng Zhangxi (Jesse), Milovan Zecevic, and William Feather for their guidance, support and help throughout the way. I would like to acknowledge Milovan's work developing the EPSC code that was used to perform much of the research work presented in this thesis.

Lastly, I would like to thank all my fellow grad students, my parents, and my siblings for their continued support.

CRYSTAL PLASTICITY MODELING FOR PREDICTING LOAD REVERSALS IN DUAL
PHASE STEELS AND ALUMINIUM ALLOYS: APPLICATIONS TO PREDICTING
SPRINGBACK BEHAVIOR

BY

Sowmya Daroju

ABSTRACT

Numerical modeling of sheet metal forming is of growing interest for industry and academia.

Metal forming operations often involve non-monotonic deformation paths with frequent

unloading. This research explores the use of elasto-plastic self-consistent (EPSC) modeling in

predicting the monotonic and load reversal deformation of aluminum alloys, and dual-phase

steels. The EPSC model considers anisotropic elasticity, dislocation density-hardening, and intra

granular slip system-level backstress fields in addition to accounting for inter granular stress

fields; the detailed contribution of this helps in properly predicting the phenomena such as

unloading non-linearity, the Bauschinger effect (BE), and changes in hardening rates during

reversals. In this study the EPSC model is also linked with Finite element analysis software

ABAQUS in predicting the spring back profiles in hat- shaped draw bending for various

dualphase steels namely DP 780, DP 980, and DP 1180 which have various strengths based on

the percentage of martensite and ferrite content.

Chapter 1:

Experimental characterization and crystal plasticity modeling of dual-phase steels subjected to strain path reversals.

This chapter has been published in Mechanics of Materials as: *"Experimental characterization and crystal plasticity modeling of dual-phase steels subjected to strain path reversals"*, Sowmya Daroju, Toshihiko Kuwabara, and Marko Knezevic.

For this chapter, all the experimental results were provided by Professor Toshihiko Kuwabara, the simulated results were carried out in EPSC.

Experimental characterization and crystal plasticity modeling of dual-phase steels subjected to strain path reversals

Sowmya Daroju[a], Toshihiko Kuwabara[b], and Marko Knezevic[a,1]

[a]Department of Mechanical Engineering, University of New Hampshire, Durham, NH 03824,

USA

[b]Division of Advanced Mechanical Systems Engineering, Institute of Engineering, Tokyo

University of Agriculture and Technology, Tokyo 184-8588, Japan

Abstract

This paper is concerned with monotonic and load reversal deformation of four dual-phase (DP) 590, 780, 980, 1180 and one martensitic (MS) 1700 steel sheets. While the monotonic data are presented for all steels, the load reversal data are provided for DP 590, DP 780, and DP 1180. Particularities pertaining to the reversal deformation including the decreasing hardening rate during forward tension, a linear and then a non-linear unloading, followed by the Bauschinger effect, and a shift in the hardening rate during continuous straining were quantified and discussed as a function of loading history. Moreover, parameters such as the reloading stress differential, reloading softening stress, ratcheting strain, and unloading deviation stress were determined and

[*] Corresponding author at: University of New Hampshire, Department of Mechanical Engineering, 33 Academic Way, Kingsbury Hall, W119, Durham, New Hampshire 03824, United States. Tel.: 603 862 5179; fax: 603 862 1865.
E-*mail address*: marko.knezevic@unh.edu (M. Knezevic).

discussed as a function of martensite fraction. The data were interpreted and predicted using an elasto-plastic self-consistent (EPSC) crystal plasticity model incorporating anisotropic elasticity, a dislocation density based hardening law, and a slip system backstress law. The model parameters associated with the slip strengths of ferrite and martensite and backstress were established. This work demonstrated the ability of crystal plasticity modeling to account for the co-dependent nature of crystallographic slip in ferrite and martensite and the sources of hardening caused by history-dependent dislocation density evolution and backstress to predict not only monotonic but also hysteresis in plastic response during the forward-reversal cycles. The combination of comprehensive experimental data and modeling results allowed us to infer that the tradeoff between the magnitude of backstress per phase and the volume fraction of ferrite versus martensite per steel governs the unloading and subsequent yielding per steel, while the dissolution of dislocations facilitates capturing the hardening rates during load reversal deformation.

1. Introduction

Strain applied in the opposite direction with respect to that applied during prior straining gives rise to the load reversal deformation path. Such deformation path changes are often exerted on the material in metal forming processes (Hosford and Caddell, 1993). Upon the load reversal, the material first exhibits linear unloading, which is followed by non-linear unloading (Cullen and Korkolis, 2013; Deng et al., 2015; Wagoner et al., 2013; Yoshida et al., 2002). Next, the yield stress changes relative to that achieved at the end of prior straining. The phenomenon is referred to as the Bauschinger effect (BE) (Bauschinger, 1886). With continuous straining in the reverse direction, the hardening rate is usually smaller than that observed during prior straining. The phenomenon is referred to as the permanent softening (Hasegawa et al., 1975; Zang et al., 2013). The phenomena pertaining to the deformation involving load reversals are driven by plasticity induced microstructural evolution, as summarized below.

The first phenomenon upon load reversal is the unloading of a strained material (Deng et al., 2015; Pavlina et al., 2015; Sritharan and Chandel, 1997; Yoshida et al., 2002). The origin of the nonlinear portion of unloading is a re-emission of dislocations piled-up at grain and phase boundaries during forward straining (Mompiou et al., 2012; Sritharan and Chandel, 1997). The re-emission of these loosely-tangled dislocations in pile-ups is accompanied by the relaxation of micro-backstress fields emanating from the pile-ups (Sritharan and Chandel, 1997). During stress relaxation, these mobilized dislocations from the pile-ups quickly vanish contributing to an increase in the forest dislocation density causing strain hardening (Dotsenko, 1979; Kruml et al., 2008; Mohebbi et al., 2015).

The second phenomenon proceeding after the unloading is the BE. The primary origin of BE pertains to intra-granular backstress sources of incompatibilities between hard regions (e.g.

dislocation cell walls) and soft regions (e.g. cell interiors) (Demir and Raabe, 2010; Gough et al., 1927; Kassner et al., 2013; Mughrabi, 1983). The secondary origin of BE pertains to inter-granular backstress sources that develop due to the anisotropy between grains of different crystal orientation (Abel, 1987; Nieh and Nix, 1986; Stout and Rollett, 1990; Verma et al., 2011). Here, a softer grain surrounded by harder grains will undergo greater plastic deformation than the surrounding neighbors. Such incompatibilities in accommodating plastic strain cause the plastic strain gradients in the microstructure. The dislocations building up the gradients are referred to as the geometrically necessary dislocations (GNDs) (Bayley et al., 2006; Fleck et al., 1994). These long range internal stresses whether intra-granular or inter-granular acts against the applied loading. Upon the reversal of the loading direction, the backstress fields combine with the applied loading inducing a drop in the yield stress. Orowan's theory justifies the BE in crystals based on the reduction in the resistance to dislocation glide in the reverse motion from that during prior forward straining (Orowan, 1959). The reverse path is easier because any obstacles on the forward path have been overcome. The strain incompatibilities are greater in multi-phase materials between grains of different phases than in single-phase materials between grains of the same phase because of a larger strength differential between phases than between grains in the same phase. As a result, the backstress fields govern a greater portion of the local and overall mechanical behavior in multi-phase materials than in single-phase materials (Brown and Stobbs, 1971; Kadkhodapour et al., 2011; Nesterova et al., 2015; Taupin et al., 2013).

The third phenomenon following re-yielding is the permanent softening. The underlying cause of the phenomenon is a competition between the annihilation/dissolution of existing dislocations and buildup of new dislocations during deformation in the reverse direction (Kitayama et al., 2013; Stout and Rollett, 1990; Wilson et al., 1990). The effect is more pronounced in multi-phase

materials (Bate and Wilson, 1986; Gardey et al., 2005; Hasegawa et al., 1975; Wilson and Bate, 1986).

Modeling of forming processes involving load reversals requires material models capable of capturing the above summarized phenomena (Li et al., 2002; Sharma et al., 2021). A range of macroscopic plasticity models combining isotropic and kinematic hardening laws attempting to represent the above summarized deformation physics have been developed (Armstrong and Frederick, 1966; Chaboche and Rousselier, 1983; Chaboche, 1977; Chaboche, 2008; Hu et al., 1992; McDowell, 1992). These models, while computationally efficient and suitable to couple with the finite element method (FEM) codes, do not account for microstructural evolution and underlying dislocation processes and sources of backstress fields. Moreover, these models contain a large number of adjustable parameters whose identification is involved and often demands a set of complex mechanical tests (Feng et al., 2020; Smith et al., 2014). Since not microstructure sensitive, these models represent a specific material state and are best applicable to the loading conditions used in the model adjusting process.

Models based on crystal plasticity theory provide more flexibility to incorporate physics of deformation because these models consider crystallography of deformation mechanisms and can capture microstructural evolution and underlying elasto-plastic anisotropy. Besides, these models are not restricted to a given state of the material or a specific loading condition, and therefore are more robust and predictive than macroscopic plasticity models. A number of crystal plasticity models have been developed in the course of last few decades ranging from Taylor-type upper-bound models (Fromm et al., 2009; Taylor, 1938), mean-field self-consistent (SC) models (Lebensohn and Tomé, 1993; Turner and Tomé, 1994) to spatially resolved techniques such as crystal plasticity finite element (Kalidindi et al., 1992; Knezevic et al., 2014; Roters et al., 2010)

and Green's function fast Fourier transform formulations (Eghtesad et al., 2018a; Lebensohn et al., 2012). While the spatial models can be used for more detailed simulations accounting for grain-to-grain interactions, the Taylor-type and SC models are more computationally efficient and have proven effective in predicting the overall flow stress and evolution of texture in polycrystalline metals. Additionally, these models can serve as constitutive laws in the FEM modeling and simulations (Knezevic et al., 2013; Segurado et al., 2012). In such formulations, the spatial variations in deformation from point to point across the FEM model relax a particular homogenization assumptions (Feather et al., 2021).

A crystallography-based elasto-plastic self-consistent (EPSC) model featuring a dislocation-based hardening law and accounting for inter-granular stress fields and intra-granular backstress sources at the slip system level has been used to interpret the load reversal deformation of DP 590 (Zecevic et al., 2016). The model has also been successfully adjusted to model the elastic anisotropy of DP 590, DP 980, DP 1180, and MS 1700 steels (Cantara et al., 2019). The earlier works also determined fraction of martensite versus ferrite in these steels (Poulin et al., 2020; Zecevic et al., 2016). Combining these modeling and characterization advances, the present work measures and models the monotonic response of DP 590, DP 780, DP 980, DP 1180, and MS 1700 and the cyclic tension-compression response to large strains of DP 590, DP 780, and DP 1180 steels. The large body of mechanical data for DP steel sheets is presented and used to calibrate and validate the model. To initialize the model, neutron diffraction measurements of texture were performed. The fitting parameters of the model are calibrated for ferrite and martensite using partial data for two steels and fine-tuned while predicting the behavior of the remaining streels. Based on the predictions, the model is regarded as capable of modeling the elasto-plastic monotonic pre-loading to various strain levels followed by hysteresis in the plastic regime with

multiple forward-reversal cycles of the steels using a single set of fitting parameters per phase. In particular, the monotonic hardening, the non-linear unloading, the BE, and the changes in the hardening rates during strain reversals are predicted for every steel. The data, calculations, and insights pertaining to the deformation behavior of the steels are presented and discussed in the paper.

2. Materials and experiments

The materials investigated in this work are DP advanced high strength steel (AHSS) sheets of DP 590, DP 780, DP 980, DP 1180, and one martensitic steel sheet, MS 1700. The sheets were acquired from the United States Steel Corporation (US Steel). DP 590, DP 780, and DP 980 underwent the hot dip (HD) processing line, while DP1180 underwent the continuous annealing line (CAL). DP 590 and DP 780 were galvannealed (HDGA) coated. DP 980 was galvanized (HDGI) coated. DP 1180 and MS 1700 were bare. Chemical composition of the DP steels (wt%) is provided in Table 1. The thicknesses of the sheets were 1.3 mm, 1.4 mm, 1 mm, 1 mm, and 1 mm for DP 590, DP 780, DP 980, DP 1180, and MS 1700, respectively. These steel sheets are typically used for auto-body and structure applications.

The studied steels offer a compromise between strength and ductility as a result of their underlying microstructure that consists of a softer ferritic phase and a harder martensitic phase. While the former phase provides ductility, the latter phase provides the strengthening. Electron backscatter diffraction (EBSD) and secondary electrons (SE) imaging was performed in earlier work to characterize grain structure and phase fractions (Poulin et al., 2020). Volume fraction of martensite for the studied steels is given in Table 2.

The tradeoff between strength and ductility of these steels is governed by the volume fraction of these two phases (Calcagnotto et al., 2012; Ghaei et al., 2015; Gong et al., 2016; Kudzal et al., 2020; Ma et al., 2016; Woo et al., 2012; Zecevic et al., 2019). Further improvements are possible by phase distribution (Bhargava et al., 2018; Calcagnotto et al., 2011). The secondary effects influencing the behavior of these steels are due to grain size and crystallographic texture per phase. Local grain-level plasticity in these steels is highly inhomogeneous due to the contrasting characteristics of the constituent phases. For example, larger grains suitably oriented for slip deform plastically earlier than smaller grains of ferrite (Tasan et al., 2014). Additionally, plastic strain can localize in channels of ferrite between martensite regions as well as at martensite/ferrite phase interfaces (Kapp et al., 2011; Tasan et al., 2014; Woo et al., 2012; Yaddanapudi et al., 2021). Such localizations limit formability in sheet metal forming operations (Bhadeshia, 2002; Nikhare et al., 2011; Saeidi et al., 2015; Shi and Gelisse, 2006; Wagoner et al., 2009; Xue et al., 2016).

To evaluate the behavior of the steels in large strain cyclic tension-compression, experiments were performed relying on the testing setup and procedure developed in the earlier works (Kuwabara et al., 2009; Kuwabara et al., 2001; Verma et al., 2011). We only indicate that the strain was measured using a YFLA-2 (Tokyo Sokki Kenkyujo) high-elongation strain-gages. Additionally, tensile tests were performed according to the ASTM E-8 standard on an MTS Landmark 370 servo-hydraulic testing machine. During these experiments, the strain was measured using the VIC-2D Digital Image Correlation (DIC) system. The DIC strain measurements were validated with those of a mechanical extensometer. A nominal strain rate of 5×10^{-4} /s was used for all tests. All tests were performed at room temperature.

Table 1. Chemical composition of DP steels (wt%).

	C	Mn	P	S	Si	Cu	Ni	Cr	Mo
DP 590	0.073	1.97	0.014	0.006	0.017	0.04	0.01	0.2	0.172
DP 780	0.1	2.163	0.015	0.006	0.014	0.03	0.01	0.26	0.332
DP 980	0.11	2.411	0.013	0.005	0.013	0.027	0.009	0.255	0.385
DP 1180	0.168	2.222	0.015	0.0053	1.421	0.021	0.007	0.036	0.013

	Sn	Al	Zr	V	Cb	Ti	B	N_2
DP590	0.002	0.045		0.001			0.0001	0.005
DP780	0.003	0.048		0.001	0.003	0.001	0.0001	0.006
DP980	0.006	0.049	0.005	0.011	0.004	0.002	0.0001	0.0033
DP1180	0.007	0.051	0.005	0.012	0.007	0.039	0.0004	0.0086

Table 2. Volume fraction of martensite for the studied steels.

DP 590	DP 780	DP 980	DP 1180	MS 1700
7.7%	34%	39%	45%	85%

3. Material model

The EPSC model was originally developed in (Turner and Tomé, 1994), while the particular version from (Zecevic et al., 2016) is used here to interpret the load reversal deformation of DP steels. The model treats a polycrystal as a collection of ellipsoidal grains with a specific crystallographic orientation and a volume fraction. Overall properties of the polycrystal are obtained using the SC homogenization scheme in which each grain is considered as an elasto-

plastic inclusion in the homogeneous-equivalent-medium (HEM). The properties of the HEM are those sought properties of the polycrystal. In the model description that follows, we use "·" notation for a contracted (dot) product and "⊗" notation for an uncontracted (tensor) product.

The strain rate and Jaumann stress rate at the polycrystal level are linked using a linear relationship

$$\hat{\boldsymbol{\sigma}} = \mathbf{L}\dot{\boldsymbol{\varepsilon}}, \tag{1}$$

with $\mathbf{L}$ denoting the instantaneous elasto-plastic stiffness tensor of the overall polycrystal. The solution for $\mathbf{L}$ is obtained iteratively using the standard SC procedure (Turner and Tomé, 1994), which ensured the stress equilibrium and strain compatibility (Eshelby, 1957). A strain rate at the grain-level and that at the overall polycrystal-level are related using

$$\dot{\boldsymbol{\varepsilon}}^c = \mathbf{A}^c\dot{\boldsymbol{\varepsilon}}, \tag{2}$$

where $\mathbf{A}^c = \left(\mathbf{L}^c + \mathbf{L}^{c^*}\right)^{-1}\left(\mathbf{L}^{c^*} + \mathbf{L}\right)$ is the localization tensor based on $\mathbf{L}^c$, which is the instantaneous crystal, c, elasto-plastic stiffness tensor and $\mathbf{L}^{c^*} = \mathbf{L}\left(\mathbf{S}^{c-1} - \mathbf{I}\right)$ is the effective stiffness tensor. The effective stiffness relates the stress and strain rate deviations between grains and HEM as $(\hat{\boldsymbol{\sigma}}^c - \hat{\boldsymbol{\sigma}}) = -\mathbf{L}^{c^*}(\dot{\boldsymbol{\varepsilon}}^c - \dot{\boldsymbol{\varepsilon}})$. $\mathbf{S}^c$ is the symmetric portion of the Eshelby tensor and $\mathbf{I}$ is the fourth rank identity. The polycrystal stress and strain rate are the volume average of the corresponding quantities at the grain-level

$$\hat{\boldsymbol{\sigma}} = \langle \hat{\boldsymbol{\sigma}}^c \rangle, \tag{3}$$

and

$$\dot{\boldsymbol{\varepsilon}} = \langle \dot{\boldsymbol{\varepsilon}}^c \rangle. \tag{4}$$

The expression for $\mathbf{L}$ is then

$$\mathbf{L} = \langle \mathbf{L}^c \mathbf{A}^c \rangle \langle \mathbf{A}^c \rangle^{-1}. \tag{5}$$

Given the Jaumann stress rate, the Cauchy stress rate is $\dot{\boldsymbol{\sigma}} = \hat{\boldsymbol{\sigma}} + \langle \mathbf{W}^c \boldsymbol{\sigma}^c \rangle - \langle \boldsymbol{\sigma}^c \mathbf{W}^c \rangle = \mathbf{L}\dot{\boldsymbol{\varepsilon}} + \langle \mathbf{W}^c \boldsymbol{\sigma}^c \rangle - \langle \boldsymbol{\sigma}^c \mathbf{W}^c \rangle$, where $\mathbf{W}^c$ is the lattice spin tensor of a crystal, c.

The constitutive relation at the grain-level is

$$\hat{\boldsymbol{\sigma}}^c = \mathbf{C}^c(\dot{\boldsymbol{\varepsilon}}^c - \sum_s \mathbf{m}^{c,s} \dot{\gamma}^{c,s}) - \boldsymbol{\sigma}^c tr(\dot{\boldsymbol{\varepsilon}}^c), \tag{6}$$

with $\mathbf{C}^c$ as the grain-level elastic stiffness tensor calculated based on the single crystal elastic constants established in (Cantara et al., 2019) and $\sum_s \mathbf{m}^{c,s} \dot{\gamma}^{c,s}$ as the plastic strain rate expressed as the sum over the slip system, s, shear strain rates, $\dot{\gamma}^{c,s}$. Here, $\mathbf{m}^{c,s} = 0.5(\mathbf{b}^{c,s} \otimes \mathbf{n}^{c,s} + \mathbf{n}^{c,s} \otimes \mathbf{b}^{c,s})$ is the symmetric part of the Schmid tensor with $\mathbf{b}^{c,s}$ and $\mathbf{n}^{c,s}$ are unite vectors representing the slip system direction and slip system plane normal, respectively. Like at the polycrystal level, the linear relationship between the grain strain rate and Jaumann stress rate is

$$\hat{\boldsymbol{\sigma}}^c = \mathbf{L}^c \dot{\boldsymbol{\varepsilon}}^c, \tag{7}$$

where $\mathbf{L}^c$ is:

$$\mathbf{L}^c = \mathbf{C}^c - \mathbf{C}^c \sum_s \mathbf{m}^{c,s} \otimes \left(\sum_{s'} (X^{ss'})^{-1} \mathbf{m}^{c,s'} (\mathbf{C}^c - \boldsymbol{\sigma}^c \otimes \mathbf{i}) \right) - \boldsymbol{\sigma}^c \otimes \mathbf{i}, \tag{8}$$

with:

$$X^{ss'} = h^{ss'} + h_{bs}^{ss'} + \mathbf{C}^c \cdot \mathbf{m}^{c,s} \otimes \mathbf{m}^{c,s'}. \tag{9}$$

To activate a slip system in EPSC, $\mathbf{m}^{c,s} \cdot \boldsymbol{\sigma}^c - \tau_{bs}^{c,s} = \tau_c^{c,s}$ and $\mathbf{m}^{c,s} \cdot \hat{\boldsymbol{\sigma}}^c - \dot{\tau}_{bs}^{c,s} = \dot{\tau}_c^{c,s}$ conditions need to be satisfied. In the first condition, the resolved shear stress corrected for the backstress, $\tau_{bs}^{c,s}$, approaches the value of slip resistance, $\tau_c^{c,s}$, while in the second condition, the stress is enforced to remain on the crystal yield surface evolving with hardening. The slip

resistance, $\dot{\tau}_c^{c,s}$, and backstress, $\dot{\tau}_{bs}^{c,s}$, rates are linked with shearing rates, $\dot{\gamma}^{c,s}$, using (Zecevic and Knezevic, 2015):

$$\dot{\tau}_c^{c,s} = \sum_{s'} h^{ss'} \dot{\gamma}^{c,s'}, \tag{10}$$

$$\dot{\tau}_{bs}^{c,s} = \sum_{s'} h_{bs}^{ss'} \dot{\gamma}^{c,s'}, \tag{11}$$

with $h^{ss'}$ and $h_{bs}^{ss'}$ being the hardening and the backstress matrices, respectively. Expressions for $h^{ss'}$ and $h_{bs}^{ss'}$ can readily be derived from the hardening and backstress evolution laws, which will be described below.

In order to calculate the reorientation of crystal orientations in both ferrite and martensite grains, the lattice spin tensor, $\mathbf{W}^c$, is used and calculates using

$$\mathbf{W}^c = \mathbf{W}^{app} + \mathbf{\Pi}^c - \mathbf{W}^{p,c} \tag{17}$$

with $\mathbf{W}^{app}$ as the applied rotation rate, $\mathbf{\Pi}^c$ as the antisymmetric part of the Eshelby tensor (Lebensohn and Tomé, 1993), and $\mathbf{W}^{p,c}$ as the plastic spin, which is obtained from the shearing rates

$$\mathbf{W}^{p,c} = \sum_s \mathbf{q}^{c,s} \dot{\gamma}^{c,s}, \tag{18}$$

with $\mathbf{q}^{c,s} = 0.5(\mathbf{b}^{c,s} \otimes \mathbf{n}^{c,s} - \mathbf{n}^{c,s} \otimes \mathbf{b}^{c,s})$.

3.1 Hardening law

In the description below, the superscript α denotes slip modes i.e. $\alpha = 1$ for $\{110\}\langle 1\bar{1}1\rangle$ and $\alpha = 2$ for $\{112\}\langle 11\bar{1}\rangle$, whereas the superscripts *s* and *s'* denote the individual slip systems in the

modes. Note that the slip systems in EPSC have positive *s+* and negative *s-* directions i.e. have the same slip plane but opposite directions.

The slip resistance evolves from an initial value, τ_0^α, that includes the Peierls stress, the barrier grain size contribution, and the initial content of dislocations contribution per slip system based on the thermally activated rate of dislocation storage

$$\tau_c^s = \tau_0^\alpha + \tau_{forest}^s + \tau_{deb}^\alpha, \tag{19}$$

where, τ_{forest}^s is a forest dislocations term and τ_{deb}^α is a debris dislocations term. The former term is modeled using the Taylor-type relation (Kitayama et al., 2013; Taylor, 1992)

$$\tau_{for}^s = b^\alpha \chi \mu^\alpha \sqrt{\rho_{tot}^s + L \sum_{s'} \rho_{tot}^{s'}}, \tag{20}$$

with $b^\alpha = 2.48 \ 10^{-10} \ m$ as the Burgers vector per slip mode, $\chi = 0.9$ as the dislocation interaction parameter, ρ_{tot}^s as the total forest density of dislocations, and L as the latent hardening parameter set to 1.05. The latter term relies on the extended Taylor-type relation (Madec et al., 2003)

$$\tau_{deb}^\alpha = 0.086 \ \mu^\alpha b^\alpha \sqrt{\rho_{deb}} log \left(\frac{1}{b^\alpha \sqrt{\rho_{deb}}} \right), \tag{21}$$

where ρ_{deb} is the debris density of dislocations.

The evolution of dislocation densities is such that the deformation-history-dependent directionality is accounted for. To this end, a fraction of accumulated dislocations are considered as reversible. The total dislocation density per slip system consists of

$$\rho_{tot}^s = \rho_{for}^s + \rho_{rev}^{s^+} + \rho_{rev}^{s^-}, \tag{22}$$

with ρ_{for}^s as the forward dislocation density shared by both directions s^+ and s^- and $\rho_{rev}^{s^+}$ and $\rho_{rev}^{s^-}$ as the reversible dislocation densities on s^+ and s^-, respectively. The evolution of forward dislocations follows the Kocks-Mecking law (Kocks and Mecking, 1981)

$$\frac{\partial \rho_{for}^s}{\partial \gamma^s} = (1-p)k_1^\alpha \sqrt{\rho_{for}^s + \rho_{rev}^s} - k_2^\alpha(\dot{\varepsilon}, T)\rho_{for}^s, \qquad (23)$$

with k_1^α as a fitting coefficient controlling the rate of dislocation generation, while k_2^α is a rate-sensitive coefficient controlling the rate of dynamic recovery (Beyerlein and Tomé, 2008), and p is a reversibility constant from 0 to 1 but taken as unity. Given that the parameter divides the increment in the total storage ($k_1^\alpha \sqrt{\rho_{for}^s + \rho_{rev}^s}\, d\gamma^s$) in a forward ($(1-p)k_1^\alpha \sqrt{\rho_{for}^s + \rho_{rev}^s}\, d\gamma^s$) increment and a reversible ($pk_1^\alpha \sqrt{\rho_{for}^s + \rho_{rev}^s}\, d\gamma^s$) increment, the value of unity makes the increment solely reversible. The value of unity is justified by the low accumulated strain level in all simulations presented later in the paper (Kitayama et al., 2013; Zecevic and Knezevic, 2015). While ρ_{for}^s is independent of the shearing direction, ρ_{rev}^s is the density associated with the shearing direction i.e. if $d\gamma^{s^+} > 0$ then $\rho_{rev}^s = \rho_{rev}^{s^+}$, and if $d\gamma^{s^-} > 0$ then $\rho_{rev}^s = \rho_{rev}^{s^-}$ as

(If $d\gamma^{s^+} > 0$)

$$\frac{\partial \rho_{rev}^{s^+}}{\partial \gamma^s} = pk_1^\alpha \sqrt{\rho_{for}^s + \rho_{rev}^s} - k_2^\alpha(\dot{\varepsilon}, T)\rho_{rev}^{s^+}, \qquad (24)$$

$$\frac{\partial \rho_{rev}^{s^-}}{\partial \gamma^s} = -k_1^\alpha \sqrt{\rho_{for}^s + \rho_{rev}^s} \left(\frac{\rho_{rev}^{s^-}}{\rho_0^s}\right)^m, \qquad (25)$$

with m as a coefficient controlling rate of dislocation recombination, set here to 0.5 (Wen et al.) and ρ_0^s as the density at the shear reversal on the sth slip system (Kitayama et al., 2013). For $d\gamma^{s^-} > 0$, the increments in $\rho_{rev}^{s^-}$ and $\rho_{rev}^{s^+}$ is calculated in an analogues manner to the above

equations. The initial conditions are $\rho_{for}^{s}(\gamma^s = 0) = \rho_{initial}^{s}$, $\rho_{rev}^{s^+}(\gamma^s = 0) = 0$ and $\rho_{rev}^{s^-}(\gamma^s = 0) = 0$.

The coefficient k_2^α is obtained using

$$\frac{k_2^\alpha}{k_1^\alpha} = \frac{\chi b^\alpha}{g^\alpha}\left(1 - \frac{k_B T}{D^\alpha (b^\alpha)^3} ln\left(\frac{\dot{\varepsilon}}{\dot{\varepsilon}_0}\right)\right), \tag{26}$$

where, k_B, $\dot{\varepsilon}_0$, g^α and D^α are constants: the Boltzmann constant, a reference strain rate set to 10^7 s^{-1}, and two fitting constant of an effective activation enthalpy and a drag stress, respectively. An increment of the debris development with the rate of recovery is

$$d\rho_{deb} = \sum_s q^\alpha b^\alpha \sqrt{\rho_{deb}} k_2^\alpha \rho_{tot}^s \left| d\gamma^{s'} \right|, \tag{27}$$

where q^α is a dislocation recovery rate fitting constant that removes a fraction of α-type dislocations that do not annihilate to become debris.

During forward tensile deformation, the dislocations mostly piled up close to obstacles such as phase or grain boundaries (Yaddanapudi et al., 2021). A strong BE can develop in steels develops in part as a consequence of easy annihilation of these dislocations formed during prior straining upon strain reversal (Gardey et al., 2005; Wilson and Bate, 1986). The effect is inferred from a decrease in hardness and shrinkage in the diffraction peak widths upon strain reversal (Wilson and Bate, 1986). At the strain reversal, generation of dislocations is momentarily retarded because a fraction of loosely-tangled stored dislocations easily glide in the reverse direction (Beyerlein, 2008). The stress relaxation takes place in which the piled-up dislocations rearrange themselves toward their equilibrium position along with the annihilation of mobile dislocations. These observations of an instantaneous decrease in dislocation density at the strain reversal is an important mechanism for the model along with the dislocation density evolution law. Hence, a fraction of total dislocation density is annihilated upon strain reversals. Continuous reloading of

the relaxed sample proceeds with the dislocation unpinning mechanisms with decline in annihilation and increase in multiplication of dislocations (Prasad et al., 2020).

3.2 Backstress law

Plastic deformation of DP steels initiates in the ferrite phase, while the martensite regions remain elastic (Gong et al., 2016). GNDs start to accumulate around the martensite regions inducing a strain gradient. These GNDs and any heterogeneous distribution of stored dislocations are sources of localized hardening and backstress fields (Nesterova et al., 2015). The stress field arising from GNDs will cause traction acting around martensite regions varying with the distance from the martensite. While the overall volume average stress equilibrates to zero, locally a non-zero value of backstress field is present in the ferrite and martensite phases entering the volume average stress (Brown and Stobbs, 1971). As dislocation density in the ferrite phase increases with plastic strain, dislocation structures develop (Yaddanapudi et al., 2021). Concurrently, GNDs continue to accumulate at these structures ensuring compatible deformation. Hence, in addition to backstress fields from GNDs around the martensite regions, there are backstress fields present inside ferrite grains influencing the grain-level plastic deformation. The volume average of these backstress fields also vanish over grains (Mughrabi, 2001).

Strain gradient plasticity model, which calculate backstress fields from GND calculations have been developed within the crystal plasticity finite element frameworks (Evers et al., 2004; Ma et al., 2006a, b, 2007). While higher order SC formulations also exist (Zecevic et al., 2017), the gradients in the model considered here exits only between the grain and the HEM. Since GNDs are not calculated in the model, a phenomenological law is adopted here to approximate the slip system backstress development with plastic strain giving rise to the kinematic hardening.

17

Formulation in which the backstress evolves with the plastic strain on individual slip systems are known as self-internal backstress formulations. A number of similar approaches exist in the literature (Bayley et al., 2006; Beyerlein and Tomé, 2007; Choi et al., 2013; Goh et al., 2003; Harder, 1999; Li et al., 2014; Wollmershauser et al., 2012; Xu and Jiang, 2004; Zecevic and Knezevic, 2015). The advantages of the backstress law used in this work is in its accuracy, simplicity and computational efficiency.

As described earlier, a slip system activates after $\mathbf{m}^s \cdot \boldsymbol{\sigma} - \tau_{bs}^s = \tau_c^s$ condition is fulfilled. Clearly, the condition is governed in part by the evolution of backstress. In our formulation, the backstress evolution law is for individual slip systems in ferrite grains, while the backstress on individual slip systems in martensite grains is obtained from the condition that the volume average of backstress always vanishes.

The backstress calculation in ferrite begins by calculating the backstress tensor per slyp system following the implementation presented in (Harder, 1999)

$$\boldsymbol{\sigma}_{bs}^{c,s,f} = (\mathbf{b}^{c,s} \otimes \mathbf{n}^{c,s} + \mathbf{n}^{c,s} \otimes \mathbf{b}^{c,s})\tau_{bs,sys}^s = 2\mathbf{m}^{c,s}\tau_{bs,sys}^s \,, \tag{28}$$

with $\boldsymbol{\sigma}_{bs}^{c,s,f}$ as a backstress tensor and $\tau_{bs,sys}^s$ as a backstress on the slip system. Then the grain backstress tensor is a summation over individual slip systems

$$\boldsymbol{\sigma}_{bs}^{c,f} = 2 \sum_{s'} \mathbf{m}^{c,s'} \tau_{bs,sys}^{s'} \,. \tag{29}$$

The slip system backstress is a resolved shear stress from the grain level backstress tensor

$$\tau_{bs}^s = \mathbf{m}^{c,s} \cdot \boldsymbol{\sigma}_{bs}^{c,f} = \tau_{bs,sys}^s + 2 \sum_{s'} \mathbf{m}^{c,s} \cdot \mathbf{m}^{c,s'} \tau_{bs,sys}^{s'} \,, \tag{30}$$

with the sum going over all active slip systems and $s' \neq s$.

Ferrite grains must deform plastically to give rise to backstress. The evolution law for backstress during plastic shearing in s^+ direction $(d\gamma^{s^+} > 0)$ is

$$\tau_{bs,sys}^{s^+} = \tau_{bs}^{sat}\left(1 - \exp\left(-\nu\gamma^{s^+}\right)\right), \tag{31}$$

$$\tau_{bs,sys}^{s^-} = -A\tau_{bs,sys}^{s^+}, \tag{32}$$

where $\tau_{bs,sys}^{s^+}$ and $\tau_{bs,sys}^{s^-}$ are individual backstresses in the two contrary directions per slip system. The law involves τ_{bs}^{sat} as a fitting parameter representing a saturation value for backstress, and A and ν as the additional fitting parameters, while γ^{s^+} is the shear strain accumulated on the sth slip system. Upon the load reversal, a system that was active during prior straining, s^+, unloads and activates in the reverse direction, i.e. s^-. Given that now $d\gamma^{s^-} > 0$, the evolution law is

$$\tau_{bs,sys}^{s^-} = -(A+1)\tau_{bs0}^{s^+} exp\left(-\frac{\gamma^{s^-}}{\gamma_b}\right) + \tau_{bs0}^{s^+}, \tau_{bs}^{s^+} = -\frac{1}{A}\tau_{bs}^{s^-} \ if \ \tau_{bs}^{s^-} < 0, \tag{33}$$

$$\tau_{bs,sys}^{s^-} = \tau_{bs}^{sat}(1 - exp(-\nu\gamma^{s^-})), \tau_{bs}^{s^+} = -A\tau_{bs}^{s^-} \ if \ \tau_{bs}^{s^-} > 0 \tag{34}$$

with $\tau_{bs0}^{s^+}$ as the value of backstress at the point of the reversal and γ_b is an additional fitting parameter. The backstress tensor varies from grain-to-grain with a net volume average of $\langle\dot{\boldsymbol{\sigma}}_{bs}^{c,f}\rangle$ (Brown and Stobbs, 1971).

Note that the rate forms of the equations are needed for $\mathbf{m}^{c,s} \cdot \hat{\boldsymbol{\sigma}}^c - \dot{\tau}_{bs}^{c,s} = \dot{\tau}_c^{c,s}$ as well as for the derivative $\frac{\partial\tau_{bs,sys}^s}{\partial\gamma^s}$ i.e. for the backstress matrix, $h_{bs}^{ss'}$. The rate forms are

$$\dot{\boldsymbol{\sigma}}_{bs}^{c,f} = 2\sum_{s'}\mathbf{m}^{c,s'}\dot{\tau}_{bs,sys}^{s'}, \tag{35}$$

$$\dot{\tau}_{bs}^s = \dot{\tau}_{bs,sys}^s + 2\sum_{s'}\mathbf{m}^{c,s} \cdot \mathbf{m}^{c,s'}\dot{\tau}_{bs,sys}^{s'} \ and \ s' \neq s, \tag{36}$$

with $\dot{\tau}_{bs,sys}^s = \frac{\partial\tau_{bs,sys}^s}{\partial\gamma^s}\dot{\gamma}^s$.

The backstress rate in martensite regions is defined using the volume average of backstress rate in ferrite phase, $\langle \dot{\boldsymbol{\sigma}}_{bs}^{c,f} \rangle$. Given that the overall backstress in the sample vanishes, the rate of backstress in martensite is

$$\langle \dot{\boldsymbol{\sigma}}_{bs}^{mr} \rangle = -\frac{V_f}{V_m} \langle \dot{\boldsymbol{\sigma}}_{bs}^{c,f} \rangle \tag{37}$$

with V_f and V_m as the fractions of ferrite and martensite phases, respectively. The backstress on slip systems in martensite grains is

$$\dot{\tau}_{bs}^{c,s,m} = \mathbf{m}^{c,s} \cdot \langle \dot{\boldsymbol{\sigma}}_{bs}^{mr} \rangle. \tag{38}$$

In summary, $\tau_{bs}^{s^+}$, acts opposite from the resolved shear stress on s^+, i.e. $\mathbf{m}^{s^+} \cdot \boldsymbol{\sigma} - \tau_{bs}^{s^+} = \tau_c^s$. Evidently $\tau_{bs}^{s^+}$ lowers the activation stress. Concurrently, $\tau_{bs}^{s^-}$ aids the activation stress on the slip system s^-, i.e. $\mathbf{m}^{s^-} \cdot \boldsymbol{\sigma} - \tau_{bs}^{s^-} = \tau_c^s$. These kinematic effects are the micro-plasticity processes primarily influencing the non-linear unloading and BE.

4. Results

This section begins by presenting the experimental results including flow stress and texture data and then continues with presenting the results of modeling including the model calibration and verification.

4.1 Experimental results for strain reversal tests

Figure 1 shows measured true stress-true strain curves during tension-compression-tension reversals. The first loading is forward tension to a given strain level. The second loading is compression to zero strain (1st reversal). The third loading is tension to fracture (2nd reversal). The materials exhibit the decreasing hardening rate during the forward tension, which is typical for

metals in which the plasticity is carried out by crystallographic slip. At the 1st reversal, the materials show an initial linear portion and then a non-linear portion of unloading. Macro-yield points during unloading at approximately 0.001 offset are indicated (σ_U). The pre-strain level in forward loading increases the magnitude of macro-yield stress, while the extent of the linear elastic unloading is approximately constant. The extent of the non-linear unloading is enhanced with strength of the steels (Bate and Wilson, 1986; Beyerlein, 2008). The reduction of the yield points between the initial straining and reverse straining is termed as transient softening. The mechanism is equivalent to the BE - the resistance to dislocation motion in the reverse sense is less than in forward straining. Following the transient softening is the permanent softening, which is a lowering of the stress-strain curves when the reverse stress-strain is plotted in the stress direction the same as the prior straining. These phenomena are depicted in the primed figures of Figure 1. The permanent softening phenomenon was first described in (Hasegawa et al., 1975) during tension-compression loading and also during forward-reverse simple shear loading in (Gracio et al., 2004). The origin of transient and permanent softening is in the backstress and annihilation of dislocations after reversing the glide directions during loading in the reverse direction. Like non-linear unloading, these phenomena are enhanced with strength.

Figure 2 shows comparisons between the forward tension and the 1st and 2nd reversals to observe the yielding differentials and subsequent hardening rates. As is evident, the transients after the 1st reversal are larger than the transients after the 2nd reversal. As the elasto-plastic transition upon the reversals (1st and the 2nd) is prolonged, the strain hardening rates are reduced compared to those during the forward tension. Although reduced, the strain hardening in compression of DP 590 surpasses that in tension causing positive yield differentials. The positive yield differential increases with pre-strain. The yield differentials for DP 780 and DP 1180 appear negative. The

origin of these reloading yield stress differentials is also in the backstress and annihilation of dislocations, as will be described later. Upon macroscopic re-yielding, the rate of strain hardening is restored. The curves after the 2nd reversal evolve towards the forward tension curves.

4.2 Texture characterization

The present work uses the two-phase EPSC constitutive law enhanced for a dislocation density law and a backstress law to predict and interpret the above-described phenomena. To initialize the model, in addition to phase fractions, texture is needed. To this end, the measurements of texture were carried out on initial samples of every steel using the High Pressure Preferred Orientation (HIPPO) beam at the pulsed neutron spallation source at Los Alamos National Laboratory, LANSCE. It is a time-of-flight neutron diffractometer for bulk texture characterization of metals at ambient and non-ambient (pressure, temperature, and load) conditions (Wenk et al., 2003). Unlike EBSD, texture measured using neutron diffraction is averaged over mm^3 to cm^3 volumes owing to the deep penetration of thermal neutrons into the metals, combined with a large beam spot sizes of ~0.1–1 cm^2. The count time for the present measurements was approximately 20 minutes at a proton current of 100 microA. Many inverse pole figures (i.e. in 135 sample directions) are measured to ensure a sufficient coverage for fiting an orientation distribution function (ODF) in a concurrent Rietveld refinement of 135 patterns, including also parameters such as lattice parameters (Wenk et al., 2010). Note that both martensite and ferrite are contained in the measurements as their diffraction peaks overlap. The ODF analyses of the data were done using MAUD (Wenk et al., 2010) with 7.5 degree resolution and the pole figures are plotted in MTEX (Bachmann et al., 2010). Figure 3 shows measured pole figures visualizing the initial texture in the steels. Texture in the steels is a typically reported orthotropic rolled texture for body-

centered cubic (BCC) metals, where the crystal orientations are concentrated around the γ-fiber and the α-fiber (Bhattacharyya et al., 2015; Holscher et al., 1994; Kocks et al., 1998). The texture intensity reduces with the fraction of martensite.
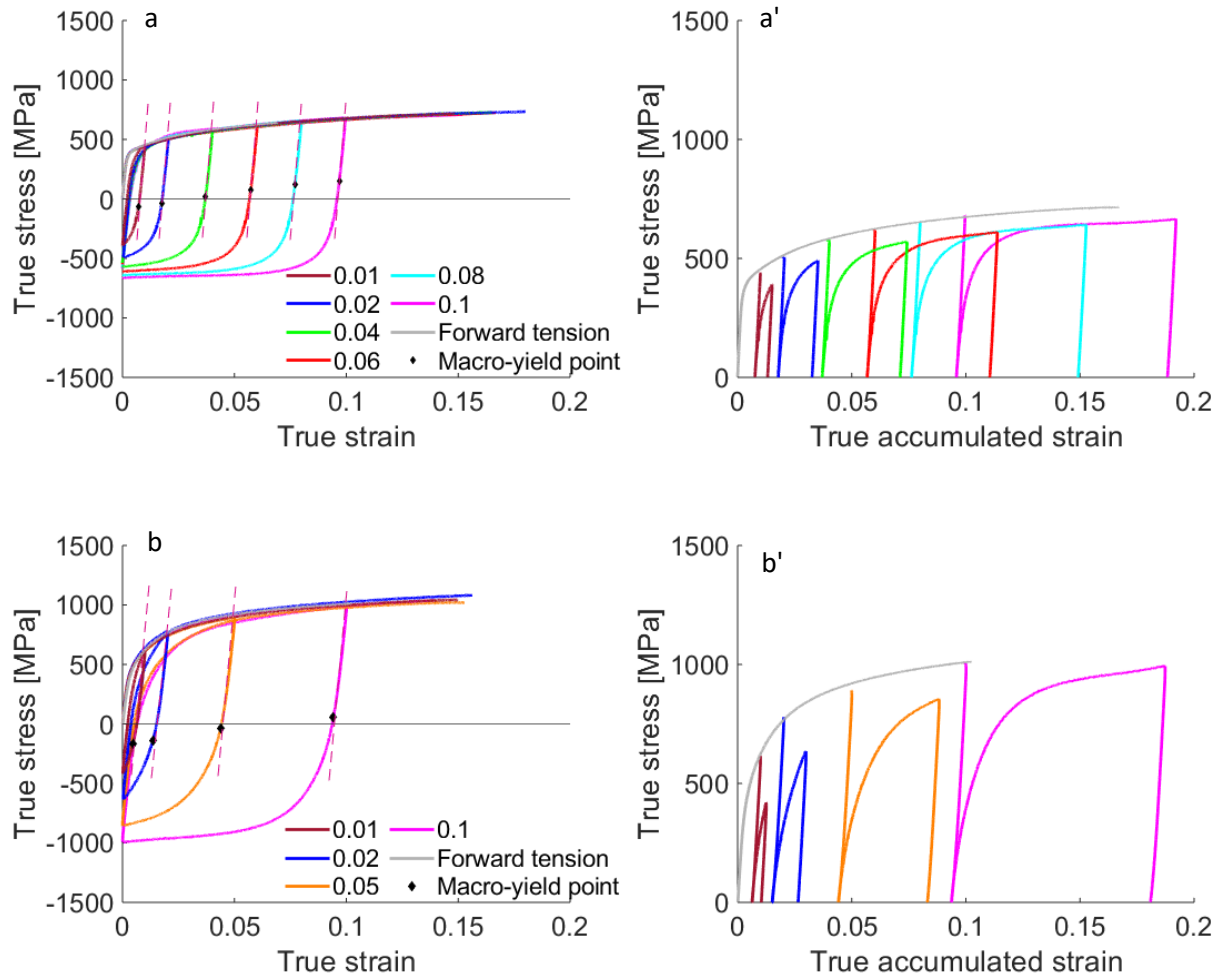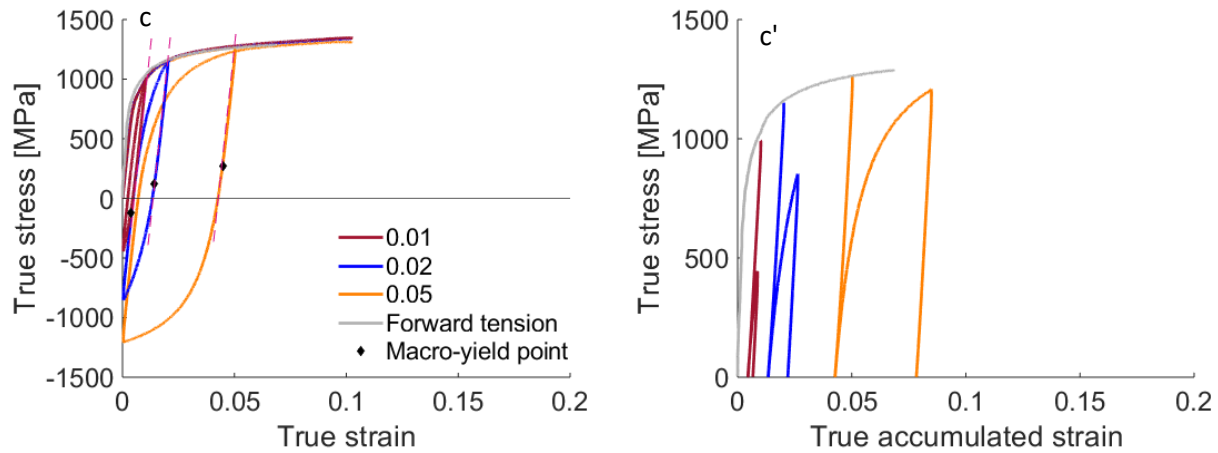
Figure 1. True stress–true strain curves during strain path reversals at several large strain levels for (a) DP 590, (b) DP 780, and (c) DP 1180 measured along the rolling direction (RD). Macro-yield points during unloading at approximately 0.001 offset are indicated (σ_U). Comparison of forward tension versus the 1st reversal curves as a function of accumulated true strain showing drops in the flow stress i.e. the permanent softening effect upon reversals for (a') DP 590, (b') DP 780, and (c') DP 1180. Legends are shown in the 'unprimend' plots and they apply to the corresponding 'primed' plots.
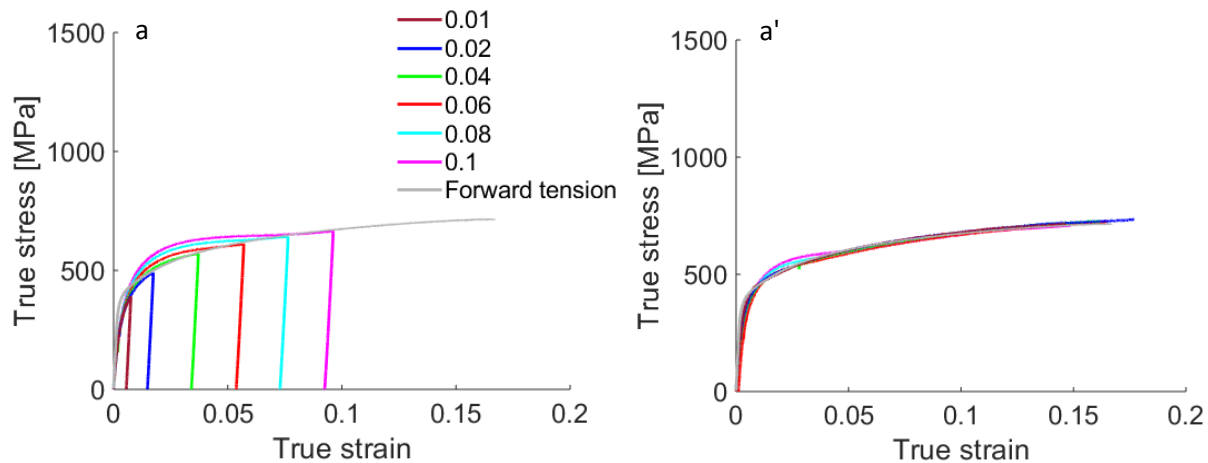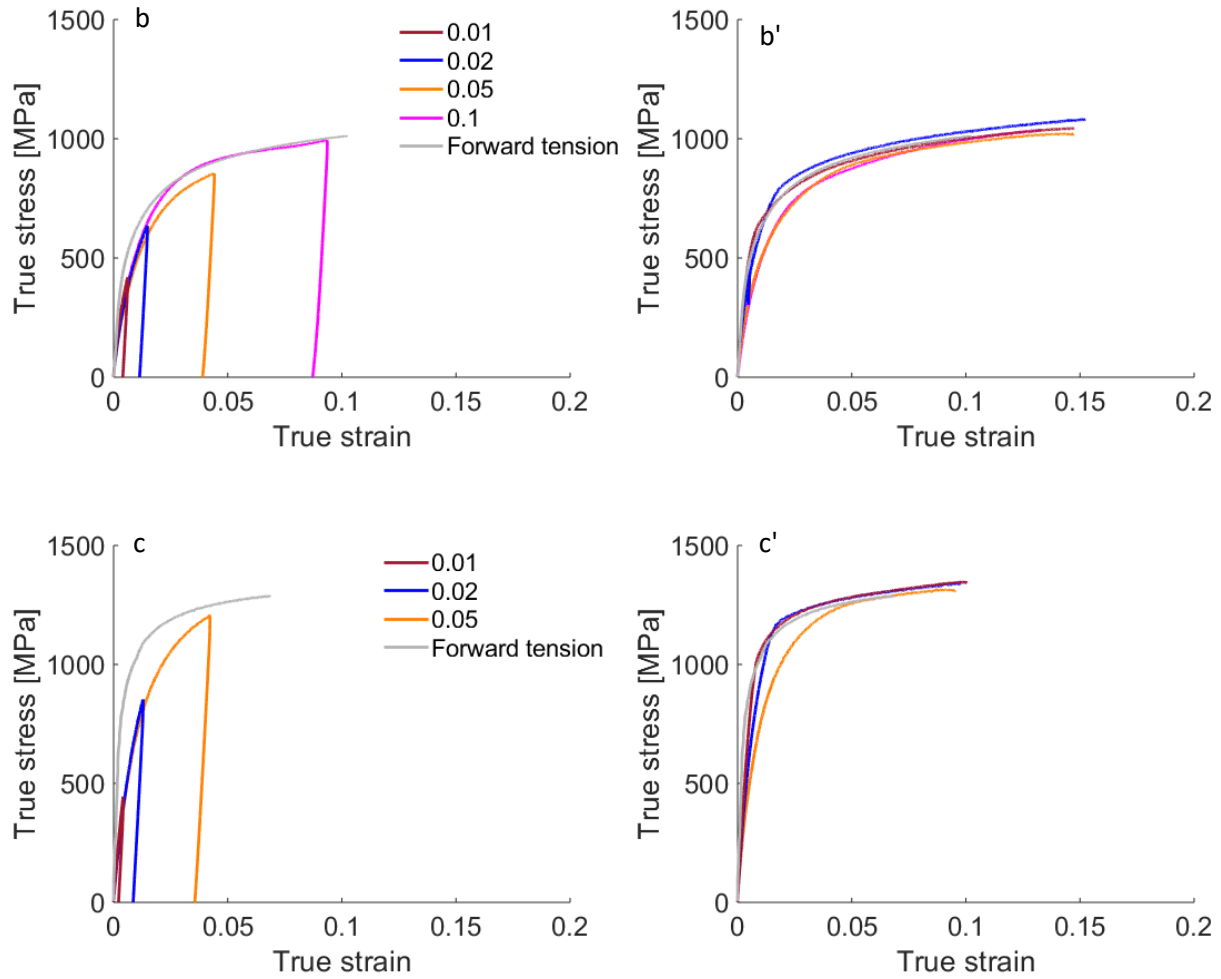
Figure 2. Comparison of the forward tension versus the 1st reversal (i.e. compression) curves pre-strained in tension to different strain levels for (a) DP 590, DP 780, and (c) DP 1180. Comparison of the forward tension versus the 2nd reversal (i.e. tension) curves pre-strained in tension followed by compression to different strain levels for (a') DP 590, (b') DP 780, and (c') DP 1180. Legends are shown in the 'unprimend' plots and are the same for the corresponding 'primed' plots.
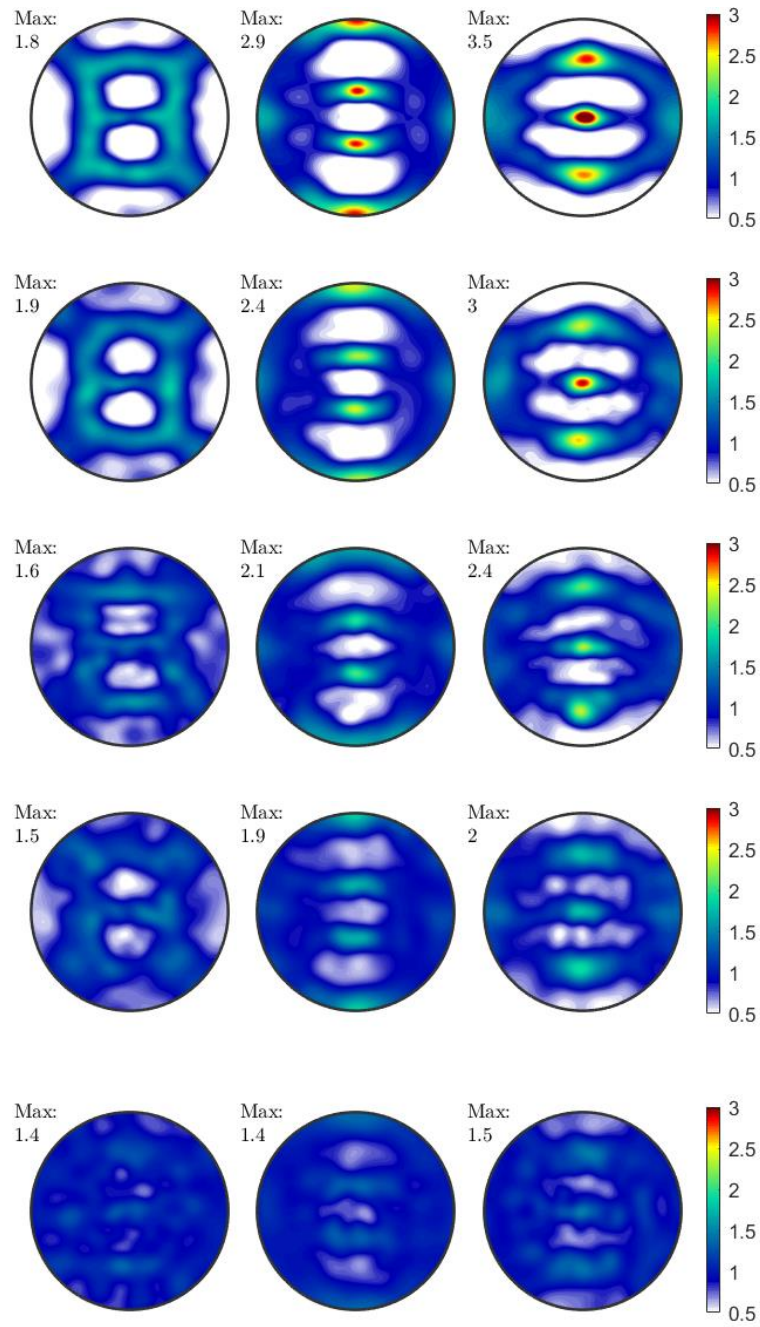
Figure 3. Stereographic pole figures showing the initial texture in sheets of DP 590 (top), DP 780, DP 980, and DP 1180, and MS 1700 (bottom).

4.3 Model calibration and validation

This section begins by calibrating the model using the cyclic tension-compression-tension response of DP 590, DP 780, and DP 1180 steels. The axial deformation processes are simulated by applying strain increments along the rolling direction (RD), while enforcing the normal stresses in transverse direction (TD) and normal direction (ND) as well as the shear strains to zero. In the simulations, the measured textures were compacted to 150 weighted orientations for ferrite, while 100 random orientations were used for texture of martensite. The texture compaction methodology was described in (Eghtesad et al., 2018b; Knezevic and Landry, 2015).
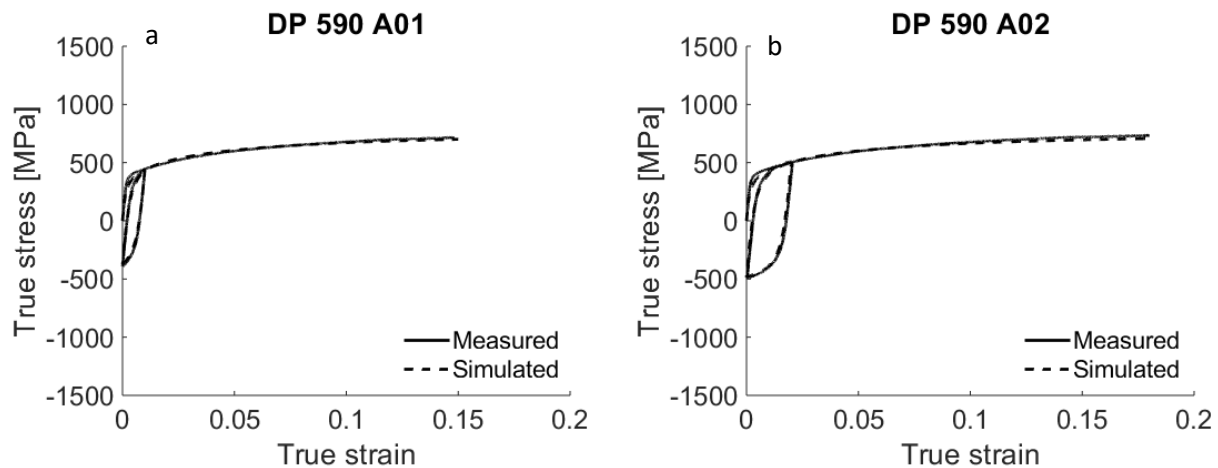
The parameters pertaining to the hardening law for the evolution of slip resistances in ferrite and martensite and the backstress law for ferrite were adjusted using one cyclic tension-compression-tension curve per steel, as each parameter affects a different portion of the curve. The curve deformed to a tensile pre-strain of 0.06 was used for DP 590, while the curves deformed to a tensile pre-strain of 0.05 were used for DP 780 and DP 1180. The identified parameters were slightly altered by comparing another cyclic curve per steel. The remaining tension-compression-tension curves can be regarded as predictions. The parameters identified per phase are the initial resistance to slip, τ_0^α, trapping rate coefficient, k_1^α, drag stress, D^α and activation barrier for de-pinning, g^α. The identification procedure begins by varying τ_0^α to reproduce initial yielding. Next, k_1^α, is varied such that the initial hardening slope is captured. Next, g^α and D^α are varied to match the hardening rates. Finally, q^α is fit to capture the later stage of the hardening rates. Simultaneously with the hardening parameters, the backstress law parameters for ferrite were calibrated for DP 590, DP 780, and DP 1180. These include the saturation value for backstress τ_{bs}^{sat}, asymmetry factor, A, and coefficients v and γ_b. Here, both τ_{bs}^{sat} and A are varied simultaneously to obtain the unloading and asymmetric yield at load reversals. Once these are achieved, tuning v and γ_b simply provides better fits. Next, the monotonic curves were simulated.

While these for DP 590, DP 780, and DP 1180 are predictions, some parameters were slightly adjusted to fit the data for DP 980 and MS 1700. The established parameters are given in Table 3. Note that the hardening parameters per phase are the same for every steel, except D^α and the initial content of dislocation density per phase.

The initial slip resistances, τ_0^α, were first estimated 75.4, 77.8, 80.8, 93.9, 95.9 [MPa] for ferrite and 501.8, 503.5, 550.4, 652.2, 774.2 [MPa] for martensite per steel, DP 590, DP 780, DP 980, DP 1180, and MS 1700, respectively. These values include the contribution of the initial dislocation density content. Given the measured values of dislocation density per phase for DP 1180 provided in (Yaddanapudi et al., 2021), we estimated the friction term of slip resistance, τ_{00}^α by subtracting the contribution of the initial dislocation density from τ_0^α for DP 1180. Keeping the same friction stress for every steel, we estimated the initial dislocation density per phase for every steel, $\sum_s \rho_{initial}^s$. Dislocation density increases with the content of martensite per steel. The expansion in volume during austenite to martensite phase transformation causes the deformation of ferrite phase and accumulation dislocations around martensite regions (Calcagnotto et al., 2010; Kadkhodapour et al., 2011). Therefore, the content of initial dislocation density is larger in steels containing more martensite. The higher the content, the higher the strength. It should also be noted that, in addition to the content of dislocations, chemical composition (i.e. the carbon content) influence the slip resistance and drag stress of the steels. This is true especially for martensite (Das et al., 2017). Therefore, the estimate for τ_{00}^α is an approximation.

Figure 4 shows the comparison between measured and simulated tension-compression-tension curves for the three steels. The multiple-range hysteresis curves are modeled with reasonable accuracy. In particular, the model is capable of reproducing the features specific to the load reversal behavior of the steels including the hardening rates during forward loading, non-linear

unloading, BE, permanent softening and subsequent hardening rates. Figure 5 shows the comparison for the monotonic data. The basic properties of the steels are listed in Table 4. The model is further experimentally validated by simulating a set of data recorded under variable strain ranges and mean strains for DP 780 and DP 1180. The model is able to capture these complex data sets also with reasonable accuracy as shown in Figure 6. Although the model captures the yield point in the first cycle, re-yielding in the subsequent cycles is often over-predicted. Model modifications such as including spreads of field variables over ellipsoids could improve these predictions. Such spreads have been incorporated in a visco-plastic SC formulation (Zecevic et al., 2017).

DP 590 A04

DP 590 A06

DP 590 A08
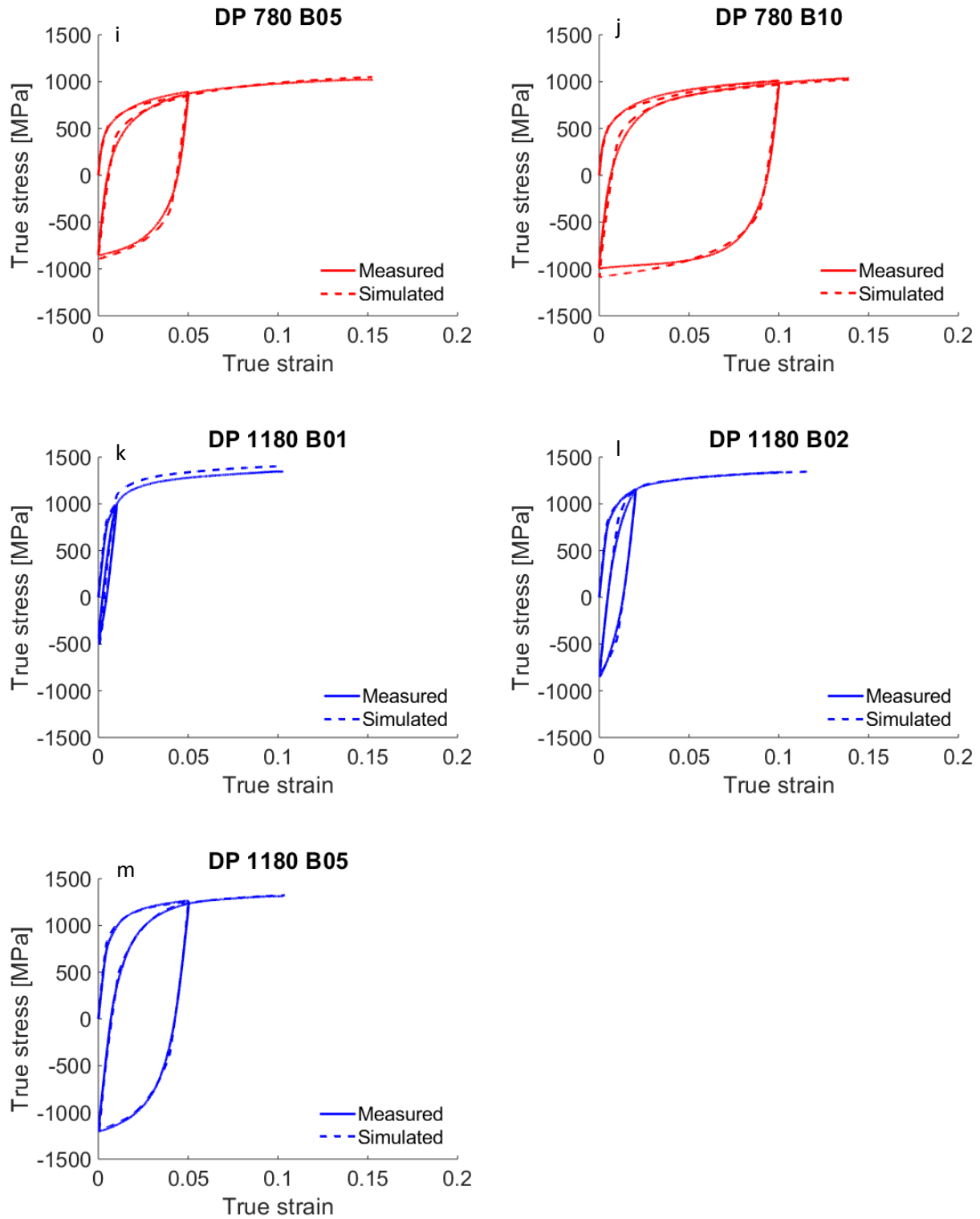
DP 590 A10

DP 780 B01

DP 780 B02
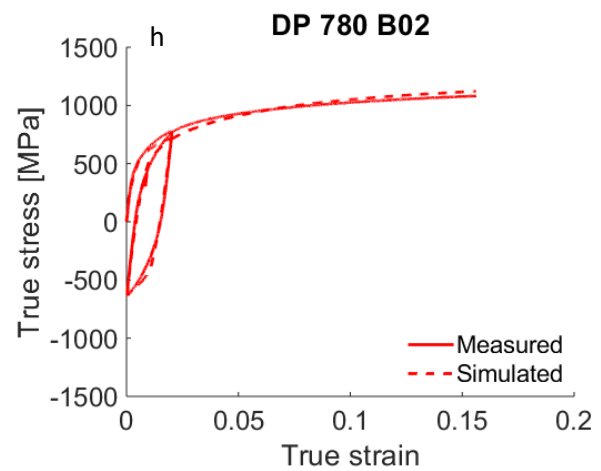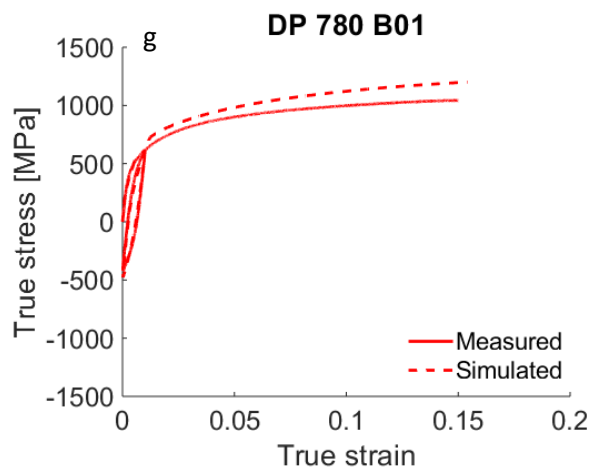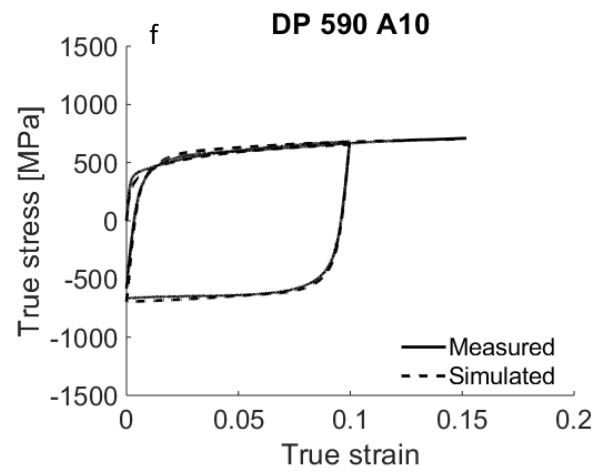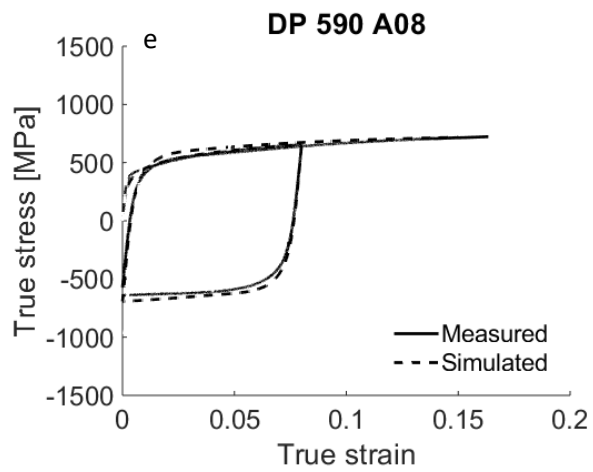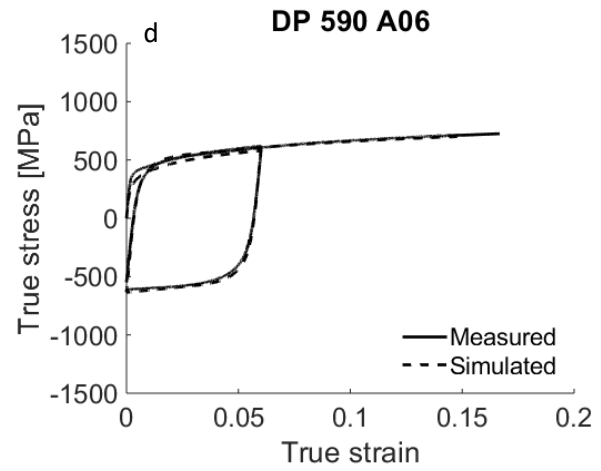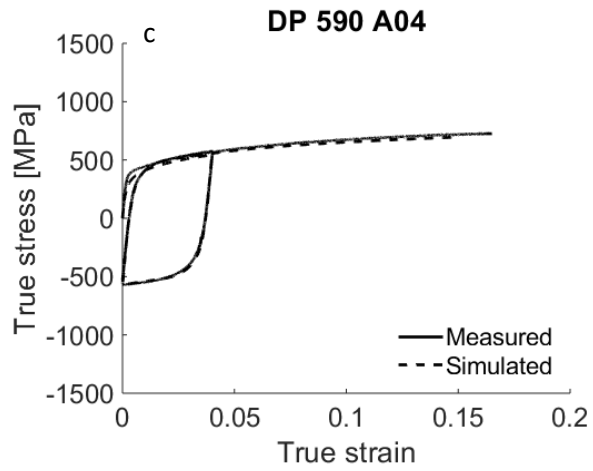
Figure 4. Comparison of measured and simulated true stress-true strain response during strain path load reversals for (a - f) DP 590, (g - j) DP 780, and (k - m) DP 1180.

Table 3a. Fitting parameters pertaining to the evolution of slip resistance for $\{110\}\langle 1\bar{1}1\rangle$ and $\{112\}\langle 11\bar{1}\rangle$ slip modes in ferrite (F) and martensite (M) common for all steels. The Burgers vector is 2.48e-10 m.

Parameter	F	M
$k_1^{\alpha}[m^{-1}]$	2.5e8	1.5e8
τ_{00}^{α} [MPa]	75	500
g^{α}	0.009	0.01
q^{α}	20	20

Table 3b. Fitting parameters pertaining to the evolution of slip resistance for $\{110\}\langle 1\bar{1}1\rangle$ and $\{112\}\langle 11\bar{1}\rangle$ slip modes in ferrite (F) and martensite (M) per steel.

Parameter	DP 590 (F)	DP 590 (M)	DP 780 (F)	DP 780 (M)	DP 980 (F)	DP 980 (M)	DP 1180 (F)	DP 1180 (M)	MS 1700 (F)	MS 1700 (M)
$\sum_s \rho_{initial}^s$	3.4e9	4.08e10	3.4e10	5.08e10	4.37e10	1.46e11	3.14e12	1.47e13	4e12	4.92e14
D^{α}	650	700	700	750	700	780	800	850	850	900

Table 3c. Fitting parameters pertaining to the evolution of backstress in ferrite per steel.

Parameters	DP 590 (F)	DP 780 (F)	DP 1180 (F)
$\tau_{bs}^{sat}[MPa]$	35	110	195

	ν	1000	1000	1000
	γ_b	0.001	0.003	0.005
	A	2	2	2
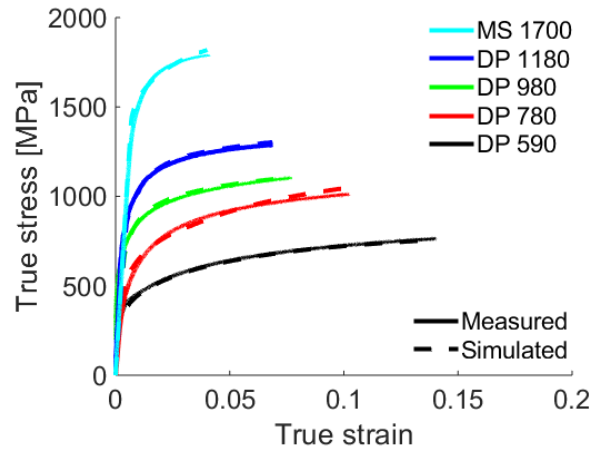
Figure 5. Comparison of measured and predicted true stress-true strain response in simple tension for the studied steels.

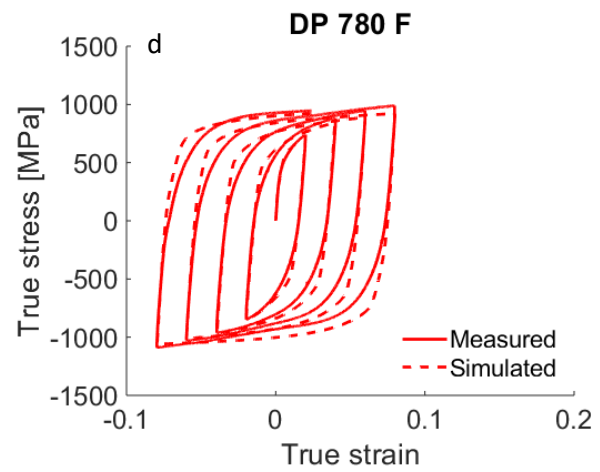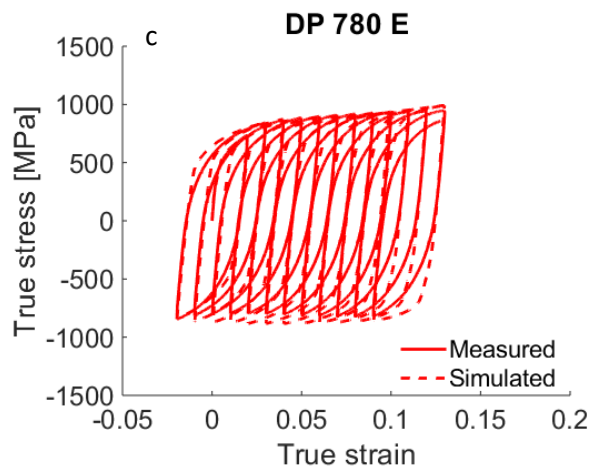Table 4. Properties based on the engineering curves for the steel sheets.

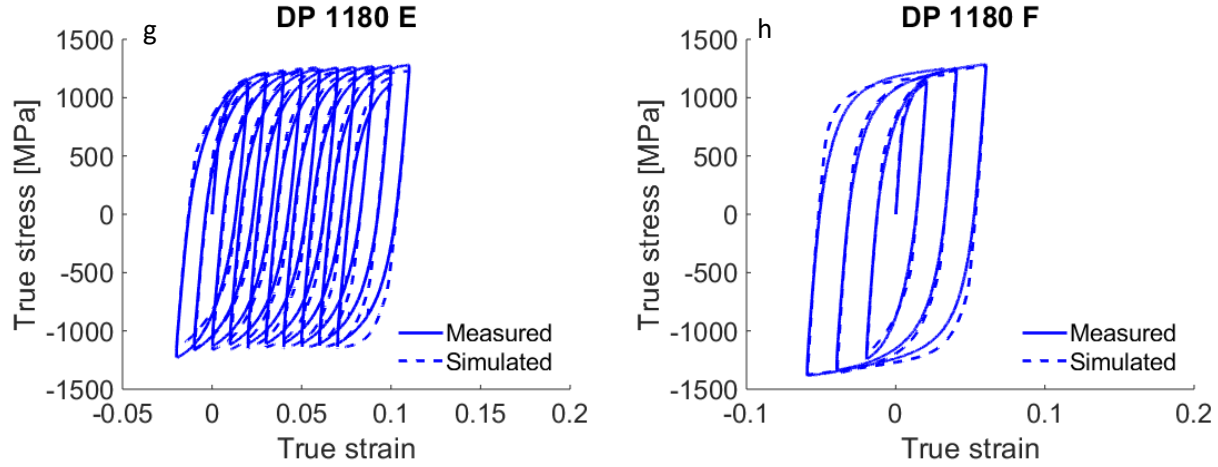|	DP 590 (RD)	DP 780 (RD)	DP 980 (RD)	DP 1180 (RD)	MS 1700 (RD)
0.2% offset yield stress (MPa)	407	504	630	840	1487
UTS (MPa)	663	913	1090	1288	1778
Eng. strain at UTS	0.146	0.108	0.086	0.072	0.041
Eng. strain at fracture	0.187	0.139	0.111	0.077	0.042
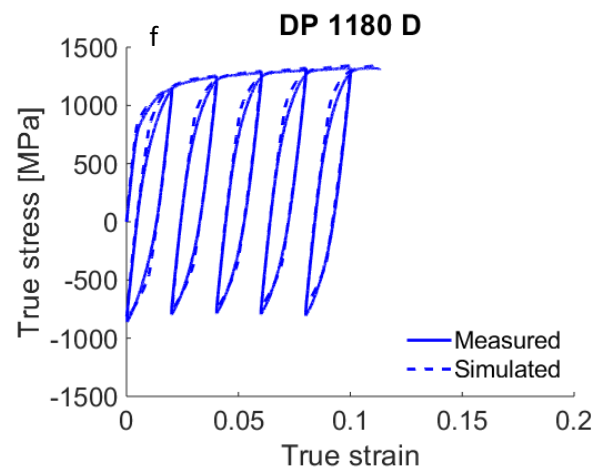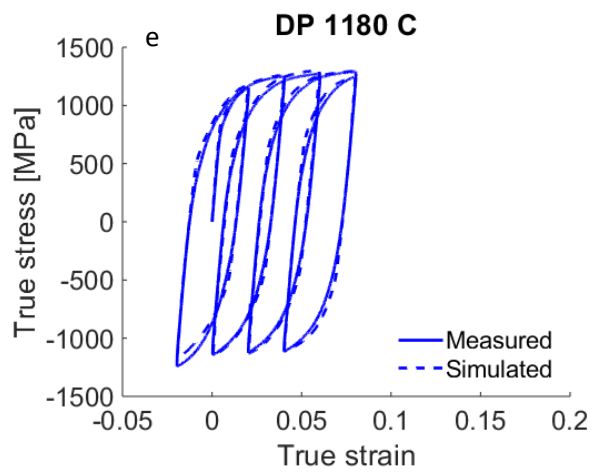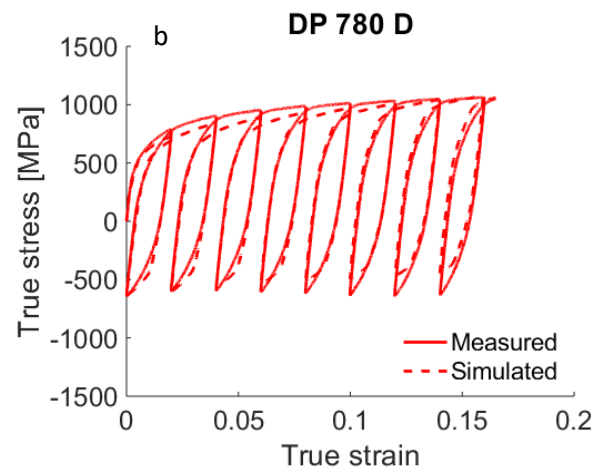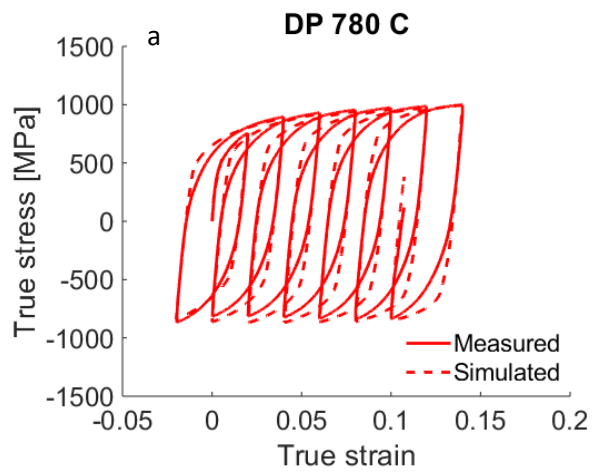
Figure 6. Comparison of measured and predicted true stress-true strain response during large strain reversals for (a - d) DP 780, and (e - h) DP 1180. The strain path in (a, e) is: $0 \rightarrow 0.02 \rightarrow -0.02 \rightarrow 0.04 \rightarrow 0 \rightarrow 0.06\ldots$ up to fracture with the strain amplitude of 0.04 and the mean strain increase of 0.02 per cycle. The strain path in (b, f) is: $0 \rightarrow 0.02 \rightarrow 0 \rightarrow 0.04 \rightarrow 0.02 \rightarrow 0.06\ldots$ up to fracture with the strain amplitude of 0.02 and the mean strain increase of 0.02 per cycle. The strain path in (c, g) is: $0 \rightarrow 0.02 \rightarrow -0.02 \rightarrow 0.03 \rightarrow -0.01 \rightarrow 0.04\ldots$ up to fracture with the strain amplitude of 0.04 and the mean strain increase of 0.01 per cycle. The strain path in (d, h) is: $0 \rightarrow 0.02 \rightarrow -0.02 \rightarrow 0.04 \rightarrow -0.04 \rightarrow 0.06\ldots$ up to fracture.

5. Discussion

This work presents comprehensive monotonic and load reversal data for five dual phase (DP) steels and is concerned with interpreting the data using a crystal plasticity model, which considers microstructural evolution and the directionality of single-crystal level deformation mechanisms. The model is the EPSC formulation (Zecevic et al., 2016), which incorporates a dislocation

density-based hardening law (Beyerlein and Tomé, 2008) advanced to account for dissolution of dislocations upon load reversal and a slip system-level backstress law.

The load reversal data recorded for DP steels showed the typical decreasing hardening rate during forward tension, a linear and then a non-linear unloading, followed by the BE, and a slight shift in the hardening rate during continuous straining. The data were used to calibrate and critically validate the EPSC model. The good performance of the model in capturing such elasto-plastic deformation characteristics is a consequence of accounting for kinematic hardening at the slip system-level through the evolution law for backstress for both ferrite and martensite and dislocation annihilation physical mechanism to reflect the experimentally observed decrease in dislocation density upon strain reversal. Additionally, the model is correctly initialized with the experimentally measured texture, phase fractions, and dislocation density per phase. From the comparisons between data and predictions, the aim is to provide insights into various aspects of the material response during load reversals.

It is observed that the tensile hysteresis loops do not overlap with the monotonic tensile curves. Several additional parameters can be defined from the differences to further discuss the load reversal deformation characteristics of the steels. Figure 7a illustrates these parameters using representative enlarged areas of the stress-strain curves. The parameters are the reloading stress differential, $\Delta\sigma_h$, reloading softening stress, $\Delta\sigma_s$, and ratcheting strain, ϵ_Δ. These specific parameters are quantified for DP 780 and DP 1180. Additionally, the unloading deviation stress $\Delta\sigma$ is quantified for DP 590, DP 780, and DP 1180. The values of these individual parameters are discussed as a function of martensite and loading.

The reloading yield stress differential under tension (the differential between initial tension and 2nd reversal), $\Delta\sigma_h$, as a function of the applied tensile pre-strain is shown in Figure 7b. The

differential increases with plastic strain and content of dislocations. While positive for DP 590, it is negative for DP 780 and DP 1180. Evidently, the increasing content of martensite weakens the reloading yield effect, which is attributed to the increase in backstress in the microstructure with martensite. The evolution of reloading softening stress with the tensile pre-strain for the investigated steels is shown in Figure 7c based on the data for two strain amplitudes, 0.02 and 0.04. Since the results are similar for both strain amplitudes, likely no appreciable plasticity occurred in compression for both datasets. The softening effects is slightly larger for the softer steel. Figure 7d shows the ratcheting strain evolution with the tensile pre-strain. Overall, the ratcheting strain shows a similar evolution trend as the reloading softening effect because the ratcheting strain results from the softening effect but, in contrast, increases with the strain amplitude and underlying loading nonlinearity. The less strong/stiff DP 780 has the ratcheting strain a bit greater than the more strong/stiff DP 1180. The unloading deviation stress, $\Delta\sigma$, is shown in Figure 7e as a function of the applied pre-strain in tension. The deviation increases with the strength of the steels.

The model reveals that the backstress predominately controls the non-linear unloading deformation and the BE along with the reloading yield effect, while the evolution of dislocation density plays a role in capturing the BE and, more importantly, in predicting the hardening rates. Figure 8 shows the evolution of backstress with the accumulated shear strain in a randomly selected grain per phase for a slip system with the highest activity in the selected grain. It should be noted that stress in each grain is a consequence of the applied stress, intergranular interaction stress, and backstress. The backstress in ferrite hinders the process of plastic deformation, since it acts against the applied field. In contrast, the backstress in the martensite phase is opposite to the backstress present in the ferrite acting with the applied field because the volume average backstress

in the material vanishes. Note the line type in Figure 8. The backstress in ferrite will aids the activation upon the reversal. The tradeoff between the magnitude of backstress per phase (Figure 8) over the steels is a consequence of the volume fraction of ferrite versus martensite per steel (Table 2). Specifically, the increasing content of martensite weakens the reloading yield effect because it increases the backstress in the microstructure (Figure 8). Note that the magnitude of backstress in martensite is driven by the magnitude of backstress in ferrite but scales inversely with the volume fraction of martensite. The tradeoff governs the unloading and subsequent yield differential per steel. The fact that martensite is deforming elastically longer than ferrite is also contributing to the tradeoff, especially after the reversal.

The annihilation of dislocation density is another important mechanism for accurate predictions of stress levels during cyclic deformation. Figure 9 shows the dislocation density evolution during the cyclic deformation of DP 1180. Such plots for other steels look similar and are not provided. The plot shows that the dislocation density evolves much more rapidly in ferrite than in martensite. The dissolution of the dislocations upon load reversal is essential in predicting the changes in the hardening rates. Evidently some deformation can be accommodated without a large increase in dislocation density. These results agree with the constitutive assumptions invoked in developing cyclic plasticity models (Ohno, 1982; Ohno and Kachi, 1986).

a

b
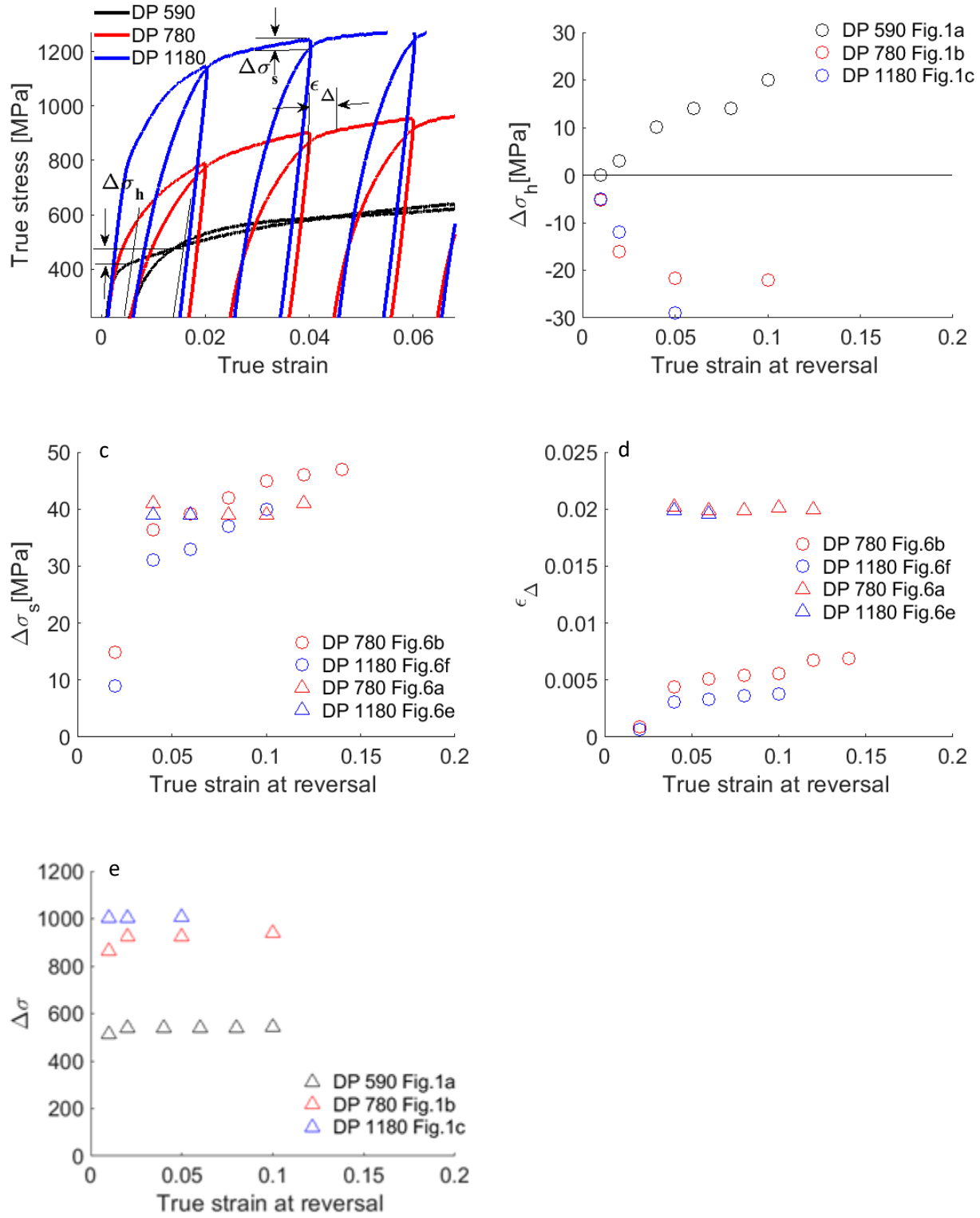
Figure 7. (a) An illustration to define the reloading yield stress differential under tension ($\Delta\sigma_h$), reloading softening stress ($\Delta\sigma_s$), and ratcheting strain (ϵ_Δ) parameters. (b) Comparison of $\Delta\sigma_h$

versus true strain levels for 1st reversal. (c) Comparison of $\Delta\sigma_s$ versus true strain levels for tension.

(d) Comparison of ϵ_Δ versus true strain levels for tension. (e) Unloading deviation stress ($\Delta\sigma = \sigma_L$

$- \sigma_U$), where σ_L is the true stress at the end of a pre-load and σ_U is the macro-yield during unload

at approximately 0.001 offset.
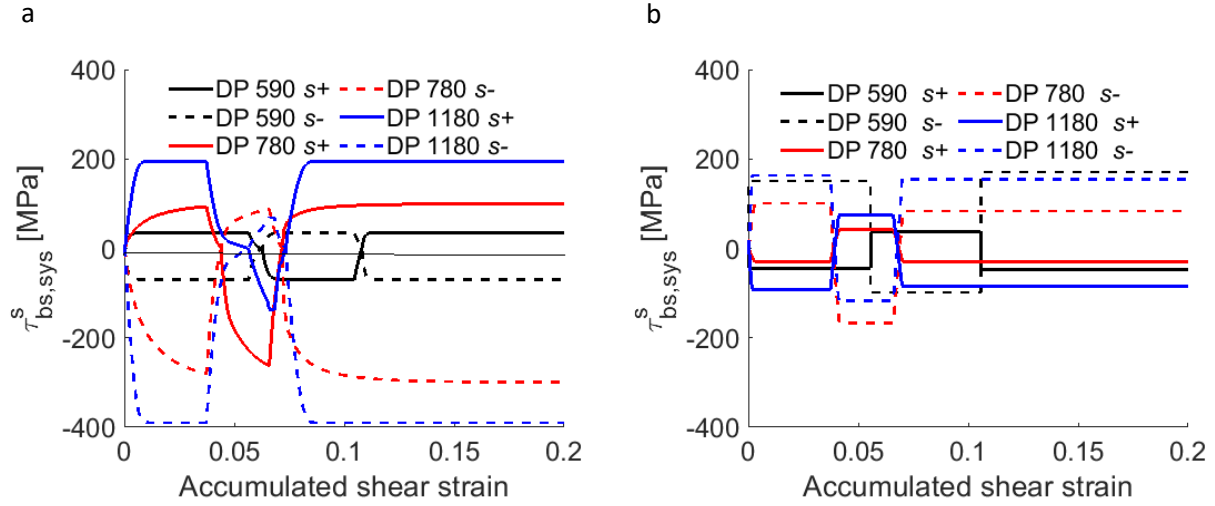
Figure 8. Evolution of backstress with accumulated shear strain in a randomly selected (a) ferrite

grain and (b) a randomly selected martensite grain for an sth slip system with the highest activity

per grain during forward tension followed by the 1st and the 2nd reversal for DP 590 (Fig. 4d), DP

780 (Fig. 4i), and DP 1180 (Fig. 4m). The same crystal orientation and the same slip system per

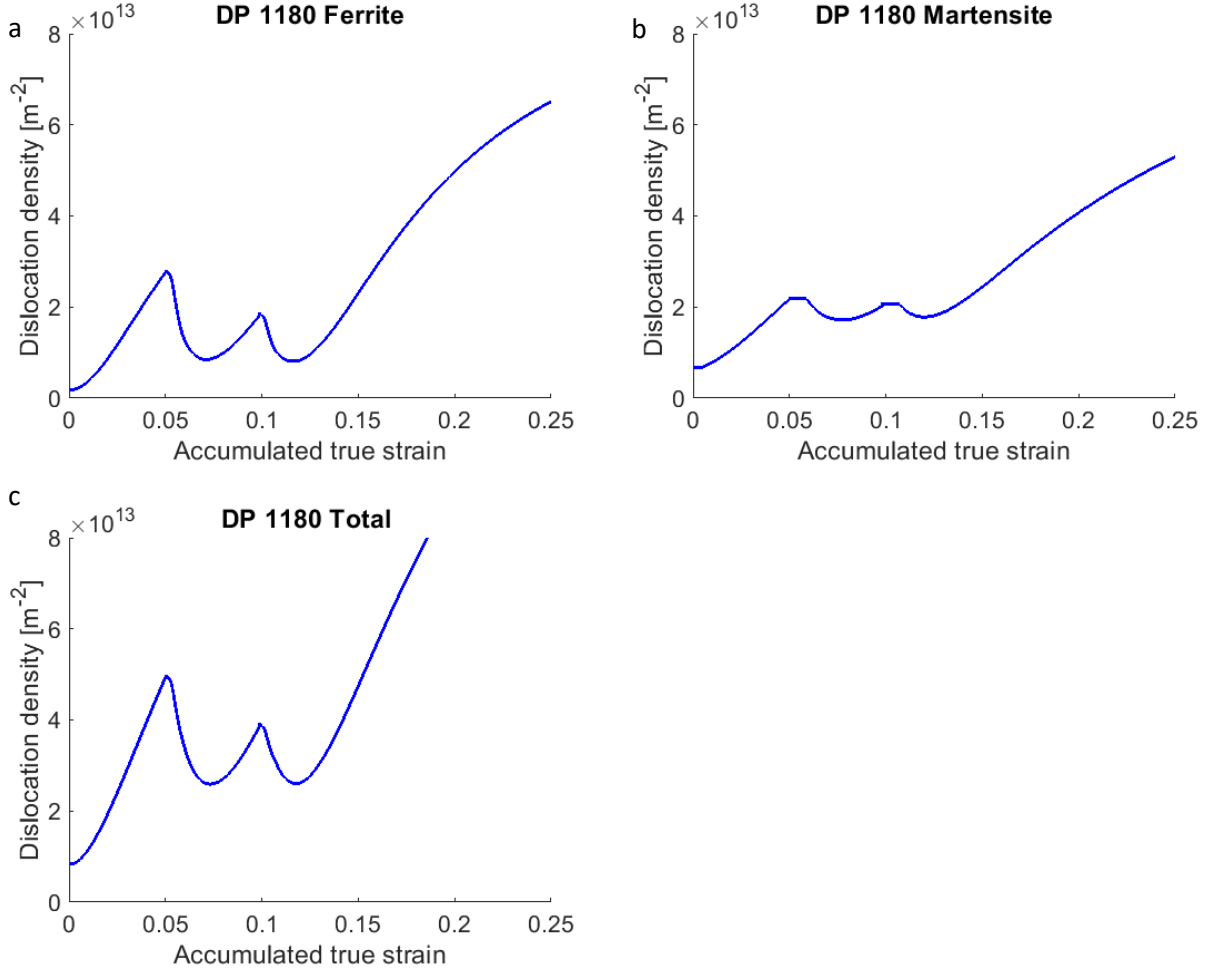phase are selected for every material.

Figure 9. Evolution of total dislocation density ($\Sigma_s \rho_{tot}^s$) in (a) ferrite, (b) martensite, and (c) combined ferrite + martensite during load reversal deformation of DP 1180 (Fig. 4m).

6. Conclusions

The monotonic response of DP 590, DP 780, DP 980, DP 1180, and MS 1700 and the large strain cyclic response of DP 590, DP 780, and DP 1180 steel sheets was measured. The large body of cyclic data showed consistently the typical decreasing hardening rate during forward tension, a linear and then a non-linear unloading, followed by the BE, and some shift in the hardening rate during continuous straining. Since the cyclic loops did not overlap with the monotonic curves,

41

parameters such as the reloading yield stress differential, reloading softening stress, ratcheting strain, and unloading deviation stress were identified and quantified. The pre-strain level in forward loading increased the magnitude of macro-yield stress, while the unloading deviation stress was approximately constant. The extent of the non-linear unloading increased with strength of the steels. Since the elasto-plastic transition upon the reversals (1st and the 2nd) was prolonged, the strain hardening rates reduced compared to those during the forward tension. Although reduced, the strain hardening in compression of DP 590 surpassed that in tension and also induced positive yield differentials under tension. The positive yield differential increased with pre-strain. In contrast, the yield differentials for DP 780 and DP 1180 were negative. The reloading softening stress and ratcheting strain scaled inversely with the strength of the steels. Upon yielding after the load reversal, the rates of strain hardening were quickly restored. Like non-linear unloading, the permanent softening was enhanced with strength.

The data were used to calibrate and critically validate an EPSC model developed for two-phase steels. The model features sub-models including a dislocation density-based hardening law and a slip system-level kinematic back-stress law for load reversals. It was shown that the model successfully reproduces the flow response of the steels during monotonic and cyclic deformation to various levels of plastic pre-strains. Specifically, hardening rates, non-linear unloading, and the BE were captured. Significantly, the model achieved excellent agreement for all data using a single set of parameters per phase except for one parameter, which varied from steel to steel. Such good performances of the model in capturing the deformation characteristics were a consequence of accounting for kinematic hardening at the slip system-level through the evolution law for backstress for both ferrite and martensite and dislocation annihilation physical mechanism to reflect the experimentally observed decrease in dislocation density upon strain reversals.

Additionally, the model was correctly initialized with the experimentally measured texture, phase fractions, and dislocation density per phase. The combination of comprehensive experimental data and modeling results allowed us to infer that the tradeoff between the magnitude of backstress per phase and the volume fraction of ferrite versus martensite per steel determined the unloading and subsequent yield differential per steel, while the dissolution of dislocations facilitated capturing the hardening rates during load reversal deformation. Specifically, the increasing content of martensite weakened the reloading yield effect because it increased the overall backstress in the microstructure. As the phenomena captured by the standalone model have major implications on the accuracy of simulations of metal forming processes of steels, the model will be used in the FEM forming simulations treating complex, non-monotonic deformation conditions in the future works.

Acknowledgments

References

Abel, A., 1987. Historical perspectives and some of the main features of the Bauschinger effect, Materials Forum. Institute of Metals and Materials Australasia, pp. 11-26.

Armstrong, P.J., Frederick, C.O., 1966. A mathematical representation of multiaxial Bauschinger effect. Berkeley nuclear laboratories.

Bachmann, F., Hielscher, R., Schaeben, H., 2010. Texture analysis with MTEX–free and open source software toolbox. Solid State Phenomena 160, 63-68.

Bate, P.S., Wilson, D.V., 1986. Analysis of the bauschinger effect. Acta Metallurgica 34, 1097-1105.

Bauschinger, J., 1886. Über die Veränderung der Elasticitätsgrenze und Festigkeit des Eisen und Stahls durch Strecken und Quetschen, durch Erwarmen und Abkühlen und durch oftmal wiederholte Beanspruchung. Mitteilungen aus dem mechanisch-technischen Laboratorium der k. polytechnischen Schule, 1877-1836.

Bayley, C.J., Brekelmans, W.A.M., Geers, M.G.D., 2006. A comparison of dislocation induced back stress formulations in strain gradient crystal plasticity. International Journal of Solids and Structures 43, 7268-7286.

Beyerlein, I.J., 2008. Plastic Behavior of Metals in Reverse Straining after Large Pre-Strains. Materials Science Forum 579, 41-60.

Beyerlein, I.J., Tomé, C.N., 2007. Modeling transients in the mechanical response of copper due to strain path changes. Int. J. Plast. 23, 640-664.

Beyerlein, I.J., Tomé, C.N., 2008. A dislocation-based constitutive law for pure Zr including temperature effects. Int. J. Plast. 24, 867-895.

Bhadeshia, H.K.D.H., 2002. TRIP-assisted steels? ISIJ international 42, 1059-1060.

Bhargava, M., Chakrabarty, S., Barnwal, V.K., Tewari, A., Mishra, S.K., 2018. Effect of microstructure evolution during plastic deformation on the formability of Transformation Induced Plasticity and Quenched & Partitioned AHSS. Mater. Des. 152, 65-77.

Bhattacharyya, A., Knezevic, M., Abouaf, M., 2015. Characterization of Crystallographic Texture and Intra-Grain Morphology in Cross-Rolled Tantalum. Metall. Mater. Trans. A 46, 1085-1096.

Brown, L.M., Stobbs, W.M., 1971. The Work-Hardening of Copper-Silica: I. A Model Based on Internal Stresses, With No Plastic Relaxation. Philosophical Magazine 23, 1185–1199.

Calcagnotto, M., Adachi, Y., Ponge, D., Raabe, D., 2011. Deformation and fracture mechanisms in fine- and ultrafine-grained ferrite/martensite dual-phase steels and the effect of aging. Acta. Mater. 59, 658-670.

Calcagnotto, M., Ponge, D., Demir, E., Raabe, D., 2010. Orientation gradients and geometrically necessary dislocations in ultrafine grained dual-phase steels studied by 2D and 3D EBSD. Materials Science and Engineering: A 527, 2738-2746.

Calcagnotto, M., Ponge, D., Raabe, D., 2012. Microstructure control during fabrication of ultrafine grained dual-phase steel: characterization and effect of intercritical annealing parameters. ISIJ international 52, 874-883.

Cantara, A.M., Zecevic, M., Eghtesad, A., Poulin, C.M., Knezevic, M., 2019. Predicting elastic anisotropy of dual-phase steels based on crystal mechanics and microstructure. International Journal of Mechanical Sciences 151, 639-649.

Chaboche, J., Rousselier, G., 1983. On the plastic and viscoplastic constitutive equations—Part I: Rules developed with internal variable concept. Journal of Pressure Vessel Technology 105, 153-158.

Chaboche, J.L., 1977. Viscoplastic constitutive equations for the description of cyclic and ansiotropic behavior of metals, In: XVIIth Polish solid mechanics conference, Bulletin de l'Académie Polonaise des Sciences, Série Sciences et Techniques, pp. 33-41.

Chaboche, J.L., 2008. A review of some plasticity and viscoplasticity constitutive theories. Int. J. Plast. 24, 1642-1693.

Choi, S.H., Kim, E.Y., Woo, W., Han, S.H., Kwak, J.H., 2013. The effect of crystallographic orientation on the micromechanical deformation and failure behaviors of DP980 steel during uniaxial tension. International Journal of Plasticity 45, 85-102.

Cullen, G.W., Korkolis, Y.P., 2013. Ductility of 304 stainless steel under pulsed uniaxial loading. International Journal of Solids and Structures 50, 1621-1633.

Das, A., Ghosh, M., Tarafder, S., Sivaprasad, S., Chakrabarti, D., 2017. Micromechanisms of deformation in dual phase steels at high strain rates. Mater. Sci. Eng. A 680, 249-258.

Demir, E., Raabe, D., 2010. Mechanical and microstructural single-crystal Bauschinger effects: Observation of reversible plasticity in copper during bending. Acta. Mater. 58, 6055-6063.

Deng, N., Kuwabara, T., Korkolis, Y.P., 2015. On the non-linear unloading behavior of a biaxially loaded dual-phase steel. (in preparation).

Dotsenko, V.I., 1979. Stress Relaxation in Crystals. physica status solidi (b) 93, 11-43.

Eghtesad, A., Barrett, T.J., Germaschewski, K., Lebensohn, R.A., McCabe, R.J., Knezevic, M., 2018a. OpenMP and MPI implementations of an elasto-viscoplastic fast Fourier transform-based micromechanical solver for fast crystal plasticity modeling. Advances in Engineering Software 126, 46-60.

Eghtesad, A., Barrett, T.J., Knezevic, M., 2018b. Compact reconstruction of orientation distributions using generalized spherical harmonics to advance large-scale crystal plasticity modeling: Verification using cubic, hexagonal, and orthorhombic polycrystals. Acta. Mater. 155, 418-432.

Eshelby, J.D., 1957. The determination of the elastic field of an ellipsoidal inclusion, and related problems. Proc R. Soc. Lond. A 241, 376-396.

Evers, L.P., Brekelmans, W.A.M., Geers, M.G.D., 2004. Non-local crystal plasticity model with intrinsic SSD and GND effects. Journal of the Mechanics and Physics of Solids 52, 2379-2401.

Feather, W.G., Savage, D.J., Knezevic, M., 2021. A crystal plasticity finite element model embedding strain-rate sensitivities inherent to deformation mechanisms: Application to alloy AZ31. Int. J. Plast. 143, 103031.

Feng, Z., Yoon, S.-Y., Choi, J.-H., Barrett, T.J., Zecevic, M., Barlat, F., Knezevic, M., 2020. A comparative study between elasto-plastic self-consistent crystal plasticity and anisotropic yield function with distortional hardening formulations for sheet metal forming. Mechanics of Materials 148, 103422.

Fleck, N.A., Muller, G.M., Ashby, M.F., Hutchinson, J.W., 1994. Strain gradient plasticity: Theory and experiment. Acta Metallurgica et Materialia 42, 475-487.

Fromm, B.S., Adams, B.L., Ahmadi, S., Knezevic, M., 2009. Grain size and orientation distributions: Application to yielding of a-titanium. Acta. Mater. 57, 2339-2348.

Gardey, B., Bouvier, S., Bacroix, B., 2005. Correlation between the macroscopic behavior and the microstructural evolutions during large plastic deformation of a dual-phase steel. Metallurgical and Materials Transactions A 36, 2937-2945.

Ghaei, A., Green, D.E., Aryanpour, A., 2015. Springback simulation of advanced high strength steels considering nonlinear elastic unloading–reloading behavior. Mater. Des. 88, 461-470.

Goh, C.-H., Neu, R.W., McDowell, D.L., 2003. Crystallographic plasticity in fretting of Ti–6AL–4V. International Journal of Plasticity 19, 1627-1650.

Gong, H., Wang, S., Knysh, P., Korkolis, Y.P., 2016. Experimental investigation of the mechanical response of laser-welded dissimilar blanks from advanced- and ultra-high-strength steels. Mater. Des. 90, 1115-1123.

Gough, H., Hanson, D., Wright, S., 1927. The Behaviour of Single Crystals of Aluminium under Static and Repeated Stresses. Philosophical Transactions of the Royal Society of London. Series A, Containing Papers of a Mathematical or Physical Character, 1-30.

Gracio, J.J., Barlat, F., Rauch, E.F., Jones, P.T., Neto, V.F., Lopes, A.B., 2004. Artificial aging and shear deformation behaviour of 6022 aluminium alloy. Int. J. Plast. 20, 427-445.

Harder, J., 1999. A crystallographic model for the study of local deformation processes in polycrystals. Int. J. Plast. 15, 605-624.

Hasegawa, T., Yakou, T., Karashima, S., 1975. Deformation behaviour and dislocation structures upon stress reversal in polycrystalline aluminium. Materials Science and Engineering 20, 267-276.

Holscher, M., Raabe, D., Lucke, K., 1994. Relationship between rolling textures and shear textures in F.C.C. and B.C.C. metals. Acta Metall. Mater. 42, 879-886.

Hosford, W.F., Caddell, R.M., 1993. Metal forming mechanics and metallurgy. Prentice-Hall, Inc.

Hu, Z., Rauch, E.F., Teodosiu, C., 1992. Work-hardening behavior of mild steel under stress reversal at large strains. Int. J. Plast. 8, 839-856.

Kadkhodapour, J., Schmauder, S., Raabe, D., Ziaei-Rad, S., Weber, U., Calcagnotto, M., 2011. Experimental and numerical study on geometrically necessary dislocations and non-homogeneous mechanical properties of the ferrite phase in dual phase steels. Acta Materialia 59, 4387-4394.

Kalidindi, S.R., Bronkhorst, C.A., Anand, L., 1992. Crystallographic texture evolution in bulk deformation processing of FCC metals. J. Mech. Phys. Solids 40, 537-569.

Kapp, M., Hebesberger, T., Kolednik, O., 2011. A micro-level strain analysis of a high-strength dual-phase steel. International Journal of Materials Research 102, 687-691.

Kassner, M.E., Geantil, P., Levine, L.E., 2013. Long range internal stresses in single-phase crystalline materials. International Journal of Plasticity 45, 44-60.

Kitayama, K., Tomé, C.N., Rauch, E.F., Gracio, J.J., Barlat, F., 2013. A crystallographic dislocation model for describing hardening of polycrystals during strain path changes. Application to low carbon steels. International Journal of Plasticity in press.

Knezevic, M., Drach, B., Ardeljan, M., Beyerlein, I.J., 2014. Three dimensional predictions of grain scale plasticity and grain boundaries using crystal plasticity finite element models. Computer Methods in Applied Mechanics and Engineering 277, 239-259.

Knezevic, M., Landry, N.W., 2015. Procedures for reducing large datasets of crystal orientations using generalized spherical harmonics. Mechanics of Materials 88, 73-86.

Knezevic, M., McCabe, R.J., Lebensohn, R.A., Tomé, C.N., Liu, C., Lovato, M.L., Mihaila, B., 2013. Integration of self-consistent polycrystal plasticity with dislocation density based hardening laws within an implicit finite element framework: Application to low-symmetry metals. J. Mech. Phys. Solids 61, 2034-2046.

Kocks, U.F., Mecking, H., 1981. Kinetics of Flow and Strain-Hardening. Acta Metall. 29, 1865-1875.

Kocks, U.F., Tomé, C.N., Wenk, H.-R., 1998. Texture and Anisotropy. Cambridge University Press, Cambridge, UK.

Kruml, T., Coddet, O., Martin, J., 2008. About the determination of the thermal and athermal stress components from stress-relaxation experiments. Acta. Mater. 56, 333-340.

Kudzal, A.D., McWilliams, B.A., Taggart-Scarff, J., Knezevic, M., 2020. Fabrication of a low alloy ultra-high strength (>1500 MPa yield) steel using powder bed fusion additive manufacturing. Mater. Sci. Eng. A 770, 138512.

Kuwabara, T., Kumano, Y., Ziegelheim, J., Kurosaki, I., 2009. Tension–compression asymmetry of phosphor bronze for electronic parts and its effect on bending behavior. Int. J. Plast. 25, 1759-1776.

Kuwabara, T., Nagata, K., Nakako, T., 2001. Measurement and analysis of the Bauschinger effect of sheet metals subjected to in plane stress reversals. Proceedings of AMPT 1, 407-412.

Lebensohn, R.A., Kanjarla, A.K., Eisenlohr, P., 2012. An elasto-viscoplastic formulation based on fast Fourier transforms for the prediction of micromechanical fields in polycrystalline materials. Int. J. Plast. 32-33, 59-69.

Lebensohn, R.A., Tomé, C.N., 1993. A self-consistent anisotropic approach for the simulation of plastic deformation and texture development of polycrystals: Application to zirconium alloys. Acta Metall. Mater. 41, 2611-2624.

Li, K., Carden, W., Wagoner, R., 2002. Simulation of springback. International Journal of Mechanical Sciences 44, 103-122.

Li, L., Shen, L., Proust, G., 2014. A texture-based representative volume element crystal plasticity model for predicting Bauschinger effect during cyclic loading. Materials Science and Engineering: A 608, 174-183.

Ma, A., Roters, F., Raabe, D., 2006a. A dislocation density based constitutive model for crystal plasticity FEM including geometrically necessary dislocations. Acta. Mater. 54, 2169-2179.

Ma, A., Roters, F., Raabe, D., 2006b. On the consideration of interactions between dislocations and grain boundaries in crystal plasticity finite element modeling – Theory, experiments, and simulations. Acta. Mater. 54, 2181-2194.

Ma, A., Roters, F., Raabe, D., 2007. A dislocation density based constitutive law for BCC materials in crystal plasticity FEM. Comput. Mater. Sci. 39, 91-95.

Ma, B., Liu, Z.G., Jiang, Z., Wu, X., Diao, K., Wan, M., 2016. Prediction of forming limit in DP590 steel sheet forming: An extended fracture criterion. Mater. Des. 96, 401-408.

Madec, R., Devincre, B., Kubin, L., Hoc, T., Rodney, D., 2003. The role of collinear interaction in dislocation-induced hardening. Science 301, 1879-1882.

McDowell, D.L., 1992. A nonlinear kinematic hardening theory for cyclic thermoplasticity and thermoviscoplasticity. Int. J. Plast. 8, 695-728.

Mohebbi, M.S., Akbarzadeh, A., Yoon, Y.-O., Kim, S.-K., 2015. Stress relaxation and flow behavior of ultrafine grained AA 1050. Mechanics of Materials 89, 23-34.

Mompiou, F., Caillard, D., Legros, M., Mughrabi, H., 2012. In situ TEM observations of reverse dislocation motion upon unloading in tensile-deformed UFG aluminium. Acta. Mater. 60, 3402-3414.

Mughrabi, H., 1983. Dislocation wall and cell structures and long-range internal stresses in deformed metal crystals. Acta Metall. 31, 1367-1379.

Mughrabi, H., 2001. On the role of strain gradients and long-range internal stresses in the composite model of crystal plasticity. Materials Science and Engineering: A 317, 171-180.

Nesterova, E.V., Bouvier, S., Bacroix, B., 2015. Microstructure evolution and mechanical behavior of a high strength dual-phase steel under monotonic loading. Materials Characterization 100, 152-162.

Nieh, T.G., Nix, W.D., 1986. Unloading yield effects in aluminum alloys. Metallurgical transactions. A, Physical metallurgy and materials science 17 A, 121-126.

Nikhare, C., Hodgson, P., Weiss, M., 2011. Necking and fracture of advanced high strength steels. Mater. Sci. Eng. A 528, 3010-3013.

Ohno, N., 1982. A Constitutive Model of Cyclic Plasticity With a Nonhardening Strain Region. J. Appl. Mech. 49(4), 721-727

Ohno, N., Kachi, Y., 1986. A Constitutive Model of Cyclic Plasticity for Nonlinear Hardening Materials. J. Appl. Mech. 53(2), 395-403.

Orowan, E., 1959. Causes and Effects of Internal Stresses, General Motors Symposium, ed. G.M. Rassweiler and W.L. Grube. Elsevier, Amsterdam, pp. 59-80.

Pavlina, E., Lee, M.-G., Barlat, F., 2015. Observations on the Nonlinear Unloading Behavior of Advanced High Strength Steels. Metall. Mater. Trans. A 46, 18-22.

Poulin, C.M., Vogel, S.C., Korkolis, Y.P., Kinsey, B.L., Knezevic, M., 2020. Experimental studies into the role of cyclic bending during stretching of dual-phase steel sheets. International Journal of Material Forming 13, 393-408.

Prasad, K., Krishnaswamy, H., Arunachalam, N., 2020. Investigations on ductility improvement and reloading yielding during stress relaxation of dual phase Ti–6Al–4V titanium alloy. J. Alloys Compd. 828, 154450.

Roters, F., Eisenlohr, P., Hantcherli, L., Tjahjanto, D.D., Bieler, T.R., Raabe, D., 2010. Overview of constitutive laws, kinematics, homogenization and multiscale methods in crystal plasticity finite-element modeling: Theory, experiments, applications. Acta. Mater. 58, 1152-1211.

Saeidi, N., Ashrafizadeh, F., Niroumand, B., Barlat, F., 2015. EBSD study of micromechanisms involved in high deformation ability of DP steels. Mater. Des. 87, 130-137.

Segurado, J., Lebensohn, R.A., Llorca, J., Tomé, C.N., 2012. Multiscale modeling of plasticity based on embedding the viscoplastic self-consistent formulation in implicit finite elements. Int. J. Plast. 28, 124-140.

Sharma, R., Poulin, C.M., Knezevic, M., Miles, M.P., Fullwood, D.T., 2021. Micromechanical origins of remarkable elongation-to-fracture in AHSS TRIP steels via continuous bending under tension. Mater. Sci. Eng. A 825, 141876.

Shi, M., Gelisse, S., 2006. Issues on the AHSS forming limit determination, Proceedings of the IDDRG International Conference, Porto, Portugal, pp. 19-21.

Smith, A., Chen, Z., Lee, J.Y., Lee, M.G., Wagoner, R.H., 2014. Effective method for fitting complex constitutive equations. Int. J. Plast. 58, 100-119.

Sritharan, T., Chandel, R.S., 1997. Phenomena in interrupted tensile tests of heat treated aluminium alloy 6061. Acta. Mater. 45, 3155-3161.

Stout, M., Rollett, A., 1990. Large-strain Bauschinger effects in fcc metals and alloys. Metall. Mater. Trans. A 21, 3201-3213.

Tasan, C.C., Hoefnagels, J.P.M., Diehl, M., Yan, D., Roters, F., Raabe, D., 2014. Strain localization and damage in dual phase steels investigated by coupled in-situ deformation experiments and crystal plasticity simulations. Int. J. Plast. 63, 198-210.

Taupin, V., Pesci, R., Berbenni, S., Berveiller, S., Ouahab, R., Bouaziz, O., 2013. Lattice strain measurements using synchrotron diffraction to calibrate a micromechanical modeling in a ferrite–cementite steel. Materials Science and Engineering: A 561, 67-77.

Taylor, G., 1992. Thermally-activated deformation of BCC metals and alloys. Prog. Mater. Sci. 36, 29-61.

Taylor, G.I., 1938. Plastic strain in metals. Journal of the Institute of Metals 62, 307-324.

Turner, P.A., Tomé, C.N., 1994. A study of residual stresses in Zircaloy-2 with rod texture. Acta Metall. Mater. 42, 4143-4153.

Verma, R.K., Kuwabara, T., Chung, K., Haldar, A., 2011. Experimental evaluation and constitutive modeling of non-proportional deformation for asymmetric steels. Int. J. Plast. 27, 82-101.

Wagoner, R.H., Kim, J.H., Sung, J.H., 2009. Formability of advanced high strength steels. International Journal of Material Forming 2, 359.

Wagoner, R.H., Lim, H., Lee, M.-G., 2013. Advanced Issues in springback. Int. J. Plast. 45, 3-20.

Wen, W., Borodachenkova, M., Tomé, C.N., Vincze, G., Rauch, E.F., Barlat, F., Grácio, J.J., 2014. Mechanical behavior of Mg subjected to strain path changes: Experiments and modeling. International Journal of Plasticity.

Wenk, H.-R., Lutterotti, L., Vogel, S., 2003. Texture analysis with the new HIPPO TOF diffractometer. Nuclear Instruments and Methods in Physics Research Section A: Accelerators, Spectrometers, Detectors and Associated Equipment 515, 575-588.

Wenk, H.-R., Lutterotti, L., Vogel, S., 2010. Rietveld texture analysis from TOF neutron diffraction data. Powder Diffraction 25, 283-296.

Wilson, D.V., Bate, P.S., 1986. Reversibility in the work hardening of spheroidised steels. Acta Metall. 34, 1107-1120.

Wilson, D.V., Zandrahimi, M., Roberts, W.T., 1990. Effects of changes in strain path on work-hardening in CP aluminium and an Al-Cu-Mg alloy. Acta Metall. Mater. 38, 215-226.

Wollmershauser, J.A., Clausen, B., Agnew, S.R., 2012. A slip system-based kinematic hardening model application to in situ neutron diffraction of cyclic deformation of austenitic stainless steel. Int. J. Fatigue 36, 181-193.

Woo, W., Em, V.T., Kim, E.Y., Han, S.H., Han, Y.S., Choi, S.H., 2012. Stress–strain relationship between ferrite and martensite in a dual-phase steel studied by in situ neutron diffraction and crystal plasticity theories. Acta. Mater. 60, 6972-6981.

Xu, B., Jiang, Y., 2004. A cyclic plasticity model for single crystals. International Journal of Plasticity 20, 2161-2178.

Xue, X., Liao, J., Vincze, G., Sousa, J., Barlat, F., Gracio, J., 2016. Modelling and sensitivity analysis of twist springback in deep drawing of dual-phase steel. Mater. Des. 90, 204-217.

Yaddanapudi, K., Knezevic, M., Mahajan, S., Beyerlein, I.J., 2021. Plasticity and structure evolution of ferrite and martensite in DP 1180 during tension and cyclic bending under tension to large strains. Mater. Sci. Eng. A 820, 141536.

Yoshida, F., Uemori, T., Fujiwara, K., 2002. Elastic–plastic behavior of steel sheets under in-plane cyclic tension–compression at large strain. Int. J. Plast. 18, 633-659.

Zang, S.-l., Lee, M.-g., Hoon Kim, J., 2013. Evaluating the significance of hardening behavior and unloading modulus under strain reversal in sheet springback prediction. International Journal of Mechanical Sciences 77, 194-204.

Zecevic, M., Knezevic, M., 2015. A dislocation density based elasto-plastic self-consistent model for the prediction of cyclic deformation: Application to Al6022-T4. Int. J. Plast. 72, 200-217.

Zecevic, M., Korkolis, Y.P., Kuwabara, T., Knezevic, M., 2016. Dual-phase steel sheets under cyclic tension–compression to large strains: Experiments and crystal plasticity modeling. J. Mech. Phys. Solids 96, 65-87.

Zecevic, M., Pantleon, W., Lebensohn, R.A., McCabe, R.J., Knezevic, M., 2017. Predicting intragranular misorientation distributions in polycrystalline metals using the viscoplastic self-consistent formulation. Acta. Mater. 140, 398-410.

Zecevic, M., Upadhyay, M.V., Polatidis, E., Panzner, T., Van Swygenhoven, H., Knezevic, M., 2019. A crystallographic extension to the Olson-Cohen model for predicting strain path dependence of martensitic transformation. Acta. Mater. 166, 386-401.

Chapter 2:

Experimental characterization and crystal plasticity modeling for predicting load reversals in AA6016-T4 and AA7021-T79.

This chapter has been published in International Journal of Plasticity as: *"Experimental characterization and crystal plasticity modeling for predicting load reversals in AA6016-T4 and AA7021-T79",* Sowmya Daroju, Toshihiko Kuwabara, Rishabh Sharma, David T. Fullwood, Michael P. Miles, Marko Knezevic.

For this chapter, all the experimental results were provided by Professor Toshihiko Kuwabara, the simulated results were carried out in EPSC.

Experimental characterization and crystal plasticity modeling for predicting load reversals in AA6016-T4 and AA7021-T79

Sowmya Daroju[a], Toshihiko Kuwabara[b], Rishabh Sharma[c], David T. Fullwood[c], Michael P. Miles[d], Marko Knezevic[a,2]

[a]Department of Mechanical Engineering, University of New Hampshire, Durham, NH 03824, USA

[b]Division of Advanced Mechanical Systems Engineering, Institute of Engineering, Tokyo University of Agriculture and Technology, Tokyo 184-8588, Japan

[c]Department of Mechanical Engineering, Brigham Young University, Provo, UT 84602, USA

[d]Manufacturing Engineering Department, Brigham Young University, Provo, UT 84602, USA

Abstract

This paper describes the results and insights from a combined experimental and modeling investigation into the monotonic and load reversal deformation of aluminum alloys (AA) 6016-T4 and 7021-T79. In addition to providing the comprehensive data, particularities pertaining to the reversal deformation, including the hardening rates during monotonic tension, a linear and then a non-linear unloading, the Bauschinger effect (BE), and hardening rates during continuous straining in the opposite direction causing permanent softening, were analyzed and discussed as a function of loading history for both alloys. Moreover, the unloading deviation stress, reloading

[*] Corresponding author at: University of New Hampshire, Department of Mechanical Engineering, 33 Academic Way, Kingsbury Hall, W119, Durham, New Hampshire 03824, United States. Tel.: 603 862 5179; fax: 603 862 1865.
E-*mail address*: marko.knezevic@unh.edu (M. Knezevic).

stress differential, reloading softening stress, and ratcheting strain were determined as a function

of pre-load strain. Interestingly, the alloys show contrasting characteristics in terms of permanent

softening and reloading yield stress differential phenomena. The data were predicted and

interpreted using an elasto-plastic self-consistent (EPSC) crystal plasticity model. The model

considers anisotropic elasticity, dislocation density-based hardening, and intra-granular slip

system-level backstress fields in addition to accounting for inter-granular stress fields. The

hardening law and the backstress law parameters were established using a portion of the

measured data for both alloys. Good predictions of the remaining data proved the ability of

crystal plasticity to account for the co-dependent nature of crystallographic glide and the sources

of hardening originating from the deformation history-dependent dislocation density evolution

and backstress fields. Comparison of the experimental and modeling results revealed that the

unloading behavior is primarily driven by backstress, the BE is governed by backstress and inter-

granular stresses, and the hardening rates upon load reversals are controlled primarily by the

strain-path sensitive evolution of dislocation density.

1. Introduction

Simulations play an important role in evaluation of component performances in service and,

especially, in optimization of metal forming operations. Reliability of such simulations is

dependent on a material model, which describes the relations between the imposed boundary

conditions on a workpiece and the resulting deformation. As metal forming operations involve

non-monotonic deformation paths with frequent unloading, the material model must be able to

describe the material response under such deformation conditions. For example, bending-unbending of metallic sheets drawn over a die radius includes tension followed by compression (Chun et al., 2002; Knezevic et al., 2019; Poulin et al., 2020; Wagoner et al., 2013). The material also undergoes unloading - the so called springback deformation, which always happens after removal of a part from a die (Boger et al., 2005; Wagoner et al., 2013). Predicting such behavior requires elasto-plastic material models able to predict unloading, transients in yield stress (the Bauschinger effect, BE), and changes in the work hardening rates during strain-path changes, in addition to anisotropic hardening rate during monotonic deformation. These phenomena originate from the evolution of the underlying microstructure as summarized next.

The unloading strains consist of an initial elastic response followed by a small nonlinear component owing to small scale yielding, attributed to a dislocation relaxation phenomenon (Mompiou et al., 2012; Pavlina et al., 2015; Sritharan and Chandel, 1997; Wagoner et al., 2013; Yoshida et al., 2002; Zhou and LeSar, 2012). The small scale back-flow during unloading is a result of accumulated micro backstress fields arising from dislocation pile-ups at grain boundaries (Seeger, 1957; Weng, 1979) or non-deforming particles (Brown and Clarke, 1975; Tanaka and Mori, 1970). The back-flow is accommodated by some re-emission of the dislocations from the pile-ups (Mompiou et al., 2012; Sritharan and Chandel, 1997), while relaxing the micro backstress fields. Since the amount of plastic deformation before unloading influences the magnitude of non-linear unloading, accurate modeling of prior plastic deformation is essential to capture the non-linear unloading using a constitutive model.

The Bauschinger effect refers to two different values of the yield stress for a material, measured depending on the loading sense, whether tension or compression (Bauschinger, 1886). The higher value occurs when the material is unloaded and then reloaded in the same sense,

while the lower value occurs when the material is unloaded and then reloaded in the opposite sense. The BE effect can occur in deformation of polycrystals from inter- and intra-granular sources (Nieh and Nix, 1986; Sauzay, 2008; Stout and Rollett, 1990) as well as in single crystals solely from intra-granular sources (Buckley and Entwistle, 1956; Demir and Raabe, 2010; Gough et al., 1927; Greetham and Honeycombe, 1960). The microstructural description of the BE is well documented in (Abel, 1987; Bate and Wilson, 1986a).

In single crystals, hard dislocation walls due to high dislocation density separated by soft regions due to low dislocation density can induce intra-granular long-range internal stresses (LRIS) (Kassner et al., 2013; Mughrabi, 1983). Geometrically necessary dislocations maintain compatibility at the interface between such hetero-structured regions giving rise to hardening. During deformation the internal stresses develop in the opposite direction from the applied loading. Upon reloading in the opposite direction, these internal stresses combine with the loading and cause a drop in the yield. In precipitation hardened alloys, such as Al alloys, precipitates as obstacles to mobile dislocations cause the BE. Dislocations shear precipitates on the slip plane until the array of obstacles becomes closely spaced and sufficiently strong to inhibit the forward motion. After the applied stress is removed, the dislocations relax and re-equilibrate locally (Orowan, 1948). If the strain-path is reversed, the backward stress necessary to move the dislocations is lower than the forward stress because the array of obstacles on the same path has been overcome during the forward motion and is less dense than the array that arrested the dislocations during the forward motion (Orowan, 1959). Another distribution of precipitates will eventually arrest dislocations moving in the opposite direction but the BE has manifested itself before that. The anisotropy in resistance to dislocation glide between forward and reverse directions causes the BE. In the case of non-shearable precipitates, dislocations bow

out and then form loops as they break through the obstacles. The loops exert a repulsive force on the dislocations of the same sign moving in the same direction but attractive force for the dislocations of the same sign moving in the opposite direction, which manifests itself as the BE. These second phase particles induce a composite effect, where the particles share the applied stress and thus reduce the amount of stress in the matrix. The matrix then flows at a larger applied stress than it would in the absence of the particles. This load sharing phenomena can be an additional source of backstress fields (Bate et al., 1981, 1982).

In polycrystalline materials, the BE effect has additional sources in inter-granular stress fields. Some grains are harder and some are softer depending on their crystal lattice orientation with respect to the loading direction. The inter-granular stress fields arise due to strain incompatibilities between adjacent soft/hard grains during forward loading. These stress fields combine with the stress applied in the reverse direction, which can manifest in the drop of the yield stress (Weng, 1979, 1980). Importantly, these inter-granular stress fields are strongly linked to the evolutions of texture and grain structure with plastic strain, which promote the development of plastic anisotropy.

Following the BE, a change in the work hardening rate may occur (Hasegawa et al., 1975a; Kitayama et al., 2013b; Stout and Rollett, 1990; Wilson et al., 1990). As a result, an offset between the reverse and the forward flow stress arises (Bate and Wilson, 1986b; Orowan, 1959; Zang et al., 2013). The offset is referred to as the permanent softening. The effect stems from a tradeoff between the annihilation of dislocations formed during the forward deformation and buildup of new dislocations during deformation in the opposite direction.

A range of macroscopic models have been formulated to predict cyclic deformation of alloys relying on a combination of isotropic and linear or nonlinear kinematic hardening laws

(Armstrong and Frederick, 1966; Chaboche and Rousselier, 1983; Chaboche, 1977; Chaboche, 2008; Hu et al., 1992; McDowell, 1992). These formulations are computationally efficient and suitable to easily implement in finite element (FE) codes. These models mathematically represent the above mechanistic sources of backstress fields using a set of model parameters and do not distinguish between intra- and inter-granular sources of backstress. Moreover, these models have a large number of adjustable parameters, which demand specialized mechanical tests and inverse methodologies for their identification (Feng et al., 2020; Smith et al., 2014). The models are also restricted to a specific material state used in testing and often to the specific loadings used during the model adjusting process.

Models based on crystal plasticity provide more flexibility to incorporate the mechanistic sources of backstress fields along with the crystallography of deformation mechanisms and texture. These models are not constrained to a specific deformation condition or a given material state and can predict the development of the anisotropy caused by the evolution of textural and microstructure (Lopes et al., 1999). To link response of individual grains to the response of a polycrystalline aggregate, several homogenization schemes have been formulated. These range from upper-bound Taylor (Knezevic et al., 2008; Taylor, 1938) to mean-field self-consistent (SC) (Lebensohn and Tomé, 1993), and finally to spatial full-field formulations (Kalidindi et al., 1992; Kalidindi et al., 2006; Lebensohn et al., 2012). While the full-field models are more accurate because of accounting for grain-to-grain interactions, the Taylor and SC models are computationally more efficient and effective in capturing the flow stress response and texture evolution. Additionally, the Taylor and SC models have been coupled with FE codes to relax the homogenization assumptions (Barrett and Knezevic, 2019; Barrett et al., 2020; Knezevic et al., 2013; Segurado et al., 2012; Zecevic et al., 2017a; Zecevic and Knezevic, 2017, 2019; Zecevic et

al., 2016). The assumptions become relaxed because the deformation varies spatially from point to point across the FE mesh.

The present work utilizes a recent implicit formulation of the elasto-plastic self-consistent (EPSC) model, integrating anisotropic elasticity, a dislocation-based hardening law, and a slip system backstress law (Zecevic and Knezevic, 2019) to study the load reversal deformation of AA6016-T4 and AA7021-T79. A large body of mechanical testing data for sheets of the alloys is presented and used to calibrate and validate the model for each alloy. To initialize the model, texture and grain structure were measured using electron backscattered diffraction (EBSD). The model parameters are calibrated for each alloy using part of the test data. Based on the performance of the model against the remaining data, the model is validated as a tool for predicting hardening rates during monotonic tension and compression, linear and then a non-linear unloading, the BE, and hardening rates during continuous straining in the opposite direction along with the permanent softening, as a function of loading history for both alloys. The experimental data, simulation results, and insights pertaining to the monotonic and load reversal behavior of the alloys are presented and discussed in the paper.

2. Materials and experiments

We study deformation behavior of precipitation-hardened alloys in sheet form, commonly used for various lightweighting efforts in the automotive industry, AA6016-T4 and AA7021-T79 (supplied by Commonwealth Rolled Products). The investigated AA6016-T4 was a 1.1 mm thick sheet, aged for about one year. It is a heat treatable low copper, Al–Si–Mg alloy in the temper T4 condition. Table 1 shows its chemical composition. The Mg and Si content are set to produce Mg_2Si precipitates (Jaafar et al., 2012). The following precipitation sequence strengthens the

alloy (Miao and Laughlin, 1999): supersaturated solid solution (sss) → Guinier–Preston (GP) zones → needle-like β'' → rod-like β' + lath-like precipitates → β + Si. These precipitate are barriers to dislocation motion, with the β'' phase proving the most effective for hardening (Eskin and Kharakterova, 2001). The investigated AA7021-T79 was a 2.5 mm thick sheet, also aged for about a year. The alloy was in T79 temper condition. Table 1 shows its chemical composition. Heat treatment of this Al-Zn-Mg-Cu alloys result in a typical precipitation sequence as follows: sss → GP zones (coherent) → η' (metastable and semicoherent) → η ($MgZn_2$ – incoherent resulting from over-aging) (Couturier et al., 2017; Mirihanage et al., 2021; Prabhu, 2015). Unfortunately, the use of this alloy in industry is restricted by its low formability at room temperature. Warm forming greatly improves its formability with a possibility to form some precipitates dynamically. The alloy is being increasingly evaluated for various application as a part of an industry-wide lightweighting effort, while the AA6016-T4 has already been employed for components like exterior body panels, as it can be formed at room temperature. The AA6016-T4 is usually strengthened during the subsequent paint bake process (about 175°C for 20 minutes). The paint bake results in final properties that are stronger than T4, but not quite at the level of T6 condition. In addition to high industrial relevance, these precipitation hardened alloys develop backstress fields and their effects on the load reversal behavior deserve to be systematically studied (Anjabin et al., 2014; Bhattacharyya et al., 2018; Sehitoglu et al., 2005; Zecevic and Knezevic, 2015).

Experimental setups have been developed to test materials under strain path reversals including forward - reverse torsion (Chen et al., 1999; Stout and Rollett, 1990), forward - reverse shear (Gracio et al., 2004), tension - torsion (Brown, 1970), tension - shear (Barlat et al., 2003; Peeters et al., 2001), and tension - compression (Boger et al., 2005; Dietrich and Turski, 1978;

Szczepiński, 1990; Tan et al., 1994; Yoshida et al., 2002). In this work, the investigated alloys are tested monotonically in tension and compression and in single and multiple tension-compression cycles to various pre-strain levels. Specimens were cut out of the sheets with orientations along the rolling direction (RD) and the transverse direction (TD) according to the dimensions provided in the appendix. To verify that the tension portion of the cyclic curves matches data of regular tension tests, additional tensile bars were made according to the ASTM E-8 standard and tested on an MTS Landmark 370 servo-hydraulic testing machine. During these experiments, the strain was measured using the VIC-2D Digital Image Correlation (DIC) system. The load reversal experiments were performed on the testing setup developed in earlier works (Kuwabara et al., 2009; Kuwabara et al., 2001; Verma et al., 2011). The load cell used was TCLM -50KNB (Tokyo Sokki Kenkyujo Co., Max. load: 50 kN). The strain was measured using high-elongation strain-gages, YFLA-2-1L (Tokyo Measuring Instruments Laboratory Co.). A nominal strain rate of 10^{-4} /s was used for all tests. All tests were performed at room temperature.

Table 1. Chemical composition of AA6016-T4 and AA7021-T79 (wt%).

	Al	Si	Mg	Fe	Mn	Zn	Cu	Ti	Cr
AA-6016 T4	Balance	1.5	0.6	0.5	0.2	0.2	0.2	0.15	0.1
AA-7021-T79	Balance	0.058	1.4	0.2	0.057	5.8	0.19	-	-

3. Modeling framework

This section summarizes the EPSC polycrystal model used for modeling of the alloys. The particular version of the code is described in (Zecevic and Knezevic, 2019). The EPSC model treats a polycrystalline aggregate as a collection of ellipsoids/grains with a specific crystal lattice orientation and a volume fraction per orientation. Shape and crystallography of elipsoids evolve with plastic strain. Polycrystalline properties are obtained through the use of the SC homogenization scheme. In this scheme, each ellipsoid/grain is considered as an elasto-plastic inclusion embedded in the homogeneous-equivalent-medium (HEM). The HEM properties are the sought properties of the polycrystalline aggregate. In the model description below, we use "·" to denote a contracted/dot product and "$\otimes$" notation to denote an outer/tensor product. Tensors are denoted by bold letters, while scalars are not bold.

The constitutive relation between Jaumann stress rate, $\hat{\boldsymbol{\sigma}}$, and strain rate, $\dot{\boldsymbol{\varepsilon}}$, is used in EPSC at both a single crystal-level and at a polycrystalline aggregate-level (Nagtegaal and Veldpaus, 1984; Neil et al., 2010)

$$\hat{\boldsymbol{\sigma}} = \mathbf{L}\dot{\boldsymbol{\varepsilon}} = \dot{\boldsymbol{\sigma}} + \boldsymbol{\sigma}\mathbf{W} - \mathbf{W}\boldsymbol{\sigma} \tag{1}$$

At the polycrystalline level, the tensors, $\boldsymbol{\sigma}$, $\mathbf{W}$, and $\mathbf{L}$ are the Cauchy stress, spin, and tangent stiffness, respectively; values at the single crystal-level are represented with a superscript, c as $\boldsymbol{\sigma}^c$, $\mathbf{W}^c$, and $\mathbf{L}^c$. Given the crystal quantities, the macroscopic Cauchy stress rate is obtained as $\dot{\boldsymbol{\sigma}} = \hat{\boldsymbol{\sigma}} + \langle \mathbf{W}^c \boldsymbol{\sigma}^c \rangle - \langle \boldsymbol{\sigma}^c \mathbf{W}^c \rangle = \mathbf{L}\dot{\boldsymbol{\varepsilon}} + \langle \mathbf{W}^c \boldsymbol{\sigma}^c \rangle - \langle \boldsymbol{\sigma}^c \mathbf{W}^c \rangle$, with $\mathbf{L}$ obtained using the standard iterative SC procedure (Eshelby, 1957; Lipinski and Berveiller, 1989; Turner and Tomé, 1994) from the volume average $\hat{\boldsymbol{\sigma}} = \langle \hat{\boldsymbol{\sigma}}^c \rangle$ and $\dot{\boldsymbol{\varepsilon}} = \langle \dot{\boldsymbol{\varepsilon}}^c \rangle$. Hooke's constitutive law is used at the crystal-level

$$\hat{\boldsymbol{\sigma}}^c = \mathbf{L}^c \dot{\boldsymbol{\varepsilon}}^c = \mathbf{C}^c (\dot{\boldsymbol{\varepsilon}}^c - \dot{\boldsymbol{\varepsilon}}^{pl,c}) - \boldsymbol{\sigma}^c tr(\dot{\boldsymbol{\varepsilon}}^c), \tag{2}$$

where $\mathbf{C}^c$ and $\dot{\boldsymbol{\varepsilon}}^{pl,c}$ are the elastic stiffness and the plastic strain rate tensors per crystal c,

respectively. The plastic strain rate tensor is

$$\dot{\boldsymbol{\varepsilon}}^{pl,c} = \sum_s \mathbf{m}^s \dot{\gamma}^s \tag{3}$$

where $\mathbf{m}^s = \frac{1}{2}(\mathbf{b}^s \otimes \mathbf{n}^s + \mathbf{n}^s \otimes \mathbf{b}^s)$ is the symmetric Schmid tensor and $\dot{\gamma}^s$ is the shearing

strain rate. The former is defined by the slip system geometry: $\mathbf{b}^s$ is the Burger's vector and $\mathbf{n}^s$

is the slip system plane normal. The index, s, enumerates available slip systems in every grain c.

Slip system activation is based on the following two conditions

$$\mathbf{m}^s \cdot \boldsymbol{\sigma}^c - \tau_{bs}^s = \tau_c^s, \tag{4}$$

$$\mathbf{m}^s \cdot \hat{\boldsymbol{\sigma}}^c - \dot{\tau}_{bs}^s = \dot{\tau}_c^s, \tag{5}$$

where, τ_c^s, is the resistance to slip and τ_{bs}^s is the slip system-level backstress determining the

kinematic hardening effects (Wollmershauser et al., 2012). Condition 4 implies that the stress

state is on the single crystal yield surface. Condition 5 ensures consistency that the stress state

stays on the single crystal yield surface (Knockaert et al., 2000; Zecevic et al., 2019). The

quantities evolve using

$$\dot{\tau}_c^s = \sum_{s'} h^{ss'} \dot{\gamma}^{s'}, \tag{6}$$

$$\dot{\tau}_{bs}^s = \sum_{s'} h_{bs}^{ss'} \dot{\gamma}^{s'}, \tag{7}$$

where, $h^{ss'}$ and $h_{bs}^{ss'}$ are the hardening matrix consisting of derivatives, $h^{ss'} = \frac{\partial \tau_c^s}{\partial \gamma^{s'}}$, and the

backstress matrix consisting of derivatives, $h_{bs}^{ss'} = \frac{\partial \tau_{bs}^s}{\partial \gamma^{s'}}$. Remaining to define at the single crystal

level $\mathbf{L}^c = \mathbf{C}^c - \mathbf{C}^c \sum_s \mathbf{m}^s \otimes \left(\sum_{s'} \left(X^{ss'} \right)^{-1} \mathbf{m}^{s'} \left(\mathbf{C}^c - \boldsymbol{\sigma}^c \otimes \mathbf{i} \right) \right) - \boldsymbol{\sigma}^c \otimes \mathbf{i}$ with $X^{ss'} = h^{ss'} +$

$h_{bs}^{ss'} + \mathbf{C}^c \cdot \mathbf{m}^s \otimes \mathbf{m}^{s'}$.

Finally, to calculate the reorientation of individual crystals with plastic strain, the lattice spin tensor, $\mathbf{W}^c$, is

$$\mathbf{W}^c = \mathbf{W}^{app} + \boldsymbol{\Pi}^c - \mathbf{W}^{p,c} \tag{8}$$

with $\mathbf{W}^{app}$ as the applied rotation rate, $\boldsymbol{\Pi}^c$ as the antisymmetric part of the Eshelby tensor (Lebensohn and Tomé, 1993), and $\mathbf{W}^{p,c}$ as the plastic spin, which is obtained from the shearing rates as

$$\mathbf{W}^{p,c} = \sum_s \mathbf{q}^s \dot{\gamma}^s, \tag{9}$$

with $\mathbf{q}^s = \frac{1}{2} (\mathbf{b}^s \otimes \mathbf{n}^s - \mathbf{n}^s \otimes \mathbf{b}^s)$.

Next, we summarize the evolution laws for slip resistance and backstress to define the above partial derivatives. To this end, the EPSC model incorporates a strain-path sensitive hardening law based on dislocation density for the evolution of slip system resistance and a slip system-level backstress law to affect the activation resolved shear stress. These laws in combination with the latent hardening are aimed at predicting the anisotropic mechanical response of the alloys during monotonic tension/compression as well as the particularities pertaining to the load reversal deformation i.e. the nonlinear unloading, the BE, and changes in the hardening rates during load reversals. It should also be emphasized that since the model is elasto-plastic, the inter-granular stresses are obtained using the SC homogenization. Modeling anisotropic elasticity is essential in attempting to predict the response under non-monotonic loading and, especially, under unloading of pre-strained alloys because of the inter-granular stress fields.

In the formulations, *s+* and *s-* denote a positive and a negative slip direction on the given slip plane for every *s* belonging to a slip family/mode α. Resistance to slip involves three terms

$$\tau_c^s = \tau_0^\alpha + \tau_{forest}^s + \tau_{debris}^\alpha, \tag{10}$$

with τ_0 representing the friction Peierls stress, barrier strengthening, solid solution strengthening, and precipitation strengthening but otherwise dislocation free fixed value of slip resistance, while τ_{forest}^s and τ_{debris} are evolving terms with statistically stored forest and debris dislocation populations, respectively. These last two terms are

$$\tau_{forest}^s = b\chi G\sqrt{\sum_{s'} L^{ss'}\rho_{tot}^{s'}} \tag{11}$$

$$\tau_{debris}^\alpha = 0.086Gb\sqrt{\rho_{deb}}\log\left(\frac{1}{b\sqrt{\rho_{deb}}}\right) \tag{12}$$

Here, *b* is the Burgers vector ($b = 2.86 \ 10^{-10}$ m for Al), χ is an interaction constant (Lavrentev, 1980; Mecking and Kocks, 1981) ($\chi = 0.9$), ρ_{tot}^s is the total density of forest dislocations for the sth slip system, ρ_{deb} is the density of debris dislocations, G (26 GPa) is the shear modulus, and $L^{ss'}$ is a latent hardening interaction matrix (Zecevic and Knezevic, 2018).

The total population of forest dislocations consists of

$$\rho_{tot}^s = \rho_{for}^s + \rho_{rev}^{s^+} + \rho_{rev}^{s^-}, \tag{13}$$

where ρ_{for}^s is the forward density, while $\rho_{rev}^{s^+}$ and $\rho_{rev}^{s^-}$ are the reversible densities associated with the *s+* and *s-* slip system directions. These densities of dislocations evolve with shearing on slip systems (Kitayama et al., 2013a; Zecevic and Knezevic, 2019)

(If $d\gamma^{s^+} > 0$)

$$\frac{\partial \rho_{for}^{s}}{\partial \gamma^{s}} = (1-p)k_1^{\alpha}\sqrt{\sum_{s\prime} g^{ss\prime}\rho_{tot}^{s\prime}} - k_2^{\alpha}(\dot{\varepsilon},T)\rho_{for}^{s}, \tag{14}$$

$$\frac{\partial \rho_{rev}^{s^+}}{\partial \gamma^{s}} = pk_1^{\alpha}\sqrt{\sum_{s\prime} g^{ss\prime}\rho_{tot}^{s\prime}} - k_2^{\alpha}(\dot{\varepsilon},T)\rho_{rev}^{s^+}, \tag{15}$$

$$\frac{\partial \rho_{rev}^{s^-}}{\partial \gamma^{s}} = -k_1^{\alpha}\sqrt{\sum_{s\prime} g^{ss\prime}\rho_{tot}^{s\prime}}\left(\frac{\rho_{rev}^{s^-}}{\rho_0^{s}}\right)^{m}, \tag{16}$$

(If $d\gamma^{s^-} > 0$)

$$\frac{\partial \rho_{for}^{s}}{\partial \gamma^{s}} = (1-p)k_1^{\alpha}\sqrt{\sum_{s\prime} g^{ss\prime}\rho_{tot}^{s\prime}} - k_2^{\alpha}(\dot{\varepsilon},T)\rho_{for}^{s}, \tag{17}$$

$$\frac{\partial \rho_{rev}^{s^+}}{\partial \gamma^{s}} = -k_1^{\alpha}\sqrt{\sum_{s\prime} g^{ss\prime}\rho_{tot}^{s\prime}}\left(\frac{\rho_{rev}^{s^+}}{\rho_0^{s}}\right)^{m}, \tag{18}$$

$$\frac{\partial \rho_{rev}^{s^-}}{\partial \gamma^{s}} = pk_1^{\alpha}\sqrt{\sum_{s\prime} g^{ss\prime}\rho_{tot}^{s\prime}} - k_2^{\alpha}(\dot{\varepsilon},T)\rho_{rev}^{s^-}, \tag{19}$$

with $\rho_{for}^{s}(\gamma^{s}=0) = \rho_{initial}^{s}$, $\rho_{rev}^{s^+}(\gamma^{s}=0) = 0$ and $\rho_{rev}^{s^-}(\gamma^{s}=0) = 0$. In the above equations, k_1 is a fitting hardening parameter controlling the rate of dislocation density increase, while k_2 is calculated to represent a rate-sensitive term controlling recovery of dislocations (Beyerlein and Tomé, 2008), p is a reversibility parameter in the range from 0 to 1 (established to be 0.2 for Al alloys), $g^{ss\prime}$ is another interaction matrix populated with 1.0 (Khadyko et al., 2016; Kocks et al., 1991; Teodosiu and Raphanel, 1991), m is another parameter controlling the rate of dislocation recombinations (the value is set to 0.5 (Wen et al., 2015)), and ρ_0^{s} is the total density of dislocations at the strain-path reversal on the system, s^{th} (Kitayama et al., 2013a).

The value of k_2 is calculated based on the following relation (Beyerlein and Tomé, 2008)

$$\frac{k_2^\alpha}{k_1^\alpha} = \frac{\chi b}{g}\left(1 - \frac{k_B T}{D b^3} \ln\left(\frac{\dot{\varepsilon}}{\dot{\varepsilon}_0}\right)\right), \tag{20}$$

with the Boltzmann constant, k_B, a reference strain rate, $\dot{\varepsilon}_0 = 10^7$, drag stress, D, and an

effective activation enthalpy, g. The debris density of dislocation is incremented based on

$$d\rho_{deb} = \sum_s q b \sqrt{\rho_{deb}}\, k_2^\alpha \rho_{tot}^s |d\gamma^s|, \tag{21}$$

with a fitting parameter q for the rate of dislocation recovery.

It remains to define a law for the evolution of backstress to calculate the backstress matrix, $h_{bs}^{ss'}$. Intra-granular sources of backstress are modeled by the phenomenological law as follows (Zecevic and Knezevic, 2019)

$$\tau_{bs}^s = \mathbf{m}^s \cdot \boldsymbol{\sigma}_{bs}^c = \tau_{bs,sys}^s + 2\sum_{s'} \mathbf{m}^s \cdot \mathbf{m}^{s'} \tau_{bs,sys*}^{s'}, \tag{22}$$

where

$$\tau_{bs,sys*}^{s'} = \begin{cases} \tau_{bs,sys}^{s'} & \text{if } \tau_{bs,sys}^{s'} > 0 \\ 0 & \text{if } \tau_{bs,sys}^{s'} < 0 \end{cases} \tag{23}$$

In the formulation, $\boldsymbol{\sigma}_{bs}^c$ is the backstress tensor based on the contribution from the slip system-level sources over s' when $s' \neq s$. The slip system-level sources are modeled using (if $d\gamma^{s^+} > 0$ and $\tau_{bs,sys}^{s^+} > 0$)

$$\tau_{bs,sys}^{s^+} = \tau_{bs}^{sat}\left(1 - \exp\left(-v\gamma^{s^+}\right)\right), \tag{24}$$

$$\tau_{bs,sys}^{s^-} = -A\tau_{bs,sys}^{s^+}, \tag{25}$$

(if $d\gamma^{s^+} > 0$ and $\tau_{bs,sys}^{s^+} < 0$)

$$\tau_{bs,sys}^{s^+} = -(A+1)\tau_{bs}^{sat} \exp\left(-\frac{\gamma^{s^-}}{\gamma_b}\right) + \tau_{bs}^{sat}, \tag{26}$$

$$\tau_{bs,sys}^{s^-} = -\frac{1}{A}\tau_{bs,sys}^{s^+}. \tag{27}$$

The law involves a saturation value, τ_{bs}^{sat}, a parameter governing an asymmetric evolution in $s+$ and $s-$, A, the denominator, γ_b, and a multiplier, ν, as fitting constants. The shearing strain, γ^s, is a value at the local load reversal. Important to note is that $\tau_{bs}^{s^+}$ opposes the driving force in s^+: $\mathbf{m}^{s+} \cdot \boldsymbol{\sigma}^c - \tau_{bs}^{s^+} = \tau_c^s$, implying that $\tau_{bs}^{s^+}$ reduces the driving force. However, $\tau_{bs}^{s^-}$ aids the driving force in s^-: $\mathbf{m}^{c,s-} \cdot \boldsymbol{\sigma}^c - \tau_{bs}^{s^-} = \tau_c^s$.

4. Results

This section presents the experimental results first including texture and flow stress curves and then modeling results including calibration and verification.

4.1 Experimental

Fig. 1 shows pole figures depicting texture in the alloys, while inverse orientation maps collected using EBSD depicting grain structure are provided in the appendix. Texture is based on multiple EBSD scans. As expected, a cube texture component is predominant in the pole figures.

Fig. 2 shows measured true stress versus logarithmic strain curves recorded during tension-compression-tension strain path reversals. The first loading is monotonic tension to a given pre-strain level. The second strain-path is compression to zero strain (1st reversal). The third strain-path is tension to fracture or to a detachment of the strain gauge (2nd reversal). The materials

66

exhibit typical decreasing work hardening rate during the monotonic tension, which is normal for plasticity facilitated by crystallographic slip. Upon the 1st reversal, the alloys exhibit a linear followed by a nonlinear portion of unloading. Macro yield points during unloading are identified (σ_U) at approximately 0.001 offset. The level of pre-strain increases the magnitude of macro yield stress but decreases the extent of the linear unloading. The extent of linear and also nonlinear unloading is greater for the stronger alloy. The reduction of the yield stress achieved during the monotonic pre-straining to that during reverse straining is the BE or transient softening. Essentially, the resistance to dislocation glide in the reverse sense is less than in the forward sense. Like nonlinear unloading, the BE is enhanced with strength. After the transient softening comes the permanent softening. The phenomenon is depicted in the primed figures of Fig. 2. However, it is prominent only for the softer alloy. There is no lowering of the flow curves when the reverse stress-strain curves are plotted in the same direction as during the prior straining for AA7021-T79.

Fig. 3 shows comparisons between the monotonic tension and the 1st and 2nd reversals to observe the yielding differentials and successive hardening rates for the alloys. While transients after the 1st reversal and after the 2nd reversal are similar for AA6016-T4, they are smaller after the 2nd reversal for AA7021-T79. As the elasto-plastic transition upon the reversals (1st and the 2nd) is prolonged for both alloys, the strain hardening rates are reduced compared to those during the forward tension for AA6016-T4 but not for AA7021-T79. Interestingly, the strain hardening in compression substantially surpasses that of tension causing positive yield differentials for AA6016-T4. Such positive yield differential increases with pre-strain. However, the yield differential is much smaller for AA7021-T79. Upon macroscopic re-yielding, the rates of strain hardening are restored for both alloys. The yield differential behavior after the 2nd reversal is

similar to that after the 1st reversal for AA6016-T4 but even smaller for AA7021-T79. The origin of these phenomena will be described and discussed later.
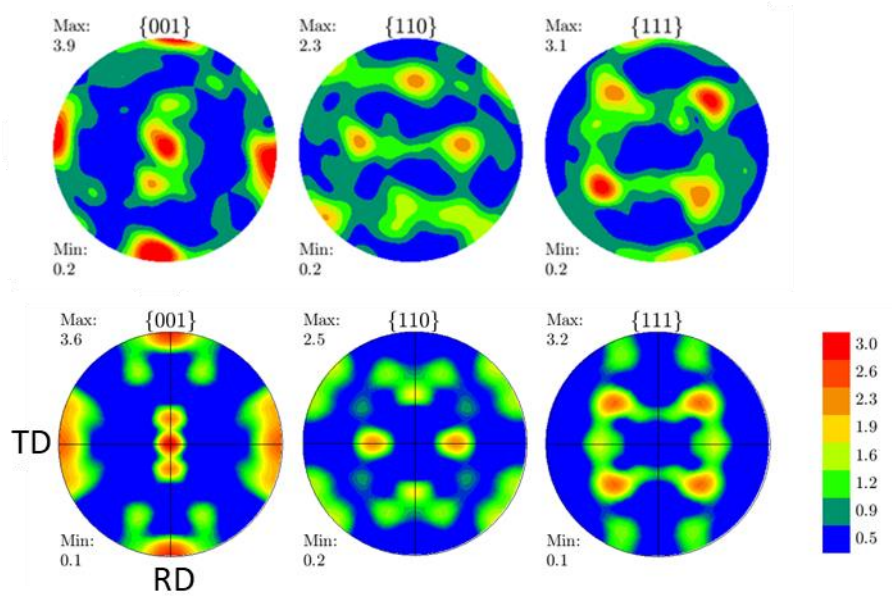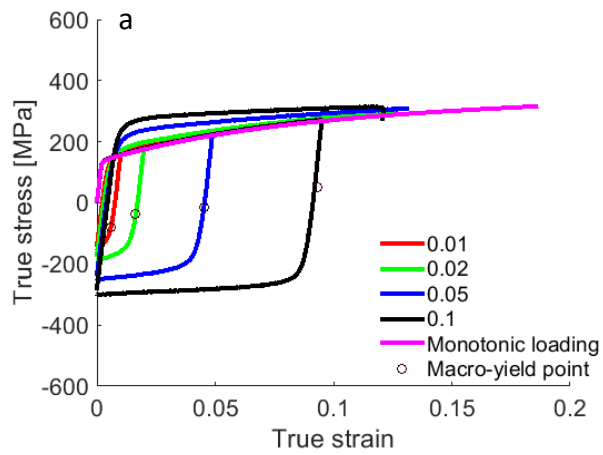

Figure 1. Pole figures showing measured initial texture for AA6016-T4 temper 1.1 mm thick sheet aged for about one year (top) and AA7021-T79 temper 2.5 mm thick sheet aged for about a year (bottom).
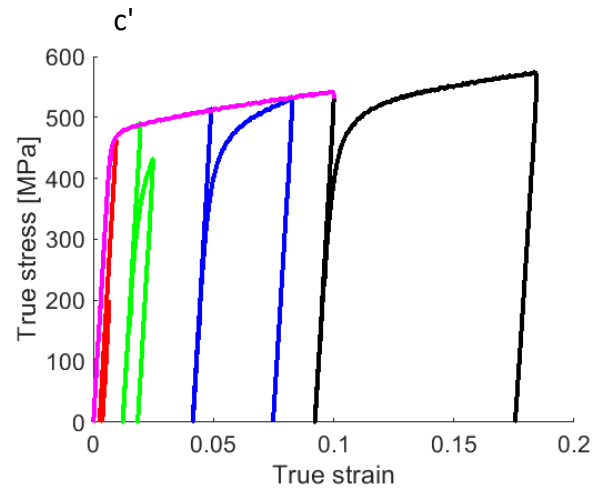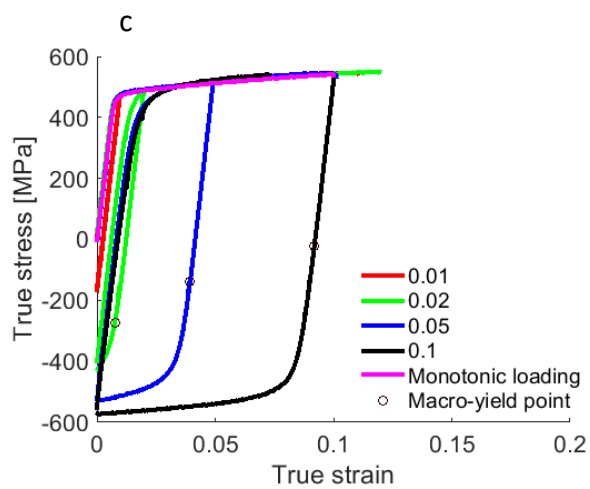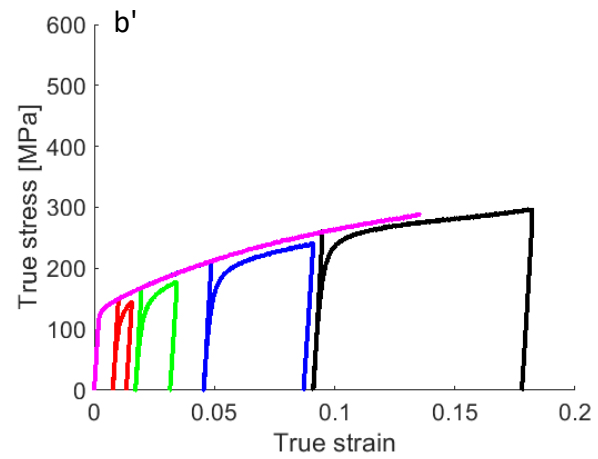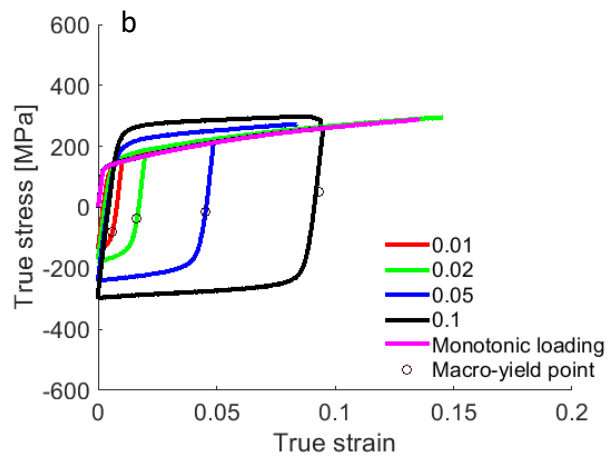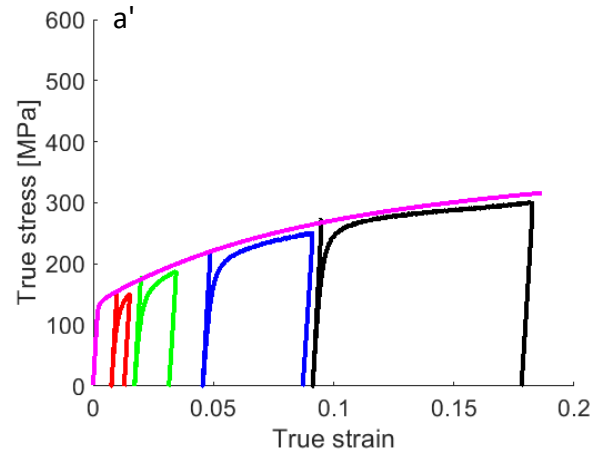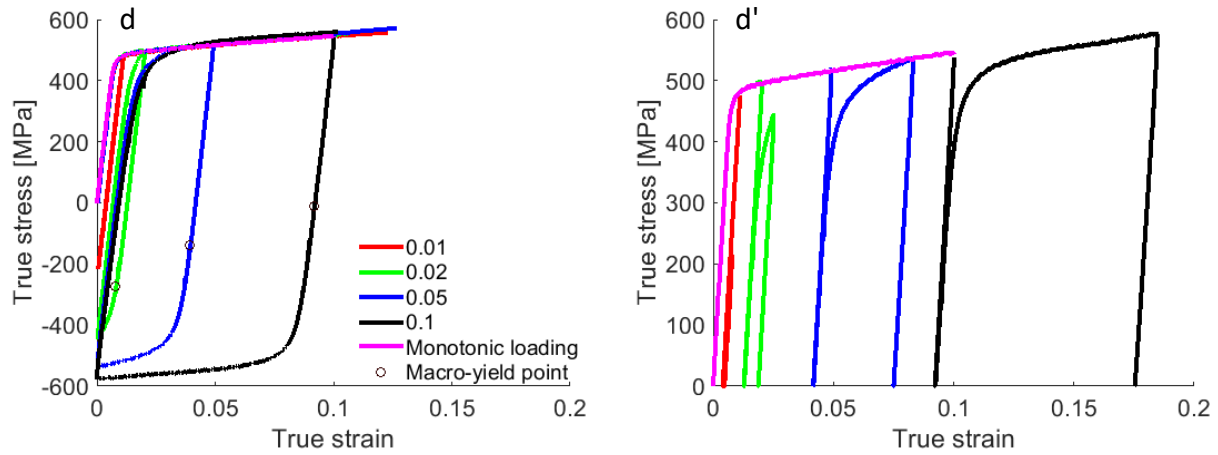
Figure 2. True stress vs. true strain curves measured at room temperature during strain path reversals at four pre-strain levels in tension as indicated in the legends followed by compression to zero and then tension to fracture for AA6016-T4 along (a) RD and (b) TD and for AA7021-T79 along (c) RD and (d) TD. Macro-yield points during unloading and compression at 0.001 strain offset are indicated (σ_U). Comparison of monotonic loading in tension versus the 1st reversal (compression) curves as a function of accumulated true strain showing the permanent softening phenomenon for AA6016-T4 along (a') RD and (b') TD and for AA7021-T79 along (c') RD and (d') TD. Legends in the 'unprimend' plots apply to the corresponding 'primed' plots.
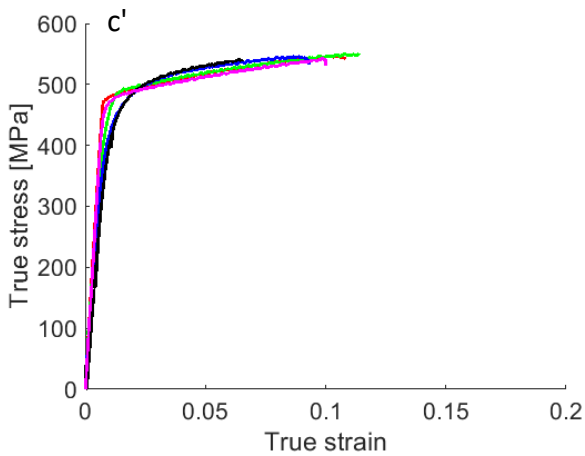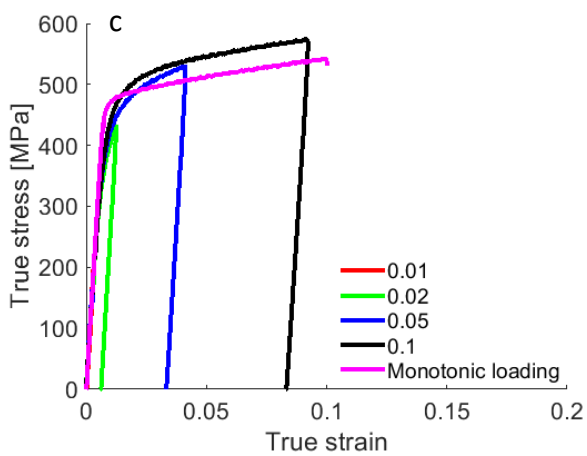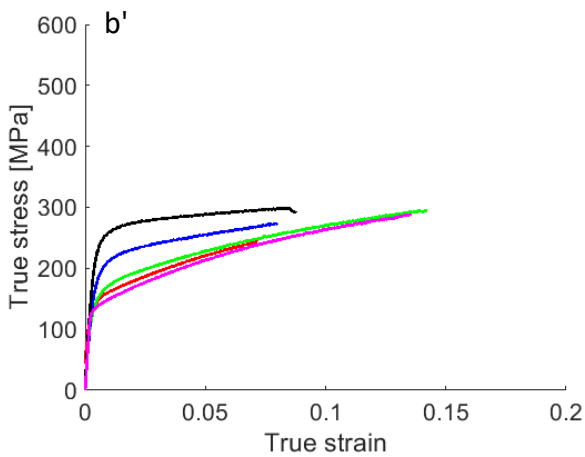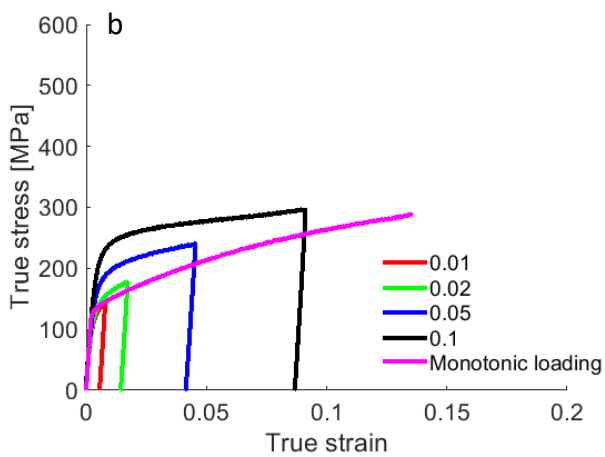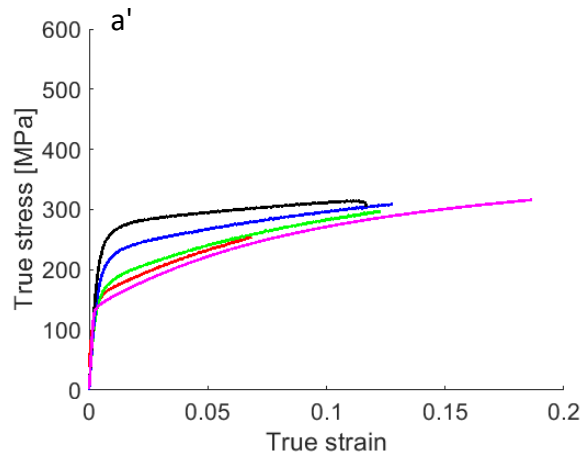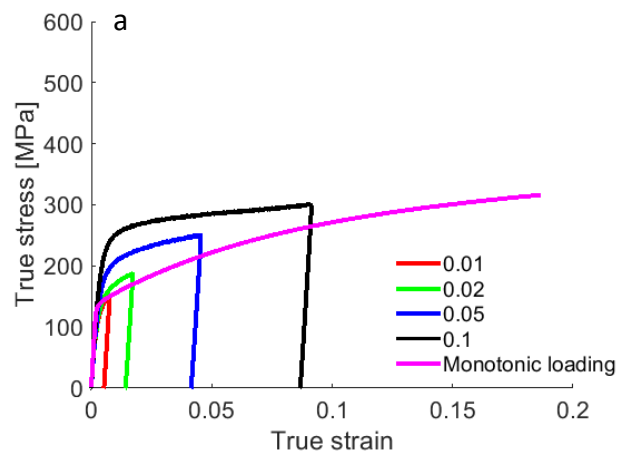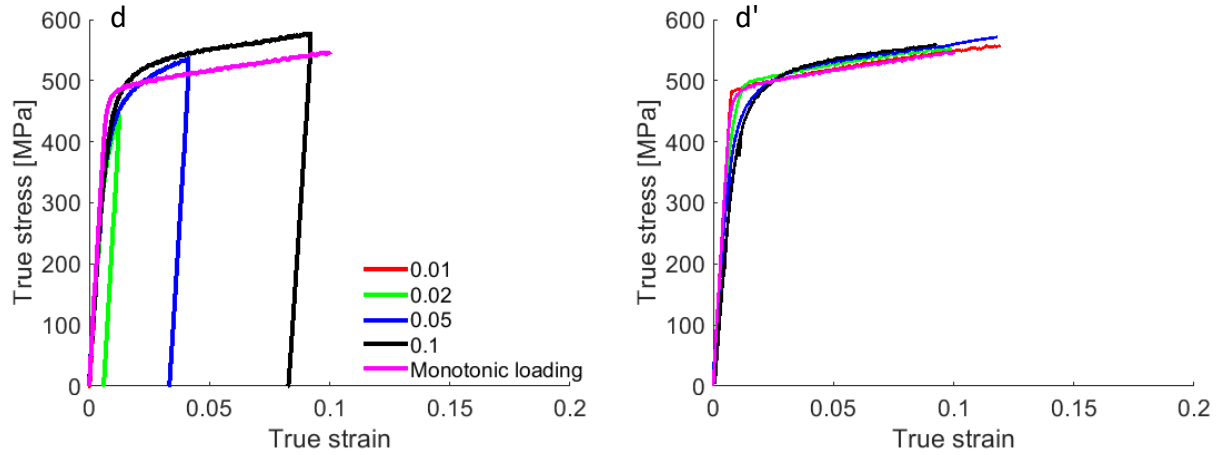
Figure 3. Comparison of the monotonic loading in tension curves vs. the 1st reversal (i.e. compression) curves from Fig. 2 for AA6016-T4 along (a) RD and (b) TD and for AA7021-T79 along (c) RD and (d) TD. Comparison of the monotonic tension curves vs. the 2nd reversal (i.e. tension) curves from Fig. 2 for AA6016-T4 along (a') RD and (b') TD and for AA7021-T79 along (c') RD and (d') TD. Legends in the 'unprimend' plots apply to the corresponding 'primed' plots.

4.2 Modeling

This section presents the results of model calibration and verification using the data. The uniaxial deformation processes are simulated by applying increments in strain along the loading direction (RD or TD), while enforcing the normal stresses in the lateral directions as well as the shear strains to zero. The simulations are initialized with the measured texture per alloy.

The hardening law along with the backstress law fitting parameters were adjusted using one cyclic tension-compression-tension curve per alloy, as each fitting parameter affects a different portion of the fitted curve. The curve deformed to a monotonic tensile pre-strain of 0.05 was used in fitting. The identified parameters were fine-tuned using another cyclic curve per alloy.

The remaining cyclic curves can be regarded as predictions. The parameters identified per alloy are the initial resistance to slip, τ_0^α, trapping rate coefficient, k_1^α, drag stress, D^α and activation barrier for de-pinning, g^α. The identification procedure started by varying τ_0^α to reproduce onset in yielding. Next, k_1^α, was varied such that the initial hardening slopes are captured. Next, g^α and D^α are varied to match the latter hardening rates. Finally, q^α was fit to capture the later stage in the hardening rates. Concurrently with the hardening parameters, the backstress law parameters were identified. These included the saturation value for backstress τ_{bs}^{sat}, asymmetry factor, A, and coefficients ν and γ_b. τ_{bs}^{sat} and A were varied to obtain the unloading and yield at load reversals. Once these were achieved, tuning ν and γ_b simply provides better fits. The established parameters per alloy are given in Table 2.

Fig. 4 shows the comparison of measured and simulated tension-compression-tension curves for the alloys. These multiple-range hysteresis curves are modeled with good accuracy. In particular, the model reproduced the features specific to the load reversal behavior of the alloys including the hardening rates, nonlinear unloading, BE, and permanent softening. Next, the monotonic tension and compression curves were simulated. Figure 5 shows the comparison for the monotonic data. The simulated curves are predictions. Importantly, the small anisotropy due to texture and underlying deformation mechanisms and their anisotropic hardening including the latent hardening is captured. AA6016-T4 does not exhibit any asymmetry, which is also well predicted by the model. Finally, the model is validated by simulating variable strain range and mean strain cycles for the alloys. The model was capable of capturing these complex data sets, also with good accuracy, as shown in Fig. 6. Although the model captures the yield point in the first cycle, re-yielding in the subsequent cycles is sometimes underpredicted in compression and overpredicted in tension. Model modifications such as accounting for spreads in the field

variables over ellipsoids could improve these predictions. In the present model, a single value is assumed for a given field across the entire ellipsoid. Such spreads have been incorporated in a visco-plastic SC (VPSC) formulation (Zecevic et al., 2017b).
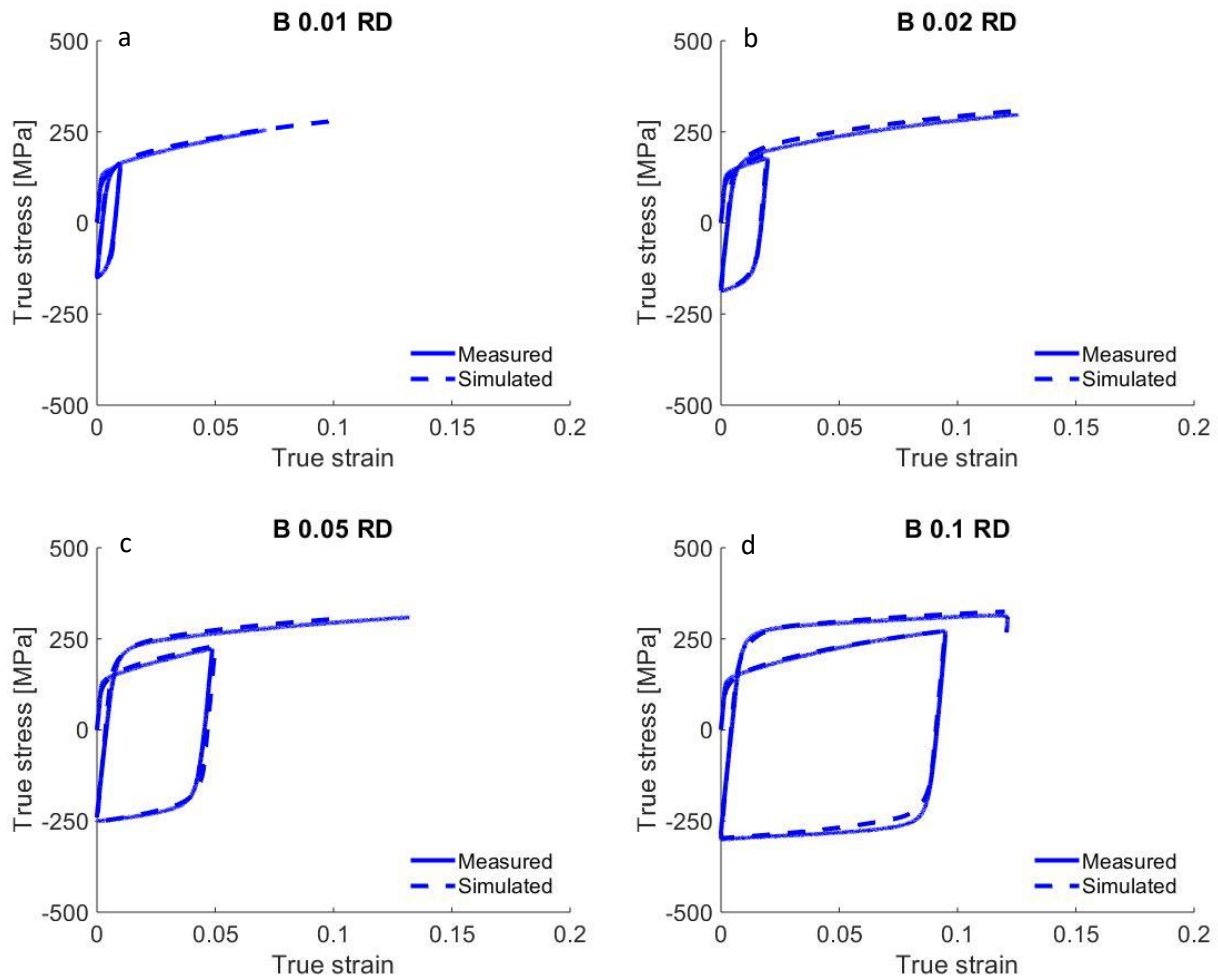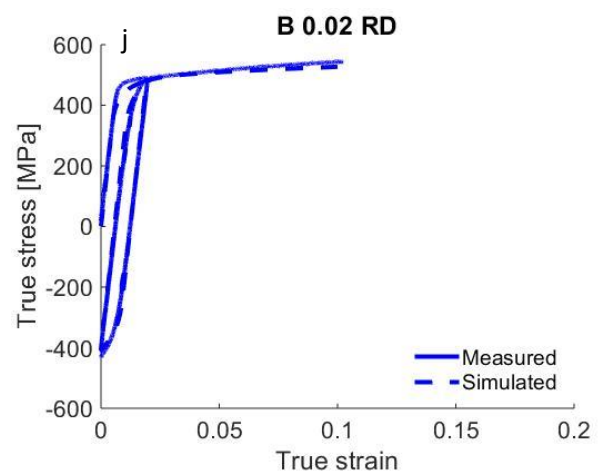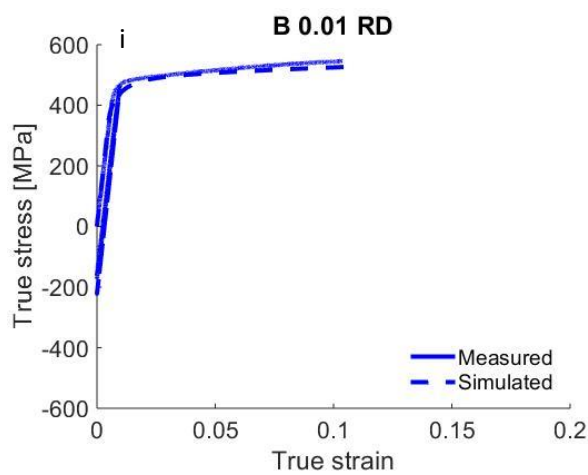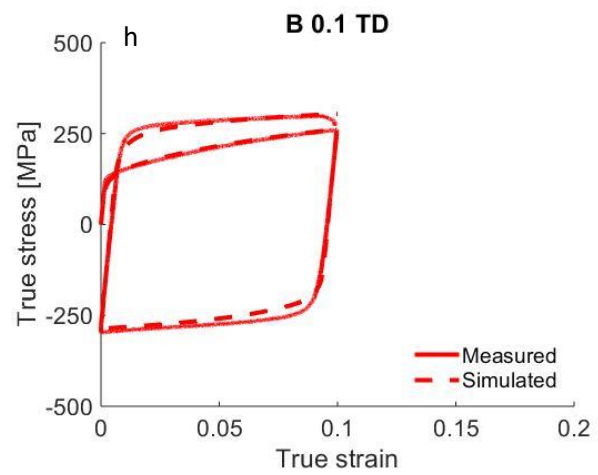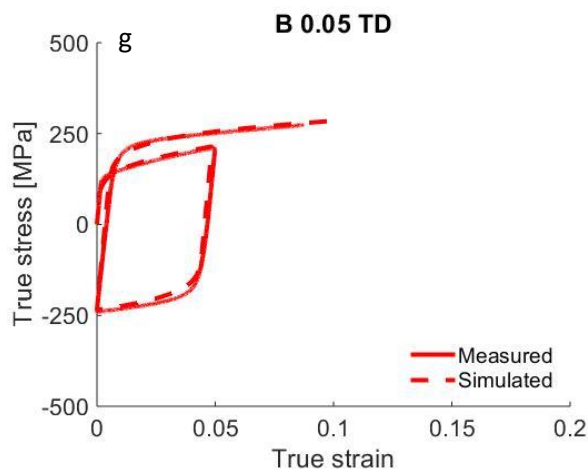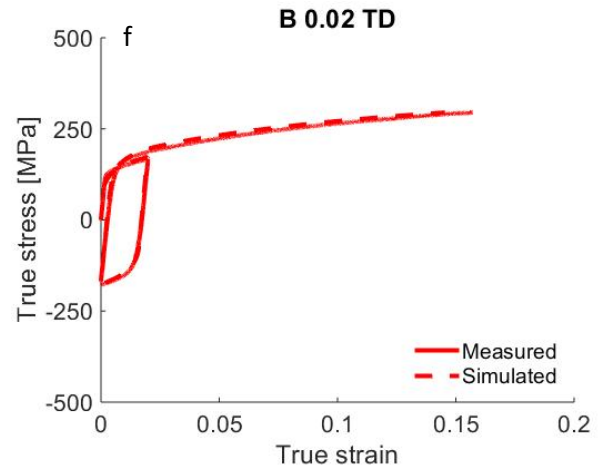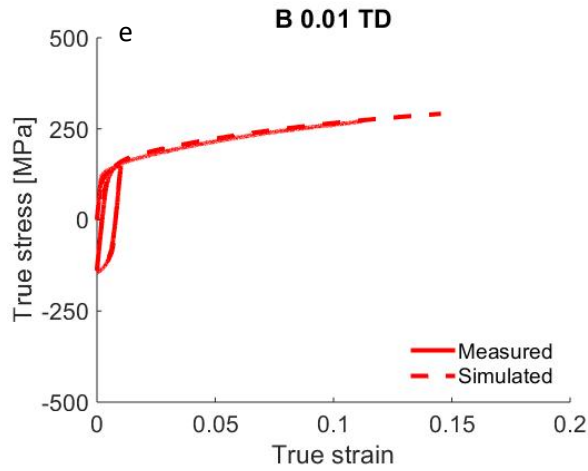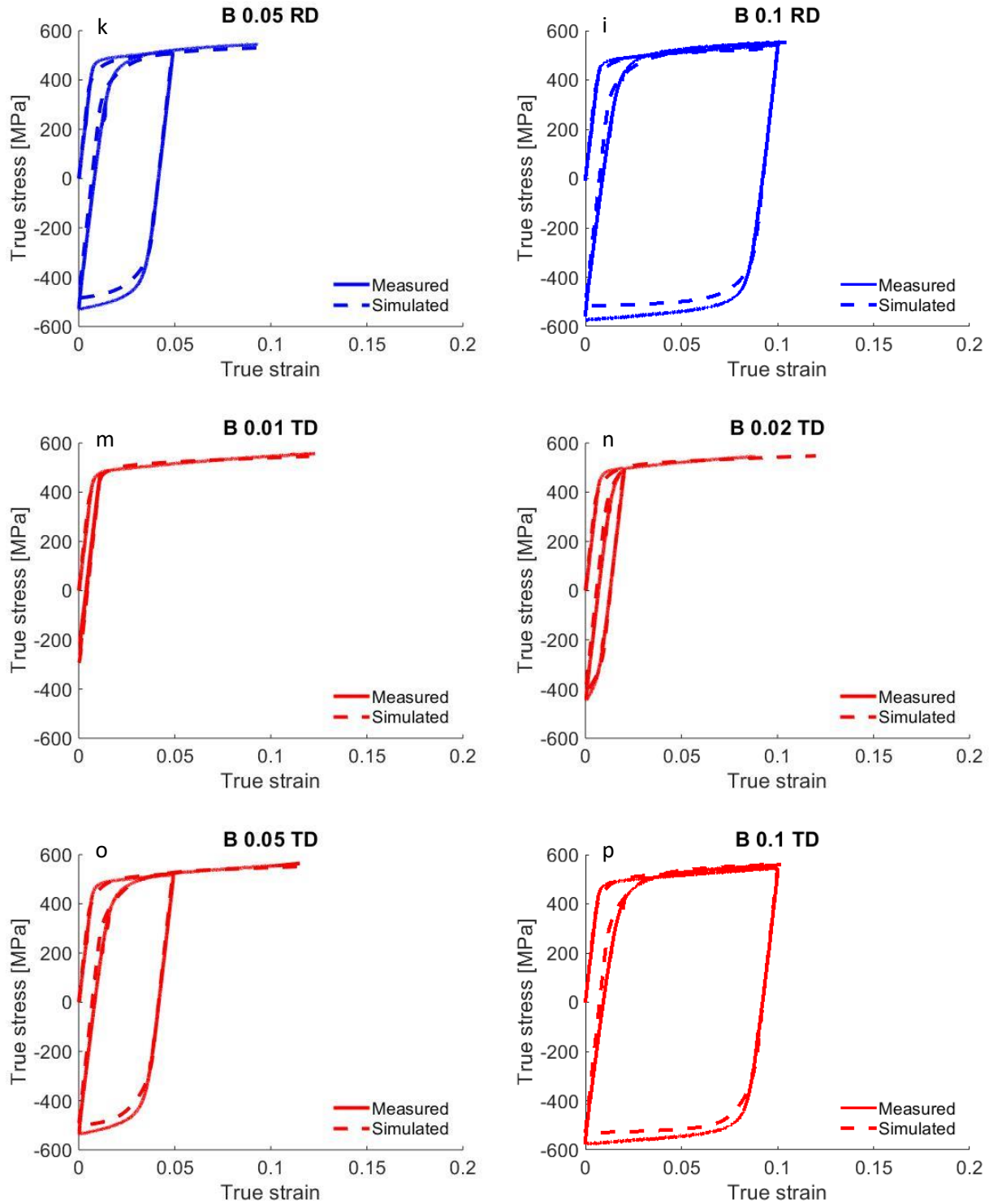
Figure 4. Comparison of simulated and measured true stress-true strain response in strain path reversal deformation for AA6016-T4 along (a - d) RD and (e - h) TD and for AA7021-T79 along (i - l) RD and (m – p) TD.

Table 2a. Fitting parameters for the evolution of slip resistance in AA6016-T4 and AA7021-T79.

	$\tau_0\,[\mathrm{MPa}]$	$k_1\,[m^{-1}]$	g	$D\,[\mathrm{MPa}]$	$\rho^s_{initial}\,[m^{-2}]$
AA6016-T4	28	1.38×10^{8}	0.09	400	4.9e12
AA7021-T79	85	1.00×10^{7}	0.09	400	1.5e14

Table 2b. Fitting parameters for the evolution of back-stress in AA6016-T4 and AA7021-T79.

$\tau^{sat}_{bs}\,[\mathrm{MPa}]$	v	γ_b	A
12	560	0.001	1

Table 2c. Latent hardening parameters established in (Devincre et al., 2006; Hoc et al., 2004) for FCC metals.

a_0	a_1	a_2	a_3	a_4	a_5
0.068	0.068	0.0454	0.625	0.137	0.122
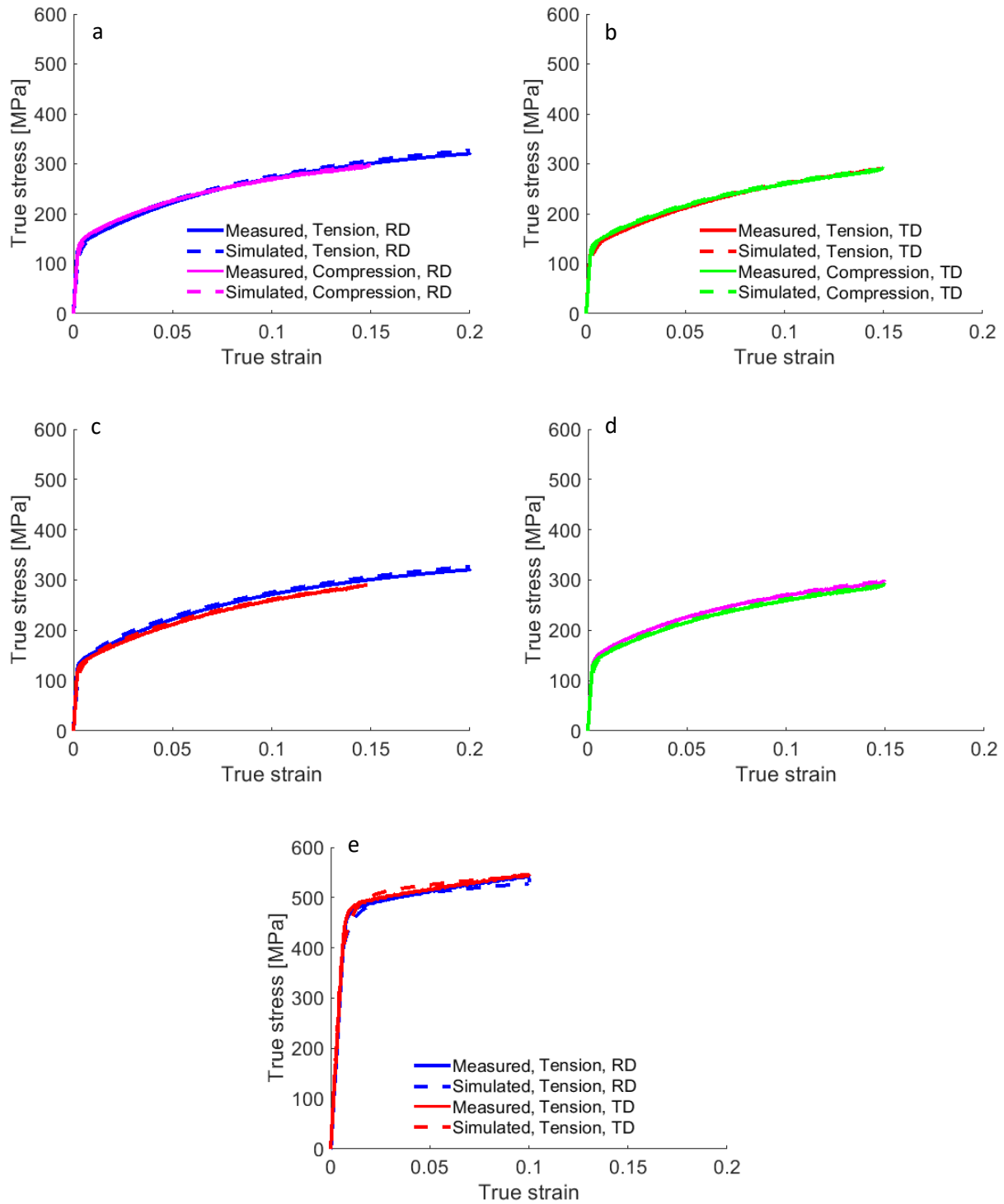
Figure 5. Comparison of predicted and measured true stress-true strain response in monotonic (a – d) simple tension and compression for AA6016-T4 and (e) simple tension for AA7021-T79.
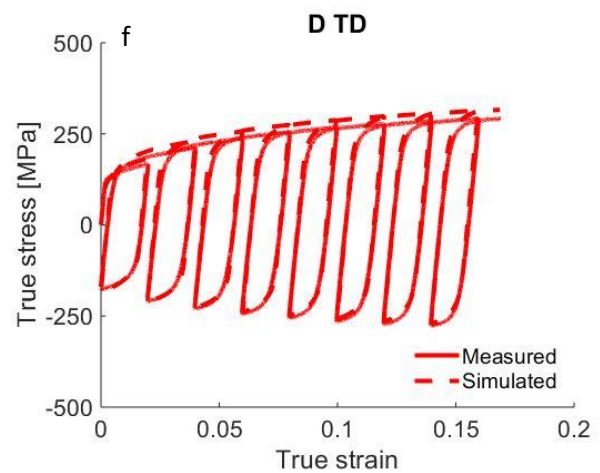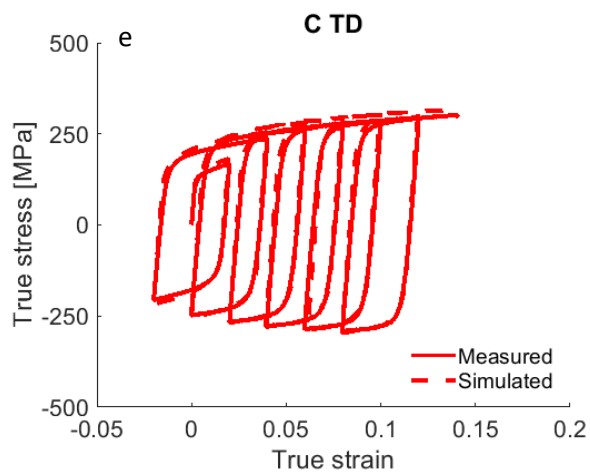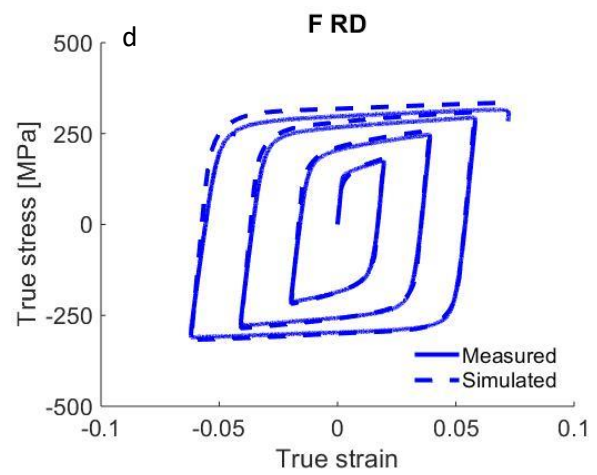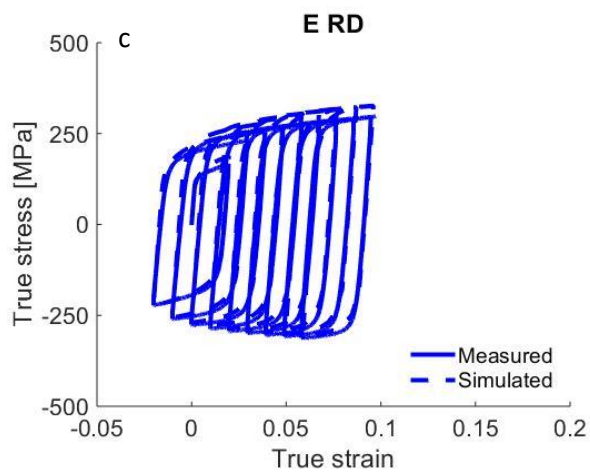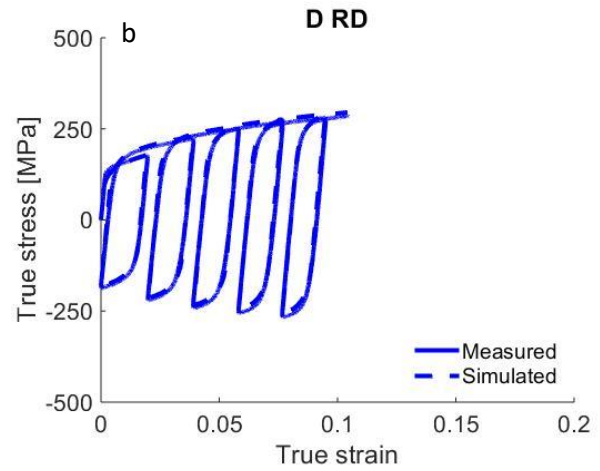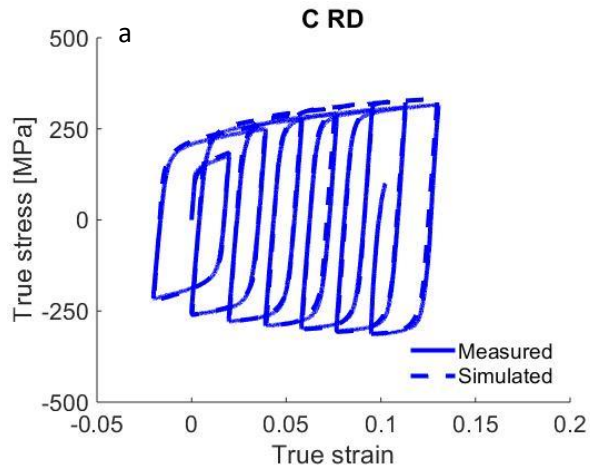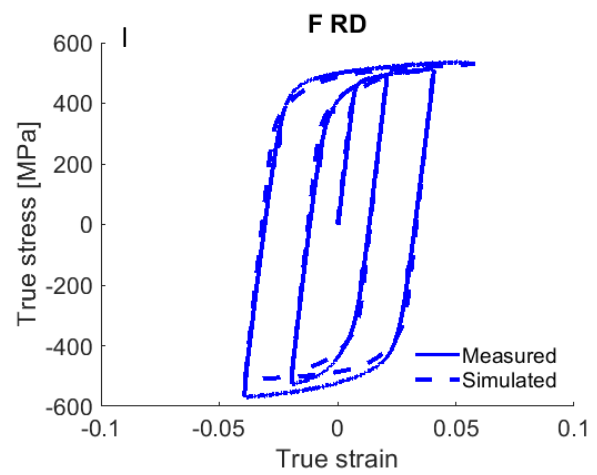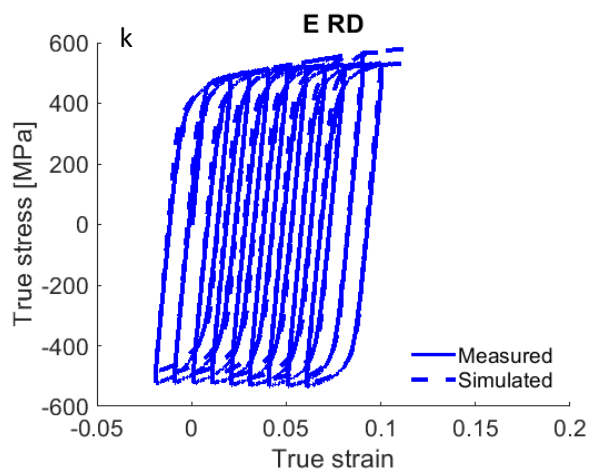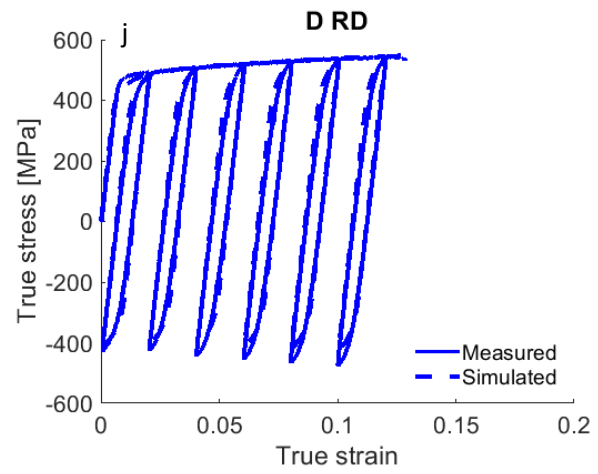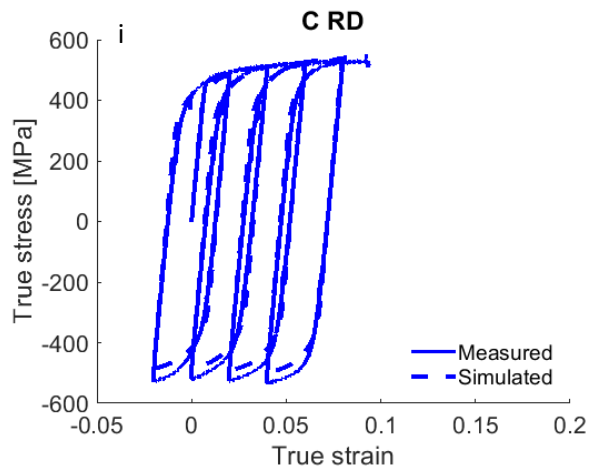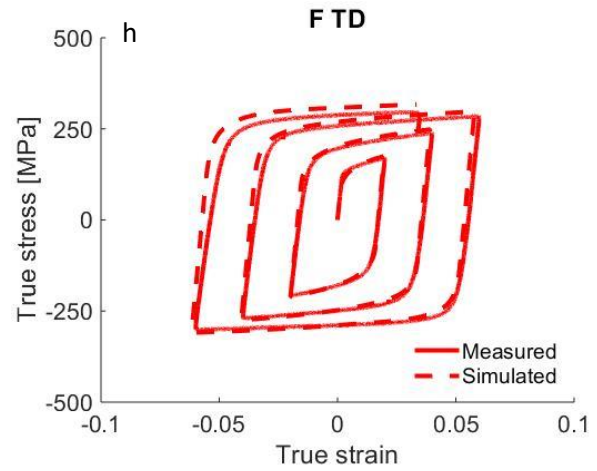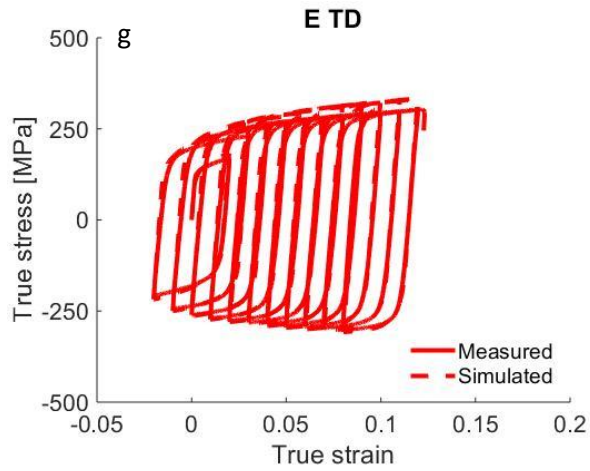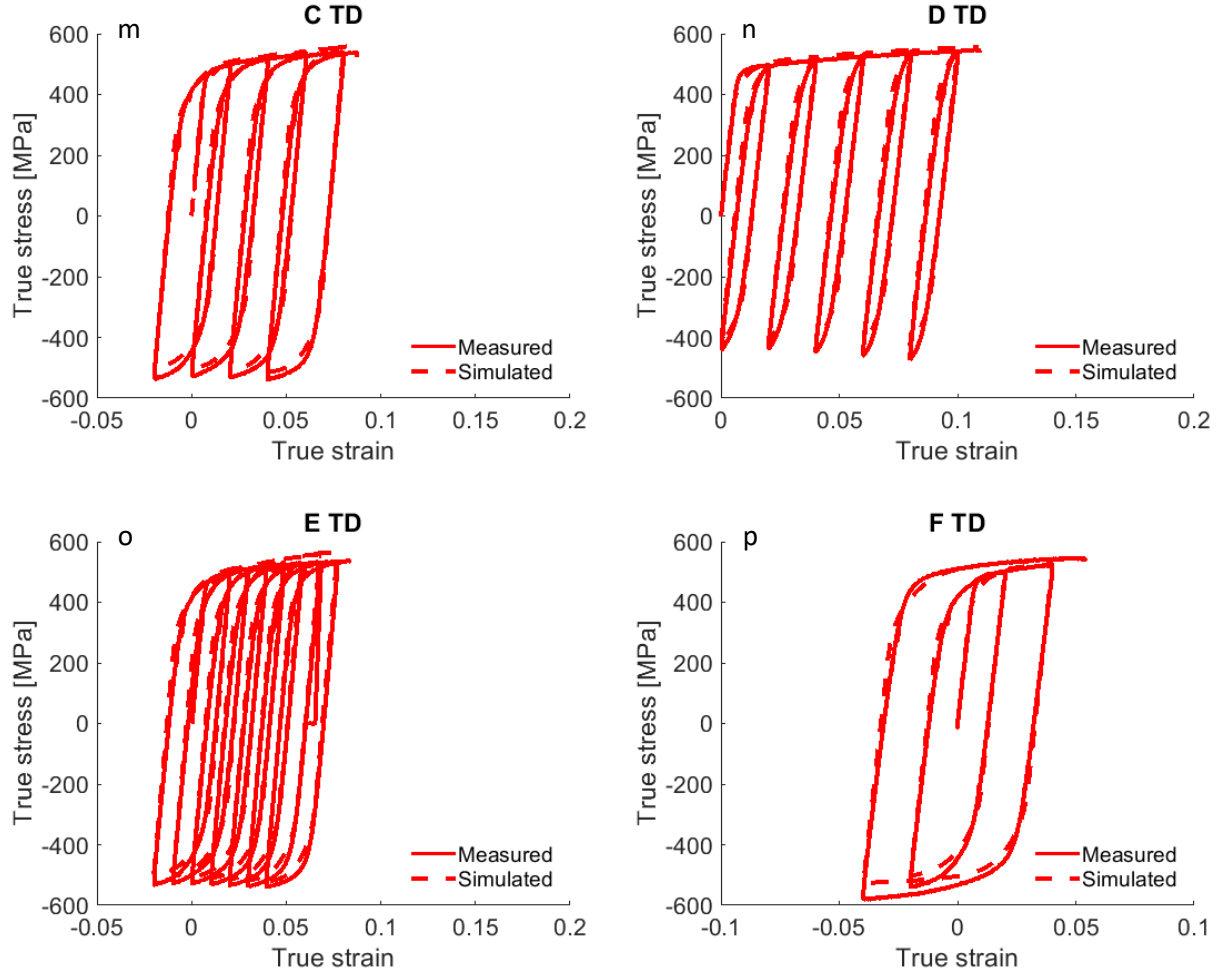
Figure 6. Comparison of predicted and measured true stress-true strain response during multiple strain cycles for AA6016-T4 along (a - d) RD and (e - h) TD anf for AA7021-T79 along (i - l) RD and (m – p) TD. The strain path in (a, e, i, and m) is: 0 → 0.02 → -0.02 → 0.04 → 0 → 0.06…up to fracture with the strain range/amplitude of 0.04 and mean strain increment of 0.02 per cycle. The strain path in (b, f, j, and n) is: 0 → 0.02 → 0 → 0.04 → 0.02 → 0.06…up to fracture with the strain range/amplitude of 0.02 and mean strain increment of 0.02 per cycle. The strain path in (c, g, k, and o) is: 0 → 0.02 → -0.02 → 0.03 → -0.01 → 0.04…up to fracture with the strain range/amplitude of 0.04 and mean strain increment of 0.01 per cycle. The strain path in (d, h, l, and p) is: 0 → 0.02 → -0.02 → 0.04 → -0.04 → 0.06…up to fracture.

5. Discussion

This work reports comprehensive monotonic and load reversal data for two Al alloys and is concerned with predicting and interpreting the data using crystal plasticity modeling, which captures microstructural evolution and the directionality of crystal-level deformation mechanisms. The model is the EPSC formulation (Zecevic and Knezevic, 2019), which incorporates a dislocation density-based hardening law originally developed in (Beyerlein and Tomé, 2008) and later advanced to account for dissolution of dislocations upon load reversal and slip system-level backstress fields.

The data showed typical decreasing hardening rates with minor anisotropy RD versus TD, a linear and then a nonlinear unloading, and the BE for both alloys. The data were employed to calibrate and validate the EPSC model. The performance of the model in capturing the complex deformation characteristics of the alloys is a consequence of accounting for kinematic hardening through the evolution law for backstress at the slip system-level, inter-granular stress fields, and annihilation to reproduce the stagnation or slight decrease in dislocation density upon strain-path reversal. Additionally, the model is initialized with the experimentally measured texture data and average grain shape for each grain per alloys. The aim is to provide physical insights into various aspects of the material response during strain-path reversals from the comparisons between data and predictions for both alloys.

To begin, we consider several additional parameters defined by looking at the overlap between the hysteresis loops and the monotonic tensile curves. The parameters are the reloading stress differential, $\Delta\sigma_h$, ratcheting strain, ϵ_Δ, and reloading softening stress, $\Delta\sigma_s$. Fig. 7a illustrates these additional parameters. Additionally, the unloading deviation stress $\Delta\sigma$ is also quantified. The reloading yield stress differential under tension i.e. the differential between

initial yield stress in tension and 2nd reversal yield stress is shown in Figs. 7b and c as a function of the applied tensile pre-strain. The differential increases with plastic strain for AA6016-T4, while it is nearly zero for AA7021-T79. Evidently, the increase in strength weakens the reloading yield effect, which is attributed to the difference in hardening rates i.e. primarily to a higher dislocation density (Table 2), and a slower buildup of dislocations with plastic strain in AA7021-T79 than AA6016-T4. Based on the data from Figs. 6a, b, e, f, i, j, m and n, the reloading softening stress is nearly zero for both alloys. As a result, the corresponding ratcheting strain is also negligibly small. These results are in contrast to recently reported results for dual phase steel sheets (Barrett and Knezevic, 2020). Finally, the unloading deviation stress is shown in Figs. 7d and e as a function of the applied pre-strain in tension. The deviation shows a decreasing trend with pre-strain, especially for the stronger alloy.

We regard the model as capable of predicting all of the phenomena associated with load reversal deformation of the alloys using a single set of parameters per alloy. The model predicts the cyclic behavior as a function of the loading direction and the level of pre-strain. With the model, we attempt to explain the deformation characteristics and underlying phenomena in the alloys during such deformation. Local stress in every grain is a consequence of the applied stress, inter-granular stress fields, and backstress fields. The model reveals that the backstress controls the nonlinear unloading deformation, early yielding upon reloading and immediate hardening that follows. Fig. 8 shows the buildup of backstress with the accumulated shearing strain in a randomly selected grain per alloys for a slip system with the highest activity in the chosen grain. In a study done on steels in (Wilson and Bate, 1986), backstress was estimated using an X-ray diffraction technique. Results of measurements showed that backstress increased rapidly to 0.03 strain. After the strain-path reversal, the backstress quickly decayed to zero by 0.02 reverse

strain. Our model predicts similar trends. Given that the unloading of both alloys is predicted using the same backstress parameters, the analysis shows that similar level of backstress fields develops in both alloys.

However, the backstress and intergranular stress fields are not sufficient to describe the flow stress upon strain-path reversals, as noted in (Orowan, 1948). Essentially, the reverse deformation would exhibit exactly the same shape of the flow curve as the original, just shifted along the stress axis. Subsequent deformation is controlled by the backstress and intergranular stress fields initially and then by the evolution of dislocation density. The annihilation of dislocation density upon strain-path reversal is an additional mechanism necessary for the accurate predictions of stress levels during strain-path reversal deformation. The effect is detected from a shrinkage in the diffraction peak widths upon strain-path reversal (Wilson and Bate, 1986). At the strain-path reversal, generation of dislocations is retarded momentarily because a fraction of loosely-tangled dislocations easily glides in the reverse direction (Beyerlein, 2008). Moreover, the stress relaxation takes place while the piled-up dislocations rearrange themselves into an equilibrium position with some annihilation of mobile dislocations.

Fig. 9 shows that the dislocation density evolution driven hardening rates are approximately 3x lower in AA7021-T79 than in AA6016-T4. The figure shows the volume average dislocation density evolution during the cyclic deformation for the alloys. Without the consideration of the reversible dislocations, the model would be able to predict the hardening rates after reversal. While the plots look similar for both alloys, substantially slower buildup of dislocation density is seen for AA7021-T79. Interestingly, some deformation can be accommodated without a marked increase in dislocation density. These predicted trends are in good agreement with the constitutive assumptions invoked in developing cyclic plasticity models in (Ohno, 1982; Ohno

and Kachi, 1986). The easy motion and annihilation of reversible dislocations in the opposite direction is controlled by the reversibility parameter. The effect of local reversible dislocation population for the reversibility parameter of 0.2 is shown in Fig. 10 for a grain in both alloys. Such evolution is typical for all grains with the accumulated shear strain on a slip system mediating the issue of over-predicting of the hardening upon the strain-path reversal. As result, the evolution of slip resistance is directional at the slip system level and evolves with these microstructure rearrangements upon load reversal. Fig. 9 is a collective result for total dislocation density of all grains per alloy. The evolution of dislocation density is responsible for predicting the magnitude of permanent softening per alloy. The phenomenon was first described in (Hasegawa et al., 1975b) during tension-compression loading. It was also described for forward-reverse simple shear loading in (Gracio et al., 2004).

Good predictions of the strain-path reversal deformation behavior of the alloys is a collective result of several distinct physical phenomena incorporated in the model. The evolution of inter-granular stress fields is the remaining phenomena the model accounts for. In general, the backstress fields have intra-granular and inter-granular sources in polycrystals. Inter-granular sources are the interactions between individual grains of different crystal orientations. As already mentioned, these effects are approximated in the EPSC formulation because every grain interacts with the averaged polycrystalline response unlike in full-field models in which grain-to-grain interaction are explicitly modeled. At zero applied stress, these inter-granular stress fields become residual stress fields. Fig. 11 shows the role of residual stress in the predictions. To obtain the predictions without residual stress, grain stress is set to zero at the zero overall flow stress after the 1st and 2nd reversals. The response after the 1st reversal is controlled by the slip resistance at the end of monotonic tension pre-straining and backstress. Evidently, the inter-

granular stresses govern the BE and yield differentials along with the backstresses but do not play a significant role for the nonlinear unloading. These results agree with arguments presented in (Kassner et al., 2009) that solely intra-granular backstress-based theories do not completely describe the BE. From the comparison of the curves with and without inter-granular stresses, it is evident that the inter-granular stresses are aiding plastic deformation in the reverse direction (i.e. the compression). Subsequently, the model predicts a decrease in yield stress in tension. The difference is ~40 MPa for both alloys compared to that at the end of the first tension. Similar effects of inter-granular stresses on the cyclic deformation were reported in (Li et al., 2014; Wu et al., 2005).
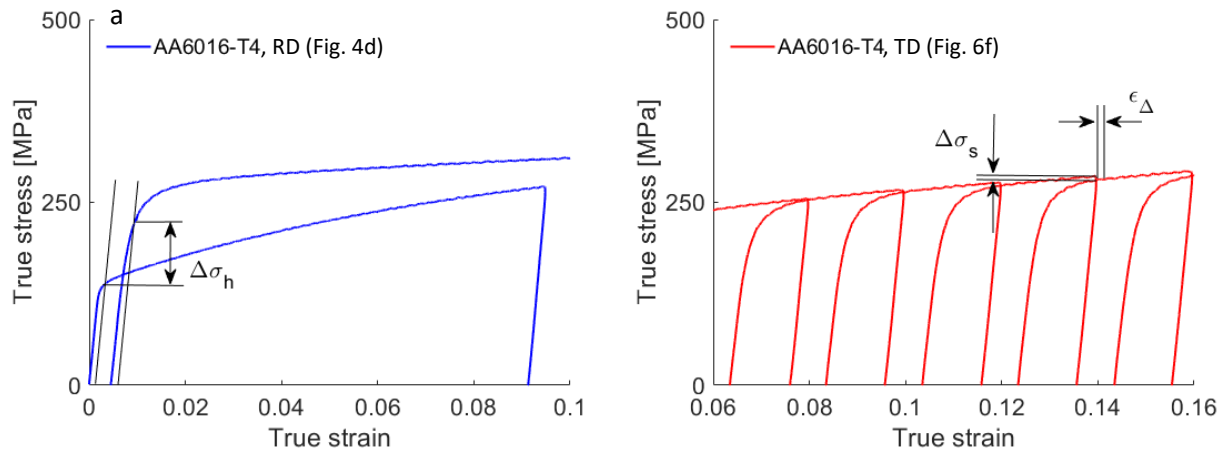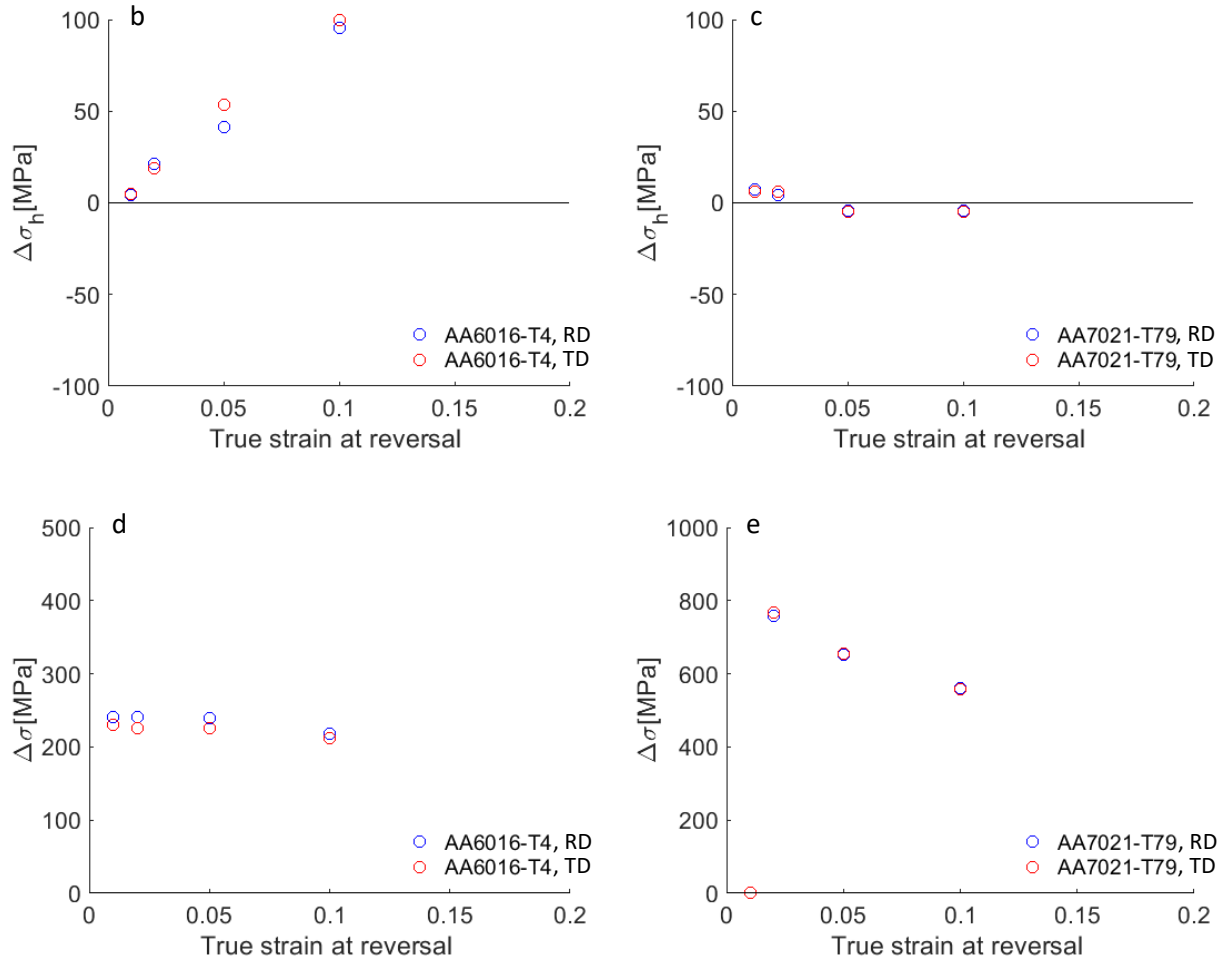
Figure 7. (a) Schematics defining the reloading yield stress differential under tension ($\Delta\sigma_h$), ratcheting strain (ϵ_Δ), and reloading softening stress ($\Delta\sigma_s$). Comparison of $\Delta\sigma_h$ versus true strain levels for 1st reversal for (b) AA6016-T4 and (c) AA7021-T79. Unloading deviation stress ($\Delta\sigma = \sigma_L - \sigma_U$), where σ_L is the true stress at the end of a pre-load and σ_U is the macro-yield stress during unload at approximately 0.001 offset, for (d) AA6016-T4 and (e) AA7021-T79.
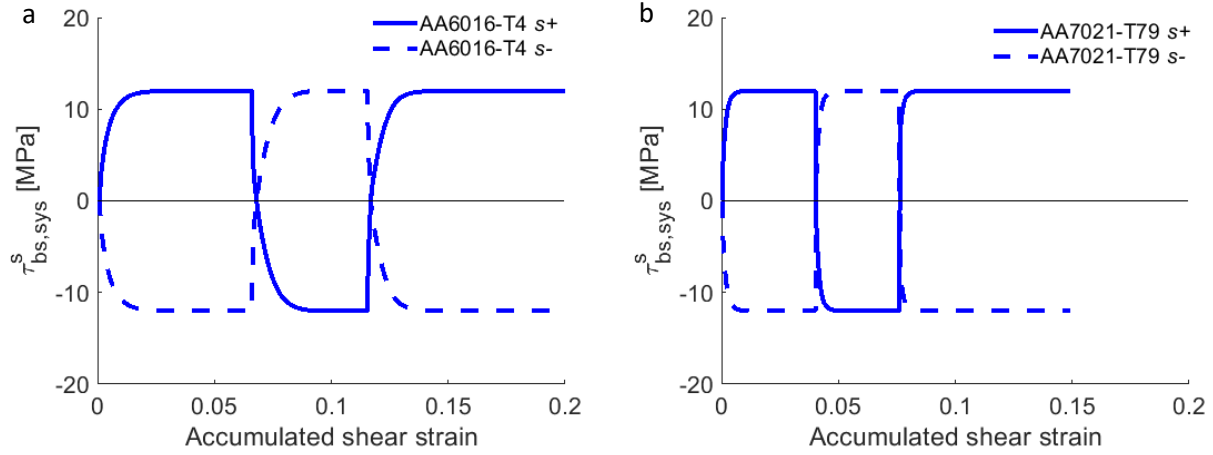
Figure 8. Backstress vs. accumulated shear strain for an sth slip system with the highest activity in a randomly selected grain during forward tension to 0.05 strain followed by the 1st and the 2nd reversal along RD for (a) AA6016-T4 and (b) AA7021-T79.
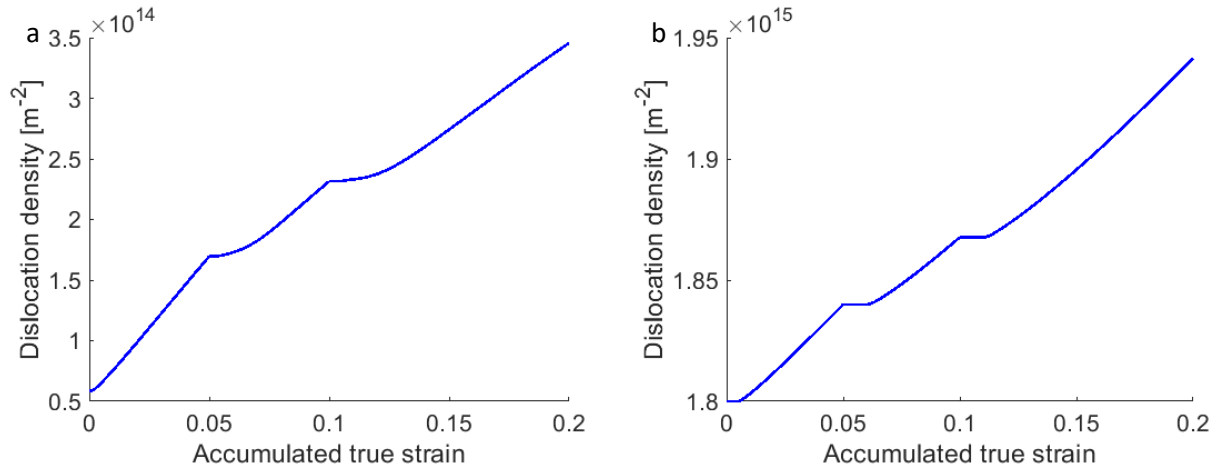
Figure 9. Evolution of total dislocation density ($\sum_s \rho_{tot}^s$) during forward tension to 0.05 strain followed by the 1st and the 2nd reversal for (a) AA6016-T4 deformed along RD and in (b) AA7021-T79 deformed along RD.
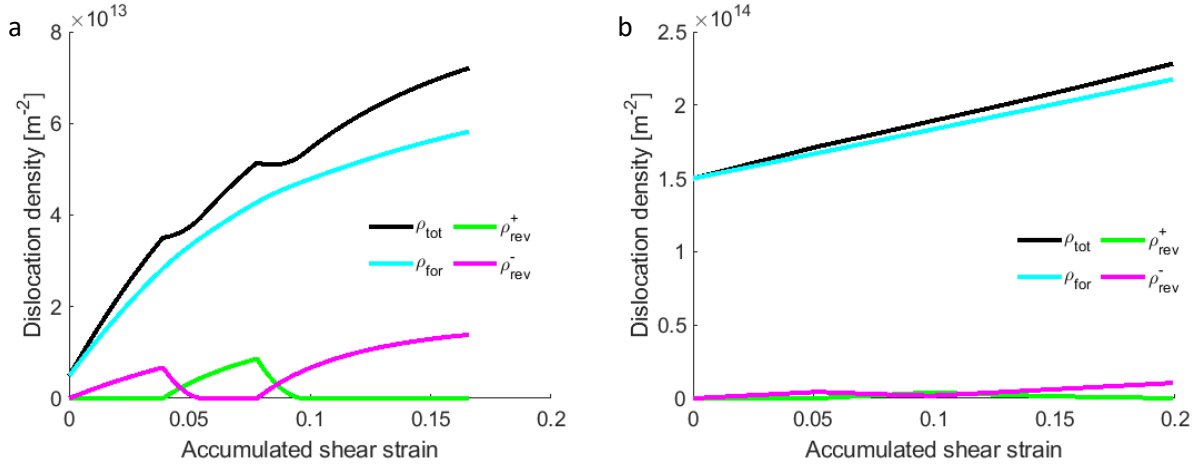
Figure 10. Evolution of dislocation populations with the accumulated shear for a slip system with the highest activity in a randomly selected grain during forward tension to 0.05 strain followed by the 1st and the 2nd reversal along RD for (c) AA6016-T4 and (d) AA7021-T79.
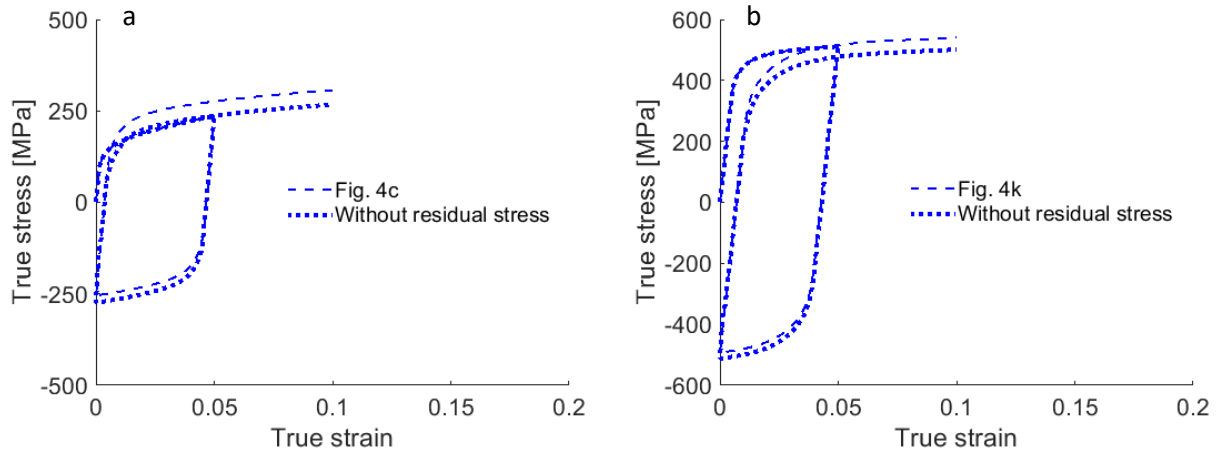
Figure 11. Comparison of true stress–true strain response simulated with and without residual stress during forward tension to 0.05 strain followed by the 1st and the 2nd reversal along RD for (a) AA6016-T4 and (b) AA7021-T79.

6. Conclusions

The monotonic and large strain cyclic response of AA6016-T4 and AA7021-T79 sheets was measured along the rolling and transverse directions. The data for both alloys showed the typical decreasing hardening rates during monotonic tension cycles. Upon the 1st strain path reversal, the extent of the nonlinear unloading was greater for AA7021-T79 than for AA6016-T4. The magnitude of macro-yield stress increased with the pre-strain level in monotonic tension for both alloys. As a result, the unloading deviation stress decreased, especially for the stronger AA7021-T79. The nonlinear unloading caused a prolonged elasto-plastic transition to re-yielding. The BE was evident in both alloys and increased with pre-strain and strength. Upon re-yielding, the rates of strain hardening were quickly restored. Interestingly, the strain hardening in compression was sufficient to increase to that of monotonic tension for AA7021-T79 but insufficient for AA6016-T4. As a result, AA6016-T4 exhibited a permanent softening phenomenon. Upon the 2nd strain path reversal, the hysteresis loops closed for AA7021-T79 but not for AA6016-T4. Consequently, the reloading yield stress differential under tension arose and increased with the level of pre-strain for AA6016-T4 but not for AA7021-T79. The multiple forward-reversal cyclic curves showed that the reloading softening stress and resulting ratcheting strain were small for both alloys.

The true stress-true strain data were used to calibrate and then critically validate the EPSC crystal plasticity model, which features sub-models including anisotropic elasticity, a strain-path sensitive law for the evolution of dislocation density, and a backstress law at the slip system-level. The model reproduced the response of both alloys during monotonic and cyclic deformation to various levels of plastic pre-strains with good accuracy using a single set of parameters per alloy. Such good performances of the model were primarily a consequence of

accounting for kinematic hardening at the slip system-level through the evolution law for backstress, inter-granular stresses, and dislocation annihilation reflecting the experimentally observed stagnation in the dislocation density build up upon strain reversals. Comparison of the experimental and modeling results revealed that the unloading behavior is primarily driven by backstress, the BE is governed by backstress and inter-granular stresses, and the hardening rates upon load reversals are controlled primarily by the strain-path sensitive evolution of dislocation density. Significantly, the model predicted the contrasting characteristics in the hysteresis of the alloys, such as the presence of large permanent softening and reloading yield stress differential in AA6016-T4 as compared to AA7021-T79. Given that the EPSC model has been coupled with the FEM to treat complex, non-monotonic deformation conditions in prior works, future works will focus on various metal forming simulations taking advantage of the EPSC adjusted here to capture the cyclic plasticity phenomena as these have essential implications on the accuracy of metal forming simulations, especially in accurate prediction of springback. As many of these features that were observed in the flow stresses of AA6016-T4 and AA7021-T79 are similar to those in other cubic alloys, the present model is expected to be applicable to a wider set of alloys in addition to Al alloys.

Appendix

This appendix presents geometry of the specimen used for the load reversal testing (Fig. A1) (Noma and Kuwabara, 2012) and inverse pole figure (IPF) maps showing grain structure in the alloys (Fig. A2).
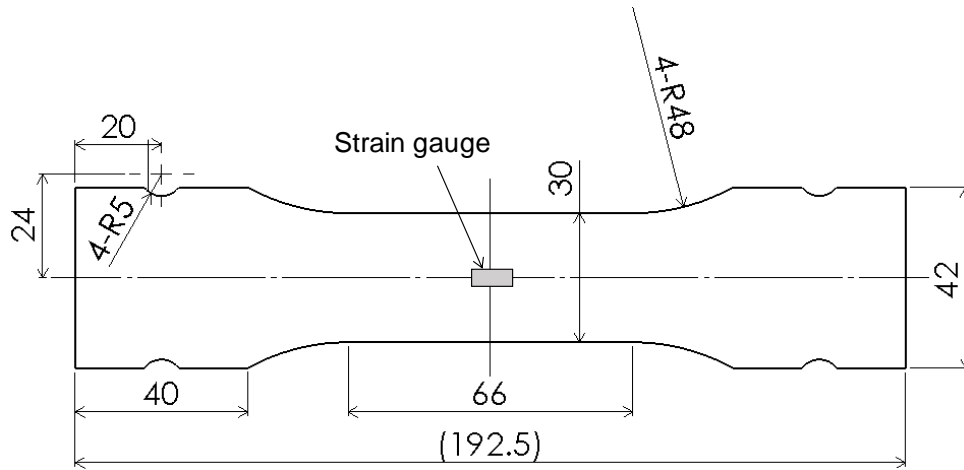

Figure A1. Geometry of the specimen used in the tension-compression testing. Units in mm.
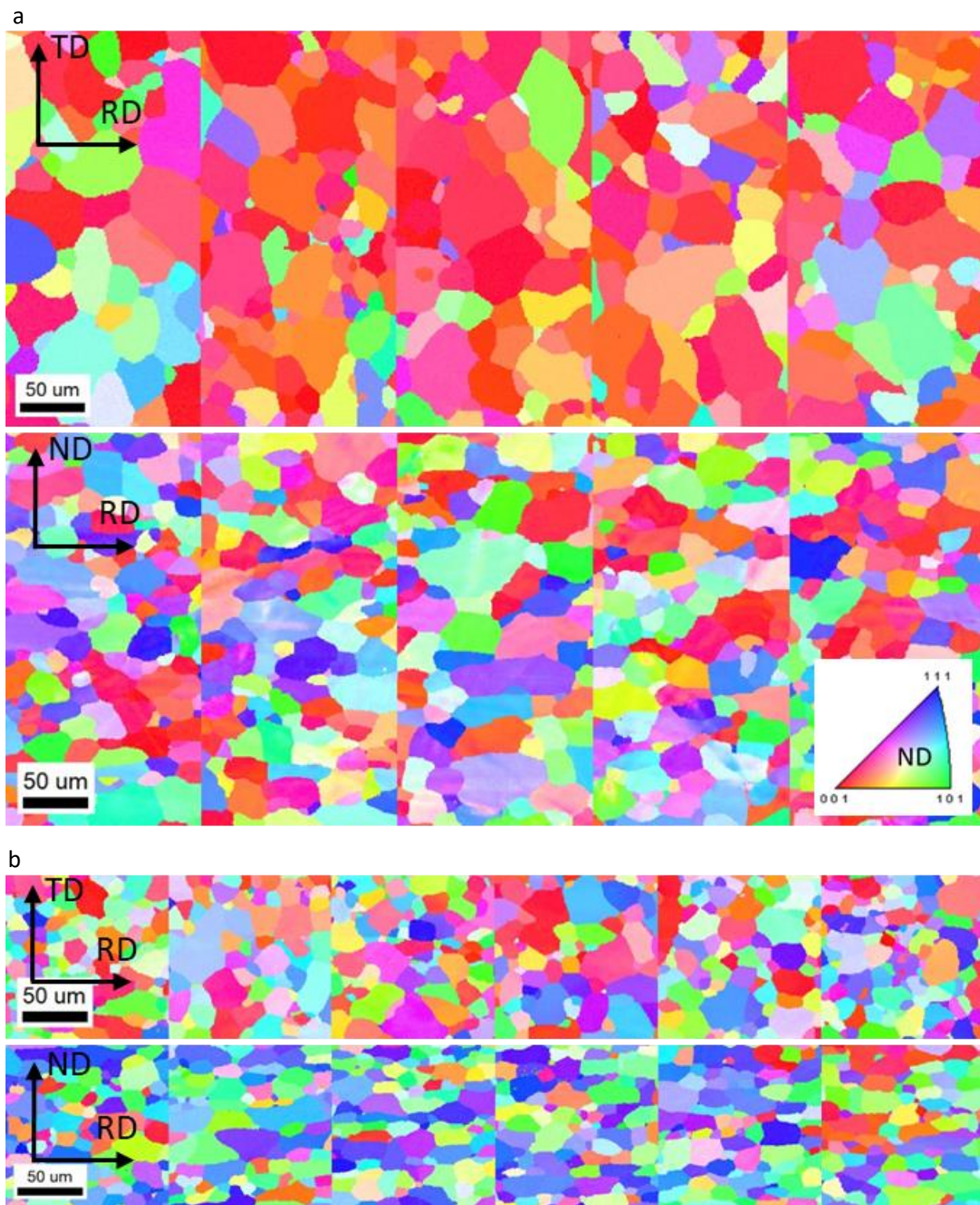
Figure A2. IPF orientation maps for (a) AA6016-T4 and (b) AA7021-T79. Note that several

different regions of virgin samples are scanned. The standard IPF triangle defines colors for the

sample axis ND. Horizontal and vertical axes of the maps are indicated in the maps. Based on the

maps, average grain size is 32 µm in RD, 30 µm in TD, and 18 µm in ND for AA6016-T4 and 18

µm in RD, 14 µm in ND, and 9 µm in ND for AA7021-T79.

References

Abel, A., 1987. Historical perspectives and some of the main features of the Bauschinger effect, Materials Forum. Institute of Metals and Materials Australasia, pp. 11-26.

Anjabin, N., Karimi Taheri, A., Kim, H.S., 2014. Crystal plasticity modeling of the effect of precipitate states on the work hardening and plastic anisotropy in an Al–Mg–Si alloy. Comput. Mater. Sci. 83, 78-85.

Armstrong, P.J., Frederick, C.O., 1966. A mathematical representation of multiaxial Bauschinger effect. Berkeley nuclear laboratories.

Barlat, F., Ferreira Duarte, J., Gracio, J., Lopes, A., Rauch, E., 2003. Plastic flow for non-monotonic loading conditions of an aluminum alloy sheet sample. Int. J. Plast. 19, 1215-1244.

Barrett, T.J., Knezevic, M., 2019. Deep drawing simulations using the finite element method embedding a multi-level crystal plasticity constitutive law: Experimental verification and sensitivity analysis. Computer Methods in Applied Mechanics and Engineering 354, 245-270.

Barrett, T.J., Knezevic, M., 2020. Modeling material behavior during continuous bending under tension for inferring the post-necking strain hardening response of ductile sheet metals: Application to DP 780 steel. International Journal of Mechanical Sciences 174, 105508.

Barrett, T.J., McCabe, R.J., Brown, D.W., Clausen, B., Vogel, S.C., Knezevic, M., 2020. Predicting deformation behavior of α-uranium during tension, compression, load reversal, rolling, and sheet forming using elasto-plastic, multi-level crystal plasticity coupled with finite elements. J. Mech. Phys. Solids 138, 103924.

Bate, P., Roberts, W., Wilson, D., 1981. The plastic anisotropy of two-phase aluminium alloys—I. Anisotropy in unidirectional deformation. Acta Metall. 29, 1797-1814.

Bate, P., Roberts, W., Wilson, D., 1982. The plastic anisotropy of two-phase aluminium alloys—II. anisotropic behaviour in load-reversal tests. Acta Metall. 30, 725-737.

Bate, P., Wilson, D., 1986a. Analysis of the Bauschinger effect. Acta Metall. 34, 1097-1105.

Bate, P.S., Wilson, D.V., 1986b. Analysis of the bauschinger effect. Acta Metallurgica 34, 1097-1105.

Bauschinger, J., 1886. Über die Veränderung der Elasticitätsgrenze und Festigkeit des Eisen und Stahls durch Strecken und Quetschen, durch Erwarmen und Abkühlen und durch oftmal wiederholte Beanspruchung. Mitteilungen aus dem mechanisch-technischen Laboratorium der k. polytechnischen Schule, 1877-1836.

Beyerlein, I.J., 2008. Plastic Behavior of Metals in Reverse Straining after Large Pre-Strains. Materials Science Forum 579, 41-60.

Beyerlein, I.J., Tomé, C.N., 2008. A dislocation-based constitutive law for pure Zr including temperature effects. Int. J. Plast. 24, 867-895.

Bhattacharyya, J.J., Bittmann, B., Agnew, S.R., 2018. The effect of precipitate-induced backstresses on plastic anisotropy:

Demonstrated by modeling the behavior of aluminum alloy 7085. Int J Plasticity in press.

Boger, R., Wagoner, R., Barlat, F., Lee, M., Chung, K., 2005. Continuous, large strain, tension/compression testing of sheet material. Int. J. Plast. 21, 2319-2343.

Brown, G.M., 1970. Inelastic deformation of an aluminum alloy under combined stress at elevated temperature. J. Mech. Phys. Solids 18, 383-396.

Brown, L.M., Clarke, D.R., 1975. Work hardening due to internal stresses in composite materials. Acta Metallurgica 23, 821-830.

Buckley, S.N., Entwistle, K.M., 1956. The bauschinger effect in super-pure aluminum single crystals and polycrystals. Acta Metall. 4, 352-361.

Chaboche, J., Rousselier, G., 1983. On the plastic and viscoplastic constitutive equations—Part I: Rules developed with internal variable concept. Journal of Pressure Vessel Technology 105, 153-158.

Chaboche, J.L., 1977. Viscoplastic constitutive equations for the description of cyclic and ansiotropic behavior of metals, In: XVIIth Polish solid mechanics conference, Bulletin de l'Académie Polonaise des Sciences, Série Sciences et Techniques, pp. 33-41.

Chaboche, J.L., 2008. A review of some plasticity and viscoplasticity constitutive theories. Int. J. Plast. 24, 1642-1693.

Chen, Z., Maekawa, S., Takeda, T., 1999. Bauschinger effect and multiaxial yield behavior of stress-reversed mild steel. Metall. Mater. Trans. A 30, 3069-3078.

Chun, B.K., Jinn, J.T., Lee, J.K., 2002. Modeling the Bauschinger effect for sheet metals, part I: theory. Int. J. Plast. 18, 571-595.

Couturier, L., Deschamps, A., De Geuser, F., Fazeli, F., Poole, W.J., 2017. An investigation of the strain dependence of dynamic precipitation in an Al-Zn-Mg-Cu alloy. Scr. Mater. 136, 120-123.

Demir, E., Raabe, D., 2010. Mechanical and microstructural single-crystal Bauschinger effects: Observation of reversible plasticity in copper during bending. Acta. Mater. 58, 6055-6063.

Devincre, B., Kubin, L., Hoc, T., 2006. Physical analyses of crystal plasticity by DD simulations. Scr. Mater. 54, 741-746.

Dietrich, L., Turski, K., 1978. New method of sheet metal compression tests. Rozp. Inz. 26.

Eshelby, J.D., 1957. The determination of the elastic field of an ellipsoidal inclusion, and related problems. Proc R. Soc. Lond. A 241, 376-396.

Eskin, D.G., Kharakterova, M.L., 2001. The effect of silicon and copper on the precipitation hardnening of sheets of 6xxx series alloy. Mater. Technol. 35, 5-8.

Feng, Z., Yoon, S.-Y., Choi, J.-H., Barrett, T.J., Zecevic, M., Barlat, F., Knezevic, M., 2020. A comparative study between elasto-plastic self-consistent crystal plasticity and anisotropic yield function with distortional hardening formulations for sheet metal forming. Mechanics of Materials 148, 103422.

Gough, H., Hanson, D., Wright, S., 1927. The Behaviour of Single Crystals of Aluminium under Static and Repeated Stresses. Philosophical Transactions of the Royal Society of London. Series A, Containing Papers of a Mathematical or Physical Character, 1-30.

Gracio, J.J., Barlat, F., Rauch, E.F., Jones, P.T., Neto, V.F., Lopes, A.B., 2004. Artificial aging and shear deformation behaviour of 6022 aluminium alloy. Int. J. Plast. 20, 427-445.

Greetham, G., Honeycombe, R., 1960. The deformation of single crystals of aluminum 4.5-percent copper alloy. Journal of the Institute of Metals 89, 13-21.

Hasegawa, T., Yakou, T., Karashima, S., 1975a. Deformation behaviour and dislocation structures upon stress reversal in polycrystalline aluminium. Materials Science and Engineering 20, 267-276.

Hasegawa, T., Yakou, T., Karashima, S., 1975b. Deformation behaviour and dislocation structures upon stress reversal in polycrystalline aluminium. Materials Science and Engineering 20, 267-276.

Hoc, T., Devincre, B., Kubin, L., 2004. Deformation stage I of FCC crystals: Constitutive modelling, 25 th Riso International Symposium on Materials Science 2004, pp. 43-59.

Hu, Z., Rauch, E.F., Teodosiu, C., 1992. Work-hardening behavior of mild steel under stress reversal at large strains. Int. J. Plast. 8, 839-856.

Jaafar, A., Rahmat, A., Zainol, l., Hussain, Z., 2012. Effects of Composition on the Mechanical Properties and Microstructural Development of Dilute 6000 Series Alloys. Journal of Applied Science 12, 775-780.

Kalidindi, S.R., Bronkhorst, C.A., Anand, L., 1992. Crystallographic texture evolution in bulk deformation processing of FCC metals. J. Mech. Phys. Solids 40, 537-569.

Kalidindi, S.R., Duvvuru, H.K., Knezevic, M., 2006. Spectral calibration of crystal plasticity models. Acta. Mater. 54, 1795-1804.

Kassner, M.E., Geantil, P., Levine, L.E., 2013. Long range internal stresses in single-phase crystalline materials. International Journal of Plasticity 45, 44-60.

Khadyko, M., Dumoulin, S., Cailletaud, G., Hopperstad, O.S., 2016. Latent hardening and plastic anisotropy evolution in AA6060 aluminium alloy. Int. J. Plast. 76, 51-74.

Kitayama, K., Tomé, C.N., Rauch, E.F., Gracio, J.J., Barlat, F., 2013a. A crystallographic dislocation model for describing hardening of polycrystals during strain path changes. Application to low carbon steels. International Journal of Plasticity 46, 54-69.

Kitayama, K., Tomé, C.N., Rauch, E.F., Gracio, J.J., Barlat, F., 2013b. A crystallographic dislocation model for describing hardening of polycrystals during strain path changes. Application to low carbon steels. International Journal of Plasticity in press.

Knezevic, M., Kalidindi, S.R., Fullwood, D., 2008. Computationally efficient database and spectral interpolation for fully plastic Taylor-type crystal plasticity calculations of face-centered cubic polycrystals. Int. J. Plast. 24, 1264-1276.

Knezevic, M., McCabe, R.J., Lebensohn, R.A., Tomé, C.N., Liu, C., Lovato, M.L., Mihaila, B., 2013. Integration of self-consistent polycrystal plasticity with dislocation density based hardening laws within an implicit finite element framework: Application to low-symmetry metals. J. Mech. Phys. Solids 61, 2034-2046.

Knezevic, M., Poulin, C.M., Zheng, X., Zheng, S., Beyerlein, I.J., 2019. Strengthening of alloy AA6022-T4 by continuous bending under tension. Mater. Sci. Eng. A 758, 47-55.

Knockaert, R., Chastel, Y., Massoni, E., 2000. Rate-independent crystalline and polycrystalline plasticity, application to FCC materials. International Journal of Plasticity 16, 179-198.

Kocks, U.F., Franciosi, P., Kawai, M., 1991. A Forest Model of Latent Hardening and its Application to Polycrystal Deformations. Textures and Microstructures 14, 1103-1114.

Kuwabara, T., Kumano, Y., Ziegelheim, J., Kurosaki, I., 2009. Tension–compression asymmetry of phosphor bronze for electronic parts and its effect on bending behavior. Int. J. Plast. 25, 1759-1776.

Kuwabara, T., Nagata, K., Nakako, T., 2001. Measurement and analysis of the Bauschinger effect of sheet metals subjected to in plane stress reversals. Proceedings of AMPT 1, 407-412.

Lavrentev, F.F., 1980. The type of dislocation interaction as the factor determining work hardening. Materials Science and Engineering 46, 191-208.

Lebensohn, R.A., Kanjarla, A.K., Eisenlohr, P., 2012. An elasto-viscoplastic formulation based on fast Fourier transforms for the prediction of micromechanical fields in polycrystalline materials. Int. J. Plast. 32-33, 59-69.

Lebensohn, R.A., Tomé, C.N., 1993. A self-consistent anisotropic approach for the simulation of plastic deformation and texture development of polycrystals: Application to zirconium alloys. Acta Metall. Mater. 41, 2611-2624.

Li, L., Shen, L., Proust, G., 2014. A texture-based representative volume element crystal plasticity model for predicting Bauschinger effect during cyclic loading. Materials Science and Engineering: A 608, 174-183.

Lipinski, P., Berveiller, M., 1989. Elastoplasticity of micro-inhomogeneous metals at large strains. Int. J. Plast. 5, 149-172.

Lopes, A.B., Rauch, E.F., Gracio, J.J., 1999. Textural vs structural plastic instabilities in sheet metal forming. Acta. Mater. 47, 859-866.

McDowell, D.L., 1992. A nonlinear kinematic hardening theory for cyclic thermoplasticity and thermoviscoplasticity. Int. J. Plast. 8, 695-728.

Mecking, H., Kocks, U.F., 1981. Kinetics of flow and strain-hardening. Acta Metall. Mater. 29, 1865-1875.

Miao, W.F., Laughlin, D.E., 1999. Precipitation hardening in aluminum alloy 6022. Scripta Materialia 40, 873-878.

Mirihanage, W.U., Robson, J.D., Mishra, S., Hidalgo-Manrique, P., da Fonseca, J.Q., Daniel, C.S., Prangnell, P.B., Michalik, S., Magdysyuk, O.V., Connolley, T., Drakopoulos, M., 2021. Direct observation of the dynamic evolution of precipitates in aluminium alloy 7021 at high strain rates via high energy synchrotron X-rays. Acta. Mater. 205, 116532.

Mompiou, F., Caillard, D., Legros, M., Mughrabi, H., 2012. In situ TEM observations of reverse dislocation motion upon unloading in tensile-deformed UFG aluminium. Acta. Mater. 60, 3402-3414.

Mughrabi, H., 1983. Dislocation wall and cell structures and long-range internal stresses in deformed metal crystals. Acta Metall. 31, 1367-1379.

Nagtegaal, J.C., Veldpaus, F.E., 1984. On the implementation of finite strain plasticity equations in a numerical model. Numerical methods in industrial forming processes, 351-371.

Neil, C.J., Wollmershauser, J.A., Clausen, B., Tomé, C.N., Agnew, S.R., 2010. Modeling lattice strain evolution at finite strains and experimental verification for copper and stainless steel using in situ neutron diffraction. Int. J. Plast. 26, 1772-1791.

Nieh, T.G., Nix, W.D., 1986. Unloading yield effects in aluminum alloys. Metallurgical transactions. A, Physical metallurgy and materials science 17 A, 121-126.

Noma, N., Kuwabara, T., 2012. Specimen geometry optimization for in-plane reverse loading test of sheet metal and experimental validation. Steel Research International Special Edition: Metal Forming 2012, 1283-1286.

Ohno, N., 1982. A Constitutive Model of Cyclic Plasticity With a Nonhardening Strain Region. J. Appl. Mech. 49(4), 721-727

Ohno, N., Kachi, Y., 1986. A Constitutive Model of Cyclic Plasticity for Nonlinear Hardening Materials. J. Appl. Mech. 53(2), 395-403.

Orowan, E., 1948. Discussion on internal stresses, Symposium on internal stresses in metals and alloys. Institute of Metals London, pp. 451-453.

Orowan, E., 1959. Causes and Effects of Internal Stresses, General Motors Symposium, ed. G.M. Rassweiler and W.L. Grube. Elsevier, Amsterdam, pp. 59-80.

Pavlina, E., Lee, M.-G., Barlat, F., 2015. Observations on the Nonlinear Unloading Behavior of Advanced High Strength Steels. Metall. Mater. Trans. A 46, 18-22.

Peeters, B., Seefeldt, M., Teodosiu, C., Kalidindi, S.R., Van Houtte, P., Aernoudt, E., 2001. Work-hardening/softening behaviour of b.c.c. polycrystals during changing strain paths: I. An integrated model based on substructure and texture evolution, and its prediction of the stress-strain behaviour of an IF steel during two-stage strain paths. Acta. Mater. 49, 1607-1619.

Poulin, C.M., Vogel, S.C., Korkolis, Y.P., Kinsey, B.L., Knezevic, M., 2020. Experimental studies into the role of cyclic bending during stretching of dual-phase steel sheets. International Journal of Material Forming 13, 393-408.

Prabhu, T.R., 2015. An Overview of High-Performance Aircraft Structural Al Alloy-AA7085. Acta Metall. Sin. (Engl. Lett.) 28, 909-921.

Sauzay, M., 2008. Analytical modelling of intragranular backstresses due to deformation induced dislocation microstructures. Int. J. Plast. 24, 727-745.

Seeger, A., 1957. Glide and work hardening in face-centered cubic and hexagonal close-packed metals, in: Fisher, J.C. (Ed.), Dslocations and Mechanical Properties of Cryslals, Wiley, New York, p. p.243.

Segurado, J., Lebensohn, R.A., Llorca, J., Tomé, C.N., 2012. Multiscale modeling of plasticity based on embedding the viscoplastic self-consistent formulation in implicit finite elements. Int. J. Plast. 28, 124-140.

Sehitoglu, H., Foglesong, T., Maier, H.J., 2005. Precipitate effects on the mechanical behavior of aluminum copper alloys: Part II. Modeling. Metall. Mater. Trans. A 36, 763-770.

Smith, A., Chen, Z., Lee, J.Y., Lee, M.G., Wagoner, R.H., 2014. Effective method for fitting complex constitutive equations. Int. J. Plast. 58, 100-119.

Sritharan, T., Chandel, R.S., 1997. Phenomena in interrupted tensile tests of heat treated aluminium alloy 6061. Acta. Mater. 45, 3155-3161.

Stout, M., Rollett, A., 1990. Large-strain Bauschinger effects in fcc metals and alloys. Metall. Mater. Trans. A 21, 3201-3213.

Szczepiński, W., 1990. Experimental methods in mechanics of solids. Elsevier

Tan, Z., Magnusson, C., Persson, B., 1994. The Bauschinger effect in compression-tension of sheet metals. Mater. Sci. Eng. A 183, 31-38.

Tanaka, K., Mori, T., 1970. The hardening of crystals by non-deforming particles and fibres. Acta Metallurgica 18, 931-941.

Taylor, G.I., 1938. Plastic strain in metals. Journal of the Institute of Metals 62, 307-324.

Teodosiu, C., Raphanel, J.L., 1991. Finite element simulations of large elastoplastic deformations of multicrystals. Proceedings of the International Seminar MECAMAT91, 153-168.

Turner, P.A., Tomé, C.N., 1994. A study of residual stresses in Zircaloy-2 with rod texture. Acta Metall. Mater. 42, 4143-4153.

Verma, R.K., Kuwabara, T., Chung, K., Haldar, A., 2011. Experimental evaluation and constitutive modeling of non-proportional deformation for asymmetric steels. Int. J. Plast. 27, 82-101.

Wagoner, R.H., Lim, H., Lee, M.-G., 2013. Advanced Issues in springback. Int. J. Plast. 45, 3-20.

Wen, W., Borodachenkova, M., Tomé, C.N., Vincze, G., Rauch, E.F., Barlat, F., Grácio, J.J., 2015. Mechanical behavior of Mg subjected to strain path changes: Experiments and modeling. International Journal of Plasticity 73, 171-183.

Weng, G.J., 1979. Kinematic hardening rule in single crystals. International Journal of Solids and Structures 15, 861-870.

Weng, G.J., 1980. Constitutive equations of single crystals and polycrystalline aggregates under cyclic loading. International Journal of Engineering Science 18, 1385-1397.

Wilson, D.V., Bate, P.S., 1986. Reversibility in the work hardening of spheroidised steels. Acta Metall. 34, 1107-1120.

Wilson, D.V., Zandrahimi, M., Roberts, W.T., 1990. Effects of changes in strain path on work-hardening in CP aluminium and an Al-Cu-Mg alloy. Acta Metall. Mater. 38, 215-226.

Wollmershauser, J.A., Clausen, B., Agnew, S.R., 2012. A slip system-based kinematic hardening model application to in situ neutron diffraction of cyclic deformation of austenitic stainless steel. Int. J. Fatigue 36, 181-193.

Wu, P.D., MacEwen, S.R., Lloyd, D.J., Jain, M., Tugcu, P., Neale, K.W., 2005. On pre-straining and the evolution of material anisotropy in sheet metals. International Journal of Plasticity 21, 723-739.

Yoshida, F., Uemori, T., Fujiwara, K., 2002. Elastic–plastic behavior of steel sheets under in-plane cyclic tension–compression at large strain. Int. J. Plast. 18, 633-659.

Zang, S.-l., Lee, M.-g., Hoon Kim, J., 2013. Evaluating the significance of hardening behavior and unloading modulus under strain reversal in sheet springback prediction. International Journal of Mechanical Sciences 77, 194-204.

Zecevic, M., Beyerlein, I.J., Knezevic, M., 2017a. Coupling elasto-plastic self-consistent crystal plasticity and implicit finite elements: Applications to compression, cyclic tension-compression, and bending to large strains. Int. J. Plast. 93, 187-211.

Zecevic, M., Knezevic, M., 2015. A dislocation density based elasto-plastic self-consistent model for the prediction of cyclic deformation: Application to Al6022-T4. Int. J. Plast. 72, 200-217.

Zecevic, M., Knezevic, M., 2017. Modeling of Sheet Metal Forming Based on Implicit Embedding of the Elasto-Plastic Self-Consistent Formulation in Shell Elements: Application to Cup Drawing of AA6022-T4. JOM 69, 922-929.

Zecevic, M., Knezevic, M., 2018. Latent hardening within the elasto-plastic self-consistent polycrystal homogenization to enable the prediction of anisotropy of AA6022-T4 sheets. Int. J. Plast. 105, 141-163.

Zecevic, M., Knezevic, M., 2019. An implicit formulation of the elasto-plastic self-consistent polycrystal plasticity model and its implementation in implicit finite elements. Mechanics of Materials 136, 103065.

Zecevic, M., Knezevic, M., Beyerlein, I.J., McCabe, R.J., 2016. Origin of texture development in orthorhombic uranium. Mater. Sci. Eng. A 665, 108-124.

Zecevic, M., Pantleon, W., Lebensohn, R.A., McCabe, R.J., Knezevic, M., 2017b. Predicting intragranular misorientation distributions in polycrystalline metals using the viscoplastic self-consistent formulation. Acta. Mater. 140, 398-410.

Zecevic, M., Upadhyay, M.V., Polatidis, E., Panzner, T., Van Swygenhoven, H., Knezevic, M., 2019. A crystallographic extension to the Olson-Cohen model for predicting strain path dependence of martensitic transformation. Acta. Mater. 166, 386-401.

Zhou, C., LeSar, R., 2012. Dislocation dynamics simulations of the Bauschinger effect in metallic thin films. Computational Materials Science 54, 350-355.

Chapter 3:

Elasto-plastic self-consistent crystal plasticity-based finite element simulations of hat-shaped draw-bending and b-pillar stamping to predict springback behavior of dual-phase steels.

For this chapter, the experimental results for DP 780 top-hat bending has been taken from the paper *An Applictaion of Homogeneous anisotropic hardening to springback prediction in pre-strained U-draw/bending by Jeong- Yeon Lee, Ji Woo Lee, Myuong-Gyu Lee, Frederic Barlat,* the simulated results were carried out in EPSC.

Elasto-plastic self-consistent crystal plasticity-based finite element simulations of hat-shaped draw-bending and b-pillar stamping to predict springback behavior of dual-phase steels

Sowmya Daroju, Marko Knezevic3

Department of Mechanical Engineering, University of New Hampshire, Durham, NH 03824,

USA

Abstract

The detailed contribution of microstructural evolution such as dislocation structure development and annihilation, as well as inter-granular and intra-granular backstress fields to the phenomena such as unloading nonlinearity, the Bauschinger effect (BE), and changes in hardening rates during reverse loading remains an area of active research and debate. This work is concerned with predicting geometrical shape changes in sheet metal forming using a multi-level simulation framework that considers such microstructural evolution and the directionality of deformation mechanisms acting at single-crystal level. The underlying model is the elasto-plastic self-consistent (EPSC) homogenization of single-crystal behavior providing a constitutive response at each finite element (FE) integration point, within the boundary value problem solved using continuum finite elements at the macro-level. First, the model parameters associated with the slip strengths of ferrite and martensite and backstress are established by reproducing a comprehensive set of mechanical data for dual-phase (DP) steels 590, 780, and 1180 using one-

---

* Corresponding author at: University of New Hampshire, Department of Mechanical Engineering, 33 Academic Way, Kingsbury Hall, W119, Durham, New Hampshire 03824, United States. Tel.: 603 862 5179; fax: 603 862 1865. E-*mail address*: marko.knezevic@unh.edu (M. Knezevic).

element model. Next, the potential of the modeling framework is illustrated by simulating hat-shaped draw-bending and b-pillar stamping of steel sheets. Consistent with experimental measurements, the process simulations using FE-EPSC predict geometry in hat-shaped draw-bending with satisfactory accuracy for DP 780. In doing so, the role of accounting for backstress is revealed as critical for the accurate prediction of the part. Next, the same process simulation involving pre-strained sheet of DP 780 reveals the role of strain hardening and residual stress on subsequent part shape predictions in hat-shaped draw-bending. Finally, the same process simulations involving DP 590 and DP 1180 further confirm the effect of strength on geometrical changes of the part. Good predictions demonstrate that the FE-EPSC modeling framework can be used to predict phenomena pertaining to constitutive behavior of steels and resulting geometrical changes important for optimization of the sheet metal forming processes.

Keywords: Microstructures; Crystal plasticity; Anisotropic material; Numerical algorithms; AA6022-T4

1 Introduction

There is a competition among automobile companies to produce light weight vehicles with lower fuel consumption and gas emission due to strict environmental regulations. The main structure of an automobile is usually made of steels. As advanced steels of complex microstructures are being developed and considered to strengthen and lighten structures, the sophistication of constitutive laws necessary to accurately model their deformation behavior also evolves (Tasan et al., 2014). Premier examples of steels aimed at weight reduction of automobiles are dual-phase (DP) advanced-high strength steels (AHSS) due to their excellent ductility and formability. These steels contain variable fractions of martensite and ferrite phases of slightly different crystal structures but highly contrasting mechanical characteristics in their microstructure (Woo et al., 2012). Therefore, properties of these steels are primarily governed by the volume fraction and distribution of the phases. Predicting geometrical shape changes and strength during sheet metal forming is essential for sheet forming process optimization (Rabahallah et al., 2009). In attempting to predict final geometry, simulating springback after unloading is essential, especially for alloys exhibiting a large magnitude of springback due to high flow stress such as DP steels (Pavlina et al., 2015; Wagoner et al., 2013). The application of high strength steels is often hampered by large springback (Yoshida et al., 2013). This work is concerned with predicting the geometry and variation in dimensional changes resulting from different strength of various DP steels during hat-shaped draw-bending and b-pillar stamping.

Springback is the elastic deformation of the sheet metal parts after unloading due to the action of internal stresses. This elastic recoveries is one of the main sources in the geometrical inaccuracies in the products of sheet metal forming processes. Springback introduces surface distortions and unexpected out of shape tolerances that not only cause deviations from the

104

designed target shapes in the products but also can lead to assembly problems. Since higher material strength causes higher springback effect, it has become an important issue in automotive industries which utilizes higher strength steel sheets for manufacturing automotive parts (Lee et al., 2011). For the same reason great efforts have been carried to predict springback using finite element (FE) simulations.

Simulations of deformation are vital to the optimization of metal forming operations as well as the evaluation of component performances in service (Hosford and Caddell, 1993). A constitutive law representing material behavior under an applied deformation is needed to solve the fundamental balance of linear momentum governing equation of mechanics. The solution over a given geometry in terms of a pair of work-conjugated stress and strain measures is usually sought numerically using the finite elements method (FEM) (Bathe, 1996). Reliability of such simulations is dependent on a selected constitutive law. As metal forming operations consist of non-monotonic deformation paths along with frequent unloading, the constitutive law must be able to represent the material response under such complex deformation conditions. For example, bending-unbending of a metallic sheet drawn over a die radius operation induces tension followed by compression deformation (Chun et al., 2002; Knezevic et al., 2019; Poulin et al., 2020a; Poulin et al., 2019; Poulin et al., 2020b; Wagoner et al., 2013). Subsequent removal/unloading of the part from the die results in springback deformation/deflection (Barrett et al., 2020; Boger et al., 2005; Li et al., 2002; Wagoner et al., 2013). Predicting such material behavior and resulting geometry requires sophisticated elasto-plastic constitutive laws able to represent transients in yield stress (the Bauschinger effect, BE), changes in the anisotropic hardening rates during strain-path changes from those during monotonic loading, and unloading. These phenomena pertaining to the material behavior originate from the evolution of the

underlying microstructure, mainly the strain-path sensitive evolution of dislocations, intra-granular backstress fields, and inter-granular stresses fields.

The first phenomenon to occur upon a strain-path change deformation can be the unloading of a strained material (Deng et al., 2015; Pavlina et al., 2015; Sritharan and Chandel, 1997; Yoshida et al., 2002). The unloading is initially liner but then nonlinear. The source of the nonlinear portion of unloading is a partial re-emission of dislocations piled-up at grain/phase boundaries during prior straining (Mompiou et al., 2012; Sritharan and Chandel, 1997). The re-emission of such dislocations is accompanied by the relaxation of micro-backstress fields (Sritharan and Chandel, 1997). The emitted dislocations quickly become the forest dislocations causing hardening (Dotsenko, 1979; Kruml et al., 2008; Mohebbi et al., 2015). The subsequent phenomenon proceeding after the unloading is the BE. The primary origin of BE are intra-granular backstress fields caused by various incompatibilities in grains (Demir and Raabe, 2010; Gough et al., 1927; Kassner et al., 2013; Mughrabi, 1983). The secondary origin of BE are inter-granular backstress fields caused by the anisotropy between grains of distinct crystal orientation (Abel, 1987; Nieh and Nix, 1986; Stout and Rollett, 1990; Verma et al., 2011). The incompatibilities are greater between grains of different phases than in grains of the same phase because of a greater strength differential between phases than between grains of the same phase (Brown and Stobbs, 1971; Kadkhodapour et al., 2011; Nesterova et al., 2015; Taupin et al., 2013). These internal stresses whether intra- or inter-granular act against the applied loading. After a strain-path change, these fields combine with the applied loading causing a transient in the yield stress. The following phenomenon is a change in strain hardening governed by a competition between annihilation/dissolution of existing dislocations and formation of new

dislocations with plastic strain (Kitayama et al., 2013b; Stout and Rollett, 1990; Wilson et al., 1990).

Macroscopic plasticity models represent the phenomena directly using isotropic and kinematic hardening laws without accounting for microstructural evolution (Armstrong and Frederick, 1966; Chaboche and Rousselier, 1983; Chaboche, 1977; Chaboche, 2008; Hu et al., 1992; McDowell, 1992). These models are formulated with many adjustable parameters for representing the phenomena. Identification of the parameters is involved and often require a set of specialized mechanical tests (Feng et al., 2020; Smith et al., 2014). More accurate simulations of sheet metal forming operations can be facilitated with material models capable of representing the above summarized microstructural evolution governing the phenomena (Li et al., 2002; Sharma et al., 2021). Since microstructure sensitive, these models are not tied to a specific material state. The type of models providing flexibility to incorporate the microstructure-based physics of deformation are based on crystallography of deformation mechanisms and termed crystal plasticity models. A crystallography-based elasto-plastic self-consistent (EPSC) model incorporating the microstructure-level processes has been recently formulated (Zecevic et al., 2016b). The initial study on DP590 successfully benchmarked the model against monotonic and load reversal deformation of DP 590. Specifically, the model features a dislocation-based hardening law and accounts for anisotropic elasticity and underlying inter-granular stress fields and intra-granular backstress sources at the slip system level.

In the current work, data from a comprehensive campaign of mechanical testing on the DP 590, DP 780, and DP 1180 steel sheet is presented, and used to calibrate and validate the model. To initialize the model, texture per steel was measured using neutron diffraction (NeD). The model parameters associated with the slip strengths of ferrite and martensite and backstress are

established. Good predictions demonstrated the ability of crystal plasticity modeling to account for the co-dependent nature of crystallographic slip in ferrite and martensite and the sources of hardening caused by history-dependent dislocation density evolution and backstress to predict not only monotonic but also hysteresis in plastic response during the forward-reversal cycles. Therefore, the model can predict the phenomena of hardening rates during monotonic tension and compression, linear and then a non-linear unloading, the BE, and hardening rates during continuous straining in the opposite direction along with the permanent softening, as a function of loading history for all steels. Experiments characterizing of hat-shaped draw-bending for DP 718 was presented in (Lee et al., 2012). The operation of hat shaped-draw-bending involves non-monotonic deformation paths - the material inside walls undergoes bending- reverse bending, and unloading. Bending – reverse bending of a metallic sheet over a die radius causes tension followed by compression, which is followed by the springback after removal from the die. The data was used here for a detailed validation of the material model in predicting geometry of the hat-shaped part from virgin and pre-strained sheets. After verifying the model in capturing the geometry and punch force displacement, the model was use to predict the same forming of DP 590 and DP 1180. Insights from these predictions are presented and discussed in the paper. In particular, the role of accounting for backstress for the accurate prediction of the geometry is discussed.

2 Simulation setups

The finite element model for hat-shaped draw-bending is carried out in Abaqus/standard. The drawing of the setup is presented in Fig. 1. Half of the section was modelled considering the

process of symmetry, as shown in Fig. 2. The tools (die, punch, and holder) were modelled as rigid analytical surfaces and the blank was meshed with plane strain (linear and quadratic with and without reduced integration) elements considering 2 and 4 elements through thickness. The length of the blank is considered as 180 mm (half of the original length, due to symmetry) and the thickness of the blank as 1.4 mm, the blank holding force of 2.94 KN is used, and the friction constant is considered as 0.1 between the tool and the blank. The final displacement of the punch is considered to be 71.8mm. Two different types of simulation were performed (1) with prestrain and (2) without prestrain. The simulation of prestrained hat-shaped bending consisted of 5 steps; (1) prestraining (2) unloading (3) blank holding (4) draw/bending and (5) final unloading. The first 2 steps were omitted for without pre-strain. After final unloading the spring back profiles were obtained.
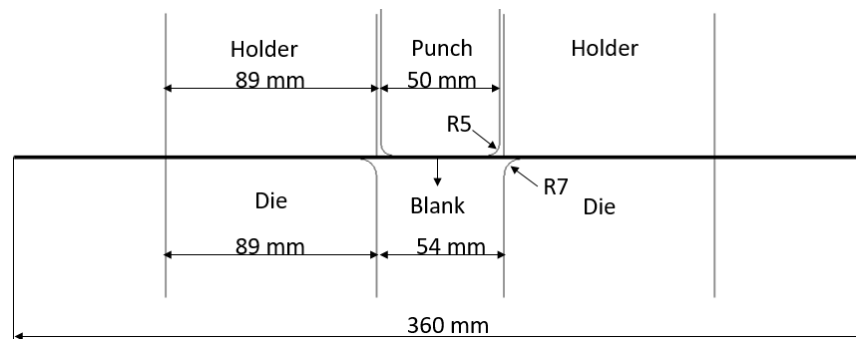
Fig. 1: Drawing of the setup for hat-shaped draw-bending process. The sheet is 360 mm long and 1.4 mm thick.
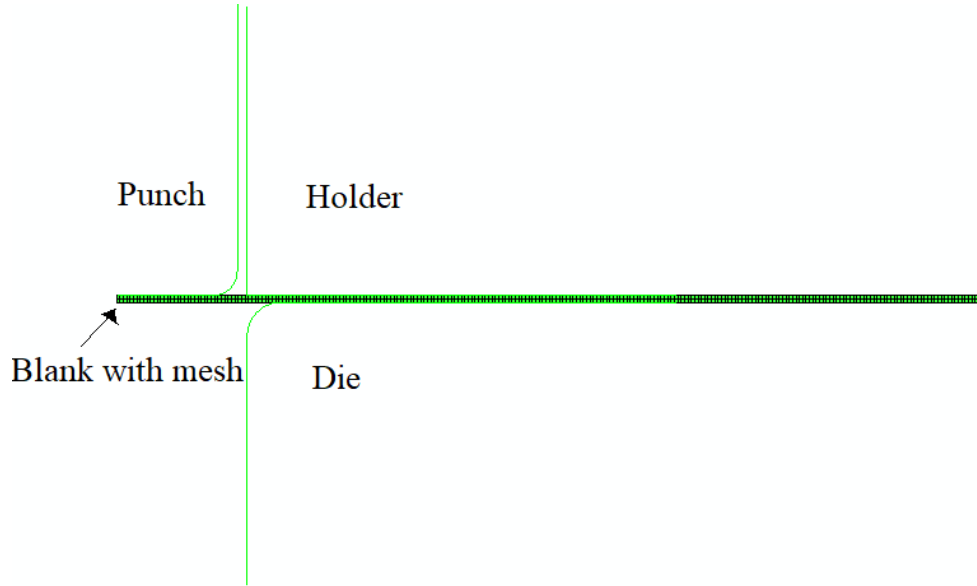
Fig. 2: Simulation setup (half model) for hat-shaped draw-bending.

3 Materials

The simulations performed in this work involved sheets of DP 590, DP 780, and DP 1180. The steel sheets were obtained from the United States Steel Corporation (US Steel). DP 590 and DP 780 were processed using the hot dip (HD) processing line, while DP1180 was processed using the continuous annealing line (CAL). DP 590 and DP 780 steels sheets were galvannealed (HDGA) coated, while DP 1180 was bare. Chemical compositions are provided in Table 1. The thicknesses of the sheets were 1.4 mm for DP 590 and DP 780 and 1 mm for DP 1180. These steel sheets are commonly used for various structure and auto-body applications.

The three steels offer a tradeoff between strength and ductility owing to their underlying microstructures, which consists of a relatively soft but ductile ferritic phase and a hard but brittle martensitic phase (Calcagnotto et al., 2012; Ghaei et al., 2015; Gong et al., 2016; Kudzal et al., 2020; Ma et al., 2016; Woo et al., 2012; Zecevic et al., 2019). Further improvements in strength

110

and ductility of DP steels are possible by altering the composition, phase distribution, grain size, and crystallographic texture per phase (Bhargava et al., 2018; Calcagnotto et al., 2011). Imaging of the structures by secondary electrons (SE) for determining phase fractions, electron backscatter diffraction (EBSD) for determining grain structure, and neutron diffraction for determining texture for the steels used in the present work was performed in our earlier work (Daroju et al., 2022; Poulin et al., 2020b). The phase fractions are given in Table 2.

Monotonic and large strain cyclic tension-compression experiments to evaluate the monotonic and load reversal behavior of the steels was performed in (Daroju et al., 2022). Figure 3 shows measured monotonic and tension-compression-tension reversal true stress-true strain curves along the rolling direction (RD). The load reversal curves involve monotonic tension to a given strain level. The second loading path is compression to zero strain (1st reversal). The third loading path is tension to rupture (2nd reversal). The steels show the decreasing hardening rate during the monotonic tension path, which is common for alloys in which the plasticity is accommodated by crystallographic slip. Upon the 1st reversal, the steels show an initial linear portion, which is followed by a non-linear portion of unloading. Reyield points in unloading at 0.001 offset are indicated (σU). Following the reyielding, the steels exhibit transient softening, which is the BE. Following the BE is the permanent softening, which is a drop of the flow curves when the reverse curve is plotted in the direction of the prior straining. The EPSC constitutive law featuring a dislocation density law and a backstress law is calibrated and validated using the data. The model is described in the next section. In addition to phase fractions, texture per phase is needed to initialize the model for each steel. Fig. 4 shows measured pole figures visualizing the initial texture in the steels. The figure also shows the pole figures after data compaction for simulations. The measured textures were compacted to 100 weighted orientations for ferrite and

100 weighted orientations for martensite. Since DP 590 has ~93% of ferrite, the measured texture of DP 590 is that of ferrite. Likewise, since MS 1700 has ~85% of martensite, the measured texture of MS 1700 is that of martensite. The data compaction methodology was described in (Eghtesad et al., 2018). Texture in the steels is predominantly orthotropic typical of rolled sheets for body-centered cubic (BCC) metals. The crystal orientations concentrate around the γ-fiber and the α-fiber (Bhattacharyya et al., 2015; Holscher et al., 1994; Kocks et al., 1998). Evidently, the texture intensity reduces with the fraction of martensite. Texture in the martensite phase is initialized using the measured texture of the martensitic steel, MS 1700.

Table 1: Chemical composition of steels (wt%) used in the study.

Steel	C	Mn	P	S	Si	Cu	Ni	Cr	Mo
DP 590	0.073	1.97	0.014	0.006	0.017	0.04	0.01	0.2	0.172
DP 780	0.1	2.163	0.015	0.006	0.014	0.03	0.01	0.26	0.332
DP 1180	0.168	2.222	0.015	0.0053	1.421	0.021	0.007	0.036	0.013

	Sn	Al	Zr	V	Cb	Ti	B	N2
DP590	0.002	0.045		0.001			0.0001	0.005
DP780	0.003	0.048		0.001	0.003	0.001	0.0001	0.006
DP1180	0.007	0.051	0.005	0.012	0.007	0.039	0.0004	0.0086

Table 2: Volume fraction of martensite for the studied DP steels.

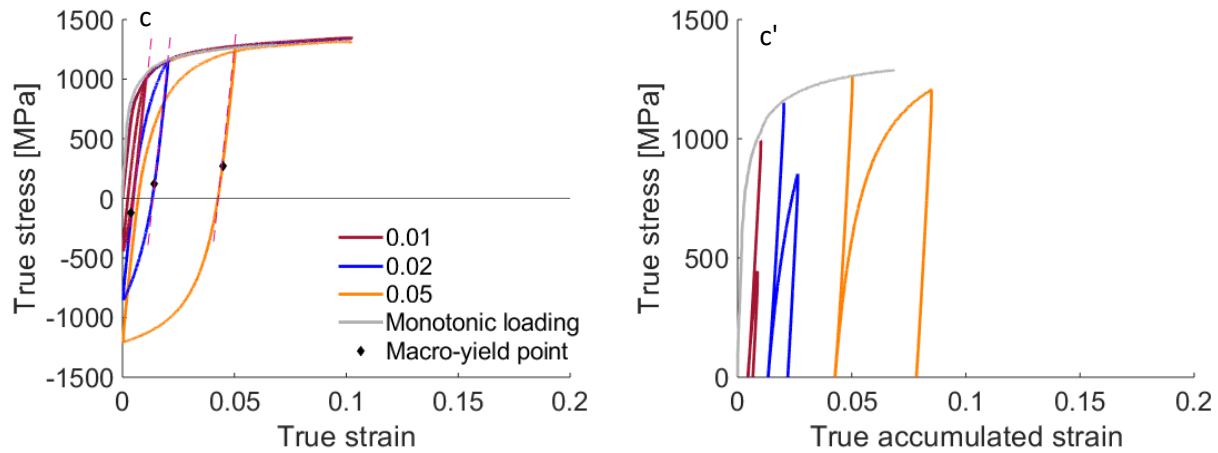| Steel	DP 590	DP 780	DP 1180
Fraction of martensite	7.7%	34%	45%
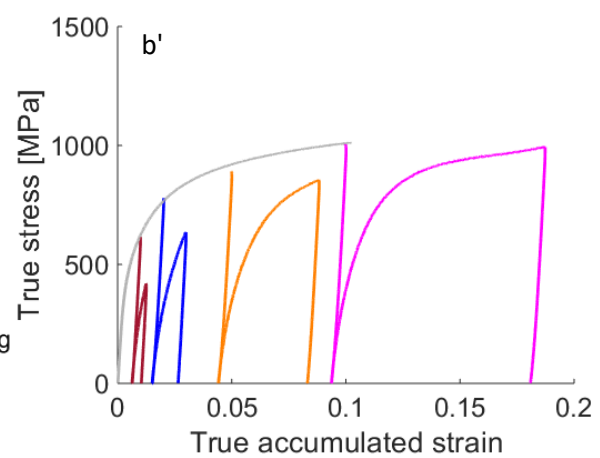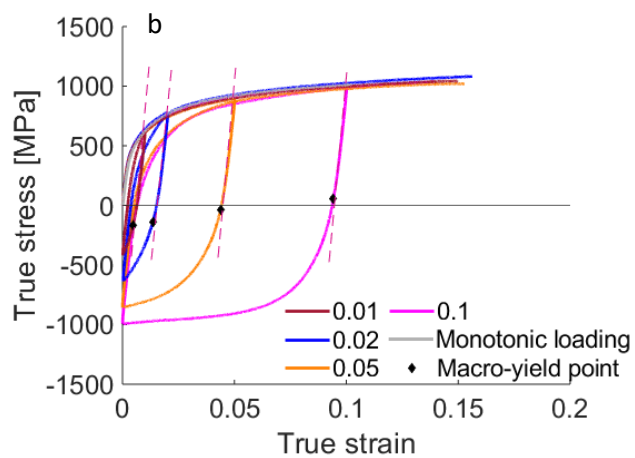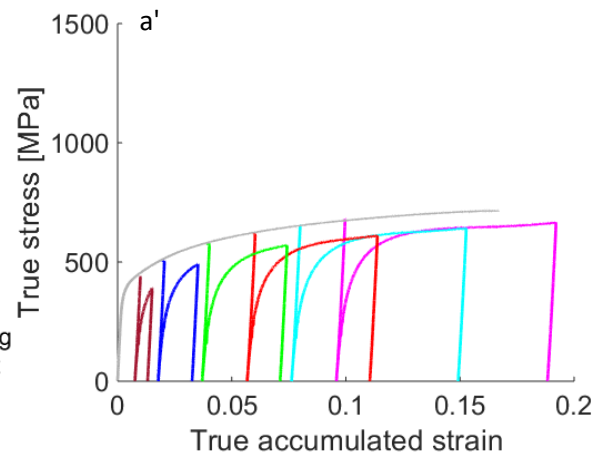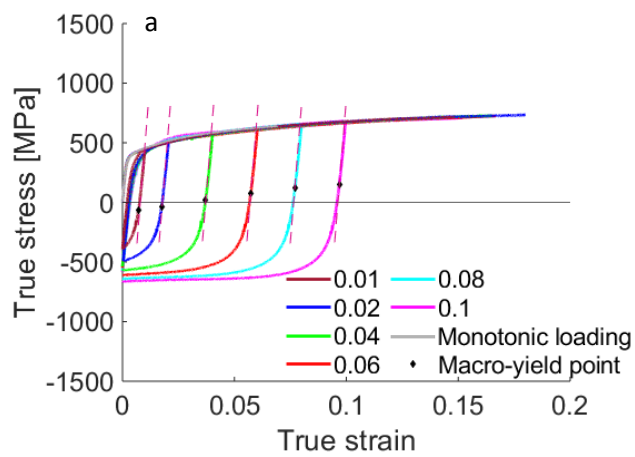
Figure 3. Stress–strain response measured during strain path reversals at large strain levels as indicated in the legends for (a) DP 590, (b) DP 780, and (c) DP 1180 along the rolling direction (RD). Macro-yield points upon unloading at 0.001 offset strain are indicated (σU). Comparison of monotonic tension and the 1st reversal curves as a function of accumulated strain for (a') DP 590, (b') DP 780, and (c') DP 1180.
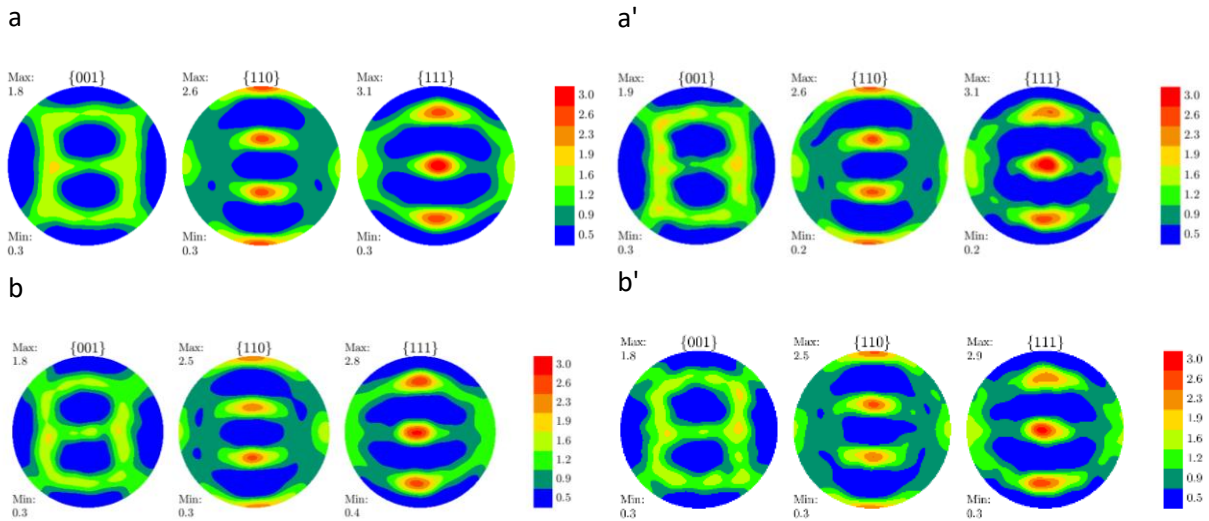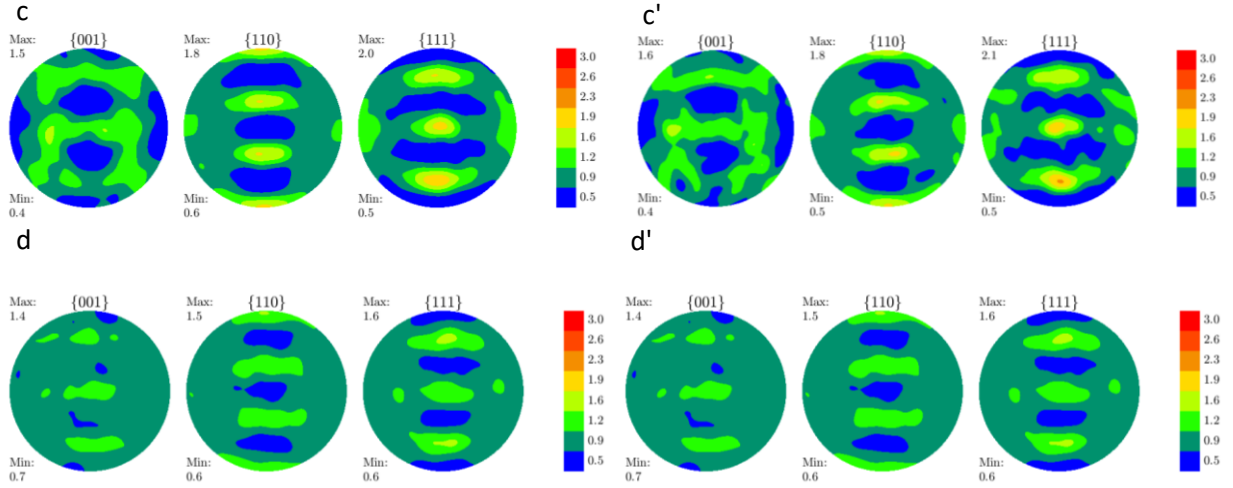
Figure 4. Stereographic pole figures measured using NeD showing the initial texture in sheets of (a) DP 590, (b) DP 780, (c) DP 1180, and (d) martensitic steel MS 1700. (a'-d') Corresponding pole figures represented using 100 weighted crystal orientations for simulations.

4 Summary of the elasto-plastic self-consistent crystal plasticity-based finite element simulation framework

This section summarizes the crystal plasticity constitutive law used to perform the simulations in the present work. The law is an implicit formulation of the EPSC model embedded in the implicit FEM framework (Zecevic and Knezevic, 2019). The model is termed FE-EPSC. The constitutive formulation of EPSC begins by relating the Jaumann rate of Cauchy stress, $\hat{\boldsymbol{\sigma}}$, and the strain rate, $\dot{\boldsymbol{\varepsilon}}$, using (Ghorbanpour et al., 2020; Nagtegaal and Veldpaus, 1984; Neil et al., 2010; Zecevic et al., 2015)

$$\hat{\boldsymbol{\sigma}} = \mathbf{L}\dot{\boldsymbol{\varepsilon}} = \dot{\boldsymbol{\sigma}} + \boldsymbol{\sigma}\mathbf{W} - \mathbf{W}\boldsymbol{\sigma}. \tag{1}$$

The constitutive equation applied equally whether a material point is a polycrystalline aggregate or a single crystal. The tensorial quantities in the equation, $\boldsymbol{\sigma}$, $\mathbf{L}$, and $\mathbf{W}$ are the Cauchy stress,

tangent stiffness, and spin respectively. These quantities at the crystal-level are denoted with the superscript c as $\widehat{\boldsymbol{\sigma}}^c$, $\mathbf{L}^c$, and $\mathbf{W}^c$. Additionally, the crystal stress and strain rate are $\boldsymbol{\sigma}^c$ and $\dot{\boldsymbol{\varepsilon}}^c$.

Using the crystal volume averages $\widehat{\boldsymbol{\sigma}} = \langle \widehat{\boldsymbol{\sigma}}^c \rangle$ and $\dot{\boldsymbol{\varepsilon}} = \langle \dot{\boldsymbol{\varepsilon}}^c \rangle$, $\mathbf{L}$ can be evaluated relying on the standard SC homogenization procedure (Eshelby, 1957; Ghorbanpour et al., 2017; Lipinski and Berveiller, 1989; Neil et al., 2010; Turner and Tomé, 1994). Dot and tensor products are indicated by $\cdot$ and $\otimes$, respectively.

The crystal-level Jaumann rate is

$$\widehat{\boldsymbol{\sigma}}^c = \mathbf{L}^c \dot{\boldsymbol{\varepsilon}}^c = \mathbf{C}^c (\dot{\boldsymbol{\varepsilon}}^c - \mathbf{m}_{sc}^s \dot{\gamma}^s) - \boldsymbol{\sigma}^c tr(\dot{\boldsymbol{\varepsilon}}^c), \tag{2}$$

with $\mathbf{C}^c$ and $\dot{\boldsymbol{\varepsilon}}^{pl,c}$ denoting the elastic stiffness tensor and the plastic strain rate for crystal c. The plastic strain rate is a sum of the products between the Schmid tensor, $\mathbf{m}_{sc}^s = \frac{1}{2}(\mathbf{b}^s \otimes \mathbf{n}^s + \mathbf{n}^s \otimes \mathbf{b}^s)$ and sharing rates, $\dot{\gamma}^s$ over available slip systems, s, per grain c. The geometry of Schmid tensors is defined by the Burgers vector, $\mathbf{b}^s$, and the slip system normal, $\mathbf{n}^s$, with a tangent $\mathbf{t}^s = \mathbf{n}^s \times \mathbf{b}^s$. Due to the core structure of dislocations in BCC metals, non-Schmid effects arise giving rise to some tension/compression asymmetry in the mechanical response (Dao and Asaro, 1993; Knezevic et al., 2014; Knezevic et al., 2015; Lim et al., 2013; Savage et al., 2017; Savage et al., 2018). Non-Schmid effects are typically included in the single crystal activation law via the non-Schmid tensor $\mathbf{m}_{ns}^{c,s}$. Here, five additional non-glide projections are included: three normal $\mathbf{n}^s \otimes \mathbf{n}^s$, $\mathbf{t}^s \otimes \mathbf{t}^s$, and $\mathbf{b}^s \otimes \mathbf{b}^s$ and two shear acting normal to the Burgers vector $\mathbf{t}^s \otimes \mathbf{b}^s$ and $\mathbf{t}^s \otimes \mathbf{n}^s$. The non-Schmid tensor and the total tensor governing the slip system activation are

$$\mathbf{m}_{ns}^s = c_1(\mathbf{t}^s \otimes \mathbf{b}^s) + c_2(\mathbf{t}^s \otimes \mathbf{n}^s) + c_3(\mathbf{n}^s \otimes \mathbf{n}^s) + c_4(\mathbf{t}^s \otimes \mathbf{t}^s) - (c_3 + c_4)(\mathbf{b}^s \otimes \mathbf{b}^s), \tag{3a}$$

$$\mathbf{m}^s = \mathbf{m}_{sc}^s + \mathbf{m}_{ns}^s. \tag{3b}$$

The four weighting coefficients, ci, referred as the non-Schmid coefficients are calibrated using mechanical data.

Activation of slip systems is then controlled by the following conditions

$$\boldsymbol{\sigma}^c \cdot \mathbf{m}^s - \tau_{bs}^s = \tau_c^s, \tag{4a}$$

$$\hat{\boldsymbol{\sigma}}^c \cdot \mathbf{m}^s - \dot{\tau}_{bs}^s = \dot{\tau}_c^s, \tag{4b}$$

where, τ_c^s is a resistance to slip, while τ_{bs}^s is a slip system backstress inducing the kinematic hardening effect (Wollmershauser et al., 2012). The condition in Eq. (4a) indicates that the stress is on the yield surface, while the condition in Eq. (4b) is the consistency ensuring that the stress stays on the yield surface (Knockaert et al., 2000; Zecevic et al., 2019). The resistance and backstress evolve using

$$\dot{\tau}_c^s = \sum_{s'} h^{ss'} \dot{\gamma}^{s'}, \tag{5a}$$

$$\dot{\tau}_{bs}^s = \sum_{s'} h_{bs}^{ss'} \dot{\gamma}^{s'}, \tag{5b}$$

where $h^{ss'}$ and $h_{bs}^{ss'}$ are matrices, one consisting of partial derivatives for hardening evolution, $h^{ss'} = \frac{\partial \tau_c^s}{\partial \gamma^{s'}}$, and another consisting of partial derivatives for backstress evolution, $h_{bs}^{ss'} = \frac{\partial \tau_{bs}^s}{\partial \gamma^{s'}}$. These partial derivatives are evaluated from the evolution laws for τ_c^s and τ_{bs}^s, which are described next.

Crystal lattice evolution with plastic strain is captured base on the spin tensor

$$\mathbf{W}^c = \mathbf{W}^{c,app} - \mathbf{W}^{pl,c}, \tag{6}$$

calculated as the sum of any applied spin $\mathbf{W}^{c,app}$ and plastic spin $\mathbf{W}^{pl,c}$. The plastic spin is calculated using $\mathbf{W}^{pl,c} = \sum_s \dot{\gamma}^s \mathbf{q}^s$ and $\mathbf{q}^s = \frac{1}{2}(\mathbf{b}^s \otimes \mathbf{n}^s - \mathbf{n}^s \otimes \mathbf{b}^s)$.

Resistance to slip is formulated to consist of (Knezevic et al., 2014; Knezevic et al., 2013; Zecevic et al., 2016a)

$$\tau_c^s = \tau_0^\alpha + \tau_{forest}^s + \tau_{debris}^\alpha, \tag{7}$$

where, τ_0^α is an initial nonevolving value, while τ_{forest}^s and τ_{debris}^α are evolving values of slip resistance. The latter two terms are driven by statistically stored forest and debris dislocation populations, respectively. τ_0^α includes the Peierls barrier, solid solution strengthening, initial dislocation density, and initial grain size strengthening through barrier effect. τ_{forest}^s and τ_{debris}^α are defined as

$$\tau_{forest}^s = b^\alpha \chi G^\alpha \sqrt{\sum_{s'} L^{ss'} \rho_{tot}^{s'}}, \tag{8a}$$

$$\tau_{debris}^\alpha = 0.086\, G^\alpha b^\alpha \sqrt{\rho_{deb}} log\left(\frac{1}{b^\alpha \sqrt{\rho_{deb}}}\right), \tag{8b}$$

where, b^α is the magnitude of Burgers vector, χ is an interaction constant for dislocations (Lavrentev, 1980; Mecking and Kocks, 1981) ($\chi = 0.9$), G^α is the shear modulus, $L^{ss'}$ is a latent hardening interaction matrix (Franciosi and Zaoui, 1982; Khadyko et al., 2016), ρ_{tot}^s is the total density of forest dislocations per slip system, ρ_{deb} is the density of debris dislocations.

The model features a strain-path sensitive law for the evolution of dislocation density governing the evolution of slip resistance. To facilitate the strain-path dependence, a positive, s+, and a negative, s-, slip directions for every s are identified. Note that every s belongs to a given slip family/mode α. Consequently, the total density of forest dislocation is formulated as

$$\rho_{tot}^s = \rho_{for}^s + \rho_{rev}^{s^+} + \rho_{rev}^{s^-}, \tag{9}$$

where, ρ_{for}^s is the forward and $\rho_{rev}^{s^+}$ and $\rho_{rev}^{s^-}$ are the reversible densities of dislocations on the

s+ and s- , respectively. The evolution laws for these densities with shearing are (Kitayama et al.,

2013a; Zecevic and Knezevic, 2019)

(If $d\gamma^{s^+} > 0$)

$$\frac{\partial \rho_{for}^s}{\partial \gamma^s} = (1-p)k_1^\alpha \sqrt{\rho_{tot}^s} - k_2^\alpha(\dot{\varepsilon}, T)\rho_{for}^s, \tag{10a}$$

$$\frac{\partial \rho_{rev}^{s^+}}{\partial \gamma^s} = p k_1^\alpha \sqrt{\rho_{tot}^s} - k_2^\alpha(\dot{\varepsilon}, T)\rho_{rev}^{s^+}, \tag{11a}$$

$$\frac{\partial \rho_{rev}^{s^-}}{\partial \gamma^s} = -k_1^\alpha \sqrt{\rho_{tot}^s} \left(\frac{\rho_{rev}^{s^-}}{\rho_0^s}\right)^m, \tag{12a}$$

(If $d\gamma^{s^-} > 0$)

$$\frac{\partial \rho_{for}^s}{\partial \gamma^s} = (1-p)k_1^\alpha \sqrt{\rho_{tot}^s} - k_2^\alpha(\dot{\varepsilon}, T)\rho_{for}^s, \tag{10b}$$

$$\frac{\partial \rho_{rev}^{s^+}}{\partial \gamma^s} = -k_1^\alpha \sqrt{\rho_{tot}^s} \left(\frac{\rho_{rev}^{s^+}}{\rho_0^s}\right)^m, \tag{11b}$$

$$\frac{\partial \rho_{rev}^{s^-}}{\partial \gamma^s} = p k_1^\alpha \sqrt{\rho_{tot}^s} - k_2^\alpha(\dot{\varepsilon}, T)\rho_{rev}^{s^-}, \tag{12b}$$

with $\rho_{for}^s(\gamma^s = 0) = \rho_{initial}^s$, $\rho_{rev}^{s^+}(\gamma^s = 0) = 0$ and $\rho_{rev}^{s^-}(\gamma^s = 0) = 0$. In the evolution

expressions, k_1^α is a fitting model parameter determining the rate of generation of forest

dislocations, while k_2 is controlling recovery of forest dislocations (Beyerlein and Tomé, 2008),

p is a reversibility parameter taken as unity (Khadyko et al., 2016; Kocks et al., 1991; Teodosiu

and Raphanel, 1991), m is a model parameter limiting the rate of recombination of dislocations

taken as 0.5 (Wen et al., 2015), and ρ_0^s is the density of dislocations at the strain-path change on

the system, s (Kitayama et al., 2013a).

k_2^α is calculated using

$$\frac{k_2^\alpha}{k_1^\alpha} = \frac{\chi b^\alpha}{g^\alpha}\left(1 - \frac{k_B T}{D^\alpha (b^\alpha)^3} ln\left(\frac{\dot{\varepsilon}}{\dot{\varepsilon}_0}\right)\right), \tag{13}$$

where k_B is the Boltzmann constant, D^α is the drag stress model parameter, g^α is the effective activation enthalpy model parameter, and $\dot{\varepsilon}_0 = 10^7$ is the a reference strain rate. The debris density of dislocations increments using

$$\sum_s \frac{\partial \rho_{deb}}{\partial \gamma^s} d\gamma^s = \sum_s q^\alpha b^\alpha \sqrt{\rho_{deb}} \, k_2^\alpha(\dot{\varepsilon}, T)\rho_{tot}^s d\gamma^s, \tag{14}$$

where q^α is another fitting model parameter for the rate of dislocation recovery.

In addition to the a strain-path sensitive dislocation density-based law for the evolution of slip system resistance, the model incorporates a slip system level backstress law to influence the resolved shear stress for slip system activation. The intra-granular sources of backstress are represented phenomenologically. The sources of backstress evolve with shearing strain. The sources on individual slip systems are summed to form the backstress tensor (Harder, 1999). The tensor is then projected get the slip system backstress as

$$\tau_{bs}^s = \mathbf{m}^s \cdot \boldsymbol{\sigma}_{bs}^c = \tau_{bs,sys}^s + 2\sum_{s'} \mathbf{m}^s \cdot \mathbf{m}^{s'} \tau_{bs,sys*}^{s'} , \tag{15}$$

where

$$\tau_{bs,sys*}^{s'} = \begin{cases} \tau_{bs,sys}^{s'} \text{ if } \tau_{bs,sys}^{s'} > 0 \\ 0 \text{ if } \tau_{bs,sys}^{s'} < 0 \end{cases}. \tag{16}$$

The slip system level back-stress is

(if $d\gamma^{s^+} > 0$ and $\tau_{bs,sys}^{s^+} > 0$)

$$\tau_{bs,sys}^{s^+} = \tau_{bs}^{sat}\left(1 - \exp\left(-\nu\gamma^{s^+}\right)\right), \tag{17}$$

$$\tau_{bs,sys}^{s^-} = -A\tau_{bs,sys}^{s^+}, \tag{18}$$

(if $d\gamma^{s^+} > 0$ and $\tau_{bs,sys}^{s^+} < 0$)

$$\tau_{bs,sys}^{s^+} = -(A+1)\tau_{bs}^{sat} \exp\left(-\frac{\gamma^{s^-}}{\gamma_b}\right) + \tau_{bs}^{sat}, \tag{19}$$

$$\tau_{bs,sys}^{s^-} = -\frac{1}{A}\tau_{bs,sys}^{s^+}. \tag{20}$$

The fitting parameters for the backstress law are the saturation value, τ_{bs}^{sat}, the parameter, A, which influences the asymmetric evolution in s+ and s-, the multiplier, ν, and the denominator, γ_b.

In addition to the intra-granular sources, the backstress fields arise from inter-granular interactions between individual grains of different crystal orientations in polycrystals. These additional sources are approximated in the EPSC model using the SC homogenization in which every grain interacts with the averaged polycrystalline response. Modeling anisotropic elasticity is essential for accurate predictions of the inter-granular stress fields. In summary, the predictive characteristics of the EPSC model are a collective result of accounting for several distinct physical phenomena, the strain-path sensitive evolution of dislocation density, intra-granular backstress fields, and inter-granular stress fields. Local stresses in every grain are a consequence of the applied stress, inter-granular backstress fields, and intra-granular backstress fields.

The EPSC model has been couples with the implicit FEM framework in prior works (Zecevic et al., 2017; Zecevic and Knezevic, 2017). In the brief summary that follows, the subscript FE implies quantities passed/returned from the FEM software, Abaqus. Every FE integration point of the meshes embeds the same initial texture for ferrite and martensite. The underneath EPSC constitutive law calculates the homogenized stress at the end of every strain increment, $\boldsymbol{\sigma}_{FE}^{t+\Delta t}$, for

a given strain increment, $\Delta \boldsymbol{\varepsilon}_{FE}$, interrogating the model. The applied strain increment is determined by imposed boundary conditions on the mesh. In addition, the implicit FEM solver needs a Jacobian matrix, $\frac{\partial \Delta \boldsymbol{\sigma}_{FE}}{\partial \Delta \boldsymbol{\varepsilon}_{FE}}$, to estimate a displacement field. Accommodated strain by the EPSC model per integration point up to the current time is

$$\boldsymbol{\varepsilon}_{FE}^{t+\Delta t} = \boldsymbol{\varepsilon}_{FE}^{t} + \Delta \boldsymbol{\varepsilon}_{FE}. \tag{21}$$

The Jacobian is (Zecevic and Knezevic, 2019)

$$\frac{\partial \Delta \boldsymbol{\sigma}_{FE}}{\partial \Delta \boldsymbol{\varepsilon}_{FE}} = \frac{\partial (\boldsymbol{\sigma}_{FE}^{t+\Delta t} - \boldsymbol{\sigma}_{FE}^{t})}{\partial \Delta \boldsymbol{\varepsilon}_{FE}} = \frac{\partial \Delta \bar{\boldsymbol{\sigma}}}{\partial \Delta \bar{\boldsymbol{\varepsilon}}} = \frac{\partial (\bar{\mathbf{L}}^{inc} \Delta \bar{\boldsymbol{\varepsilon}})}{\partial \Delta \bar{\boldsymbol{\varepsilon}}} = \bar{\mathbf{L}}^{inc}. \tag{22}$$

where $\bar{\mathbf{L}}^{inc}$ is the stiffness relating the increments in Cauchy stress and strain. The bar on top denotes that variables are in the configuration at the beginning of time increment with respect to the crystal rotation (Zecevic and Knezevic, 2019).

5 Model calibration

The measured axial deformation processes for DP 590, DP 780, and DP 1180 steels are simulated in FE-EPSC using a model in Abaqus consisting of one element, C3D8. The applied boundary conditions were such that the displacement is imposed along the 1-direction (RD) for axial tension/compression and stress-free conditions on the lateral faces. Using the one element model, the hardening parameters for the evolution of slip resistances in ferrite and martensite and for the backstress law in ferrite are adjusted by simulating one cyclic tension-compression-tension curve per steel. The identified parameters were then fine-tuned by comparing another cyclic curve per steel. The remaining data was used for verification. Fig. 5 shows the comparison between measured and predicted curves for the three steels. The model captures the hardening

rates during forward loading, non-linear unloading, BE, permanent softening, and subsequent hardening rates with good accuracy.

The identified parameters for hardening are the initial resistance to slip, τ_0^α, trapping rate coefficient, k_1^α, drag stress, D^α and activation barrier for de-pinning, g^α. The identified parameters for the backstress law are the saturation value for backstress τ_{bs}^{sat}, asymmetry factor, A, and coefficients ν and γ_b. The established parameters are given in Table 3, while the crystal elastic constants are given in Table 4. Importantly, the hardening parameters per phase are the same for every steel, except D^α and the initial content of dislocation density per phase. The initial content of dislocations was estimated from the initial slip resistances, τ_0^α. These initial values include the contribution of the initial dislocation density content. Using the available measured data for dislocation density per phase is DP 1180 (Yaddanapudi et al., 2021), we estimate the friction term of slip resistance, τ_{00}^α by subtracting the contribution of the initial dislocation density from τ_0^α for DP 1180. Using the same estimated friction stress for every steel, we estimated the initial dislocation density per phase in every steel, $\sum_s \rho_{initial}^s$. Evidently, the dislocation densities increase with the content of martensite per steel. The expansion in volume in austenite to martensite phase transformation causes the deformation of ferrite phase and accumulation of dislocations around martensite regions (Calcagnotto et al., 2010; Kadkhodapour et al., 2011). As a result, the content of dislocation density is larger in steels containing more martensite.
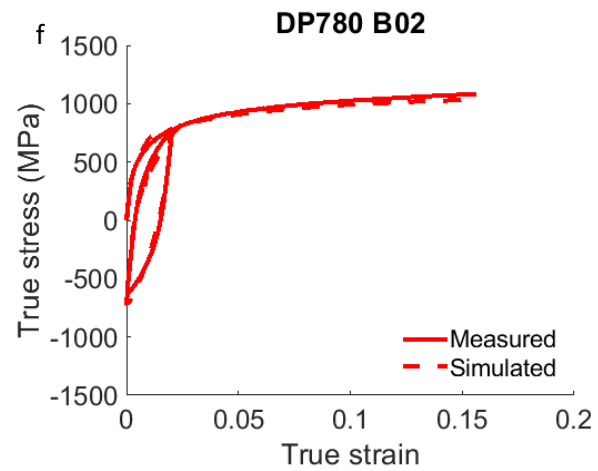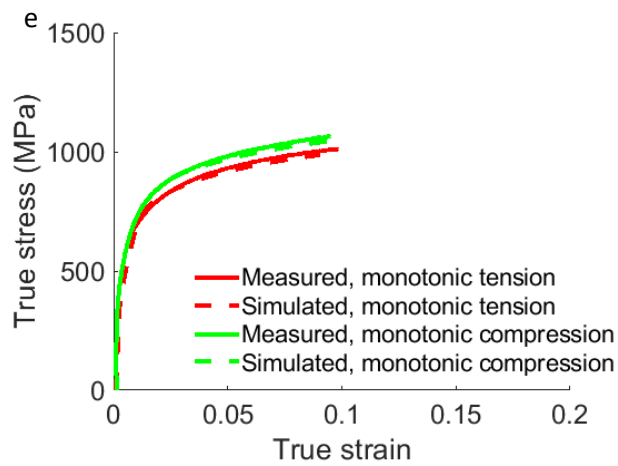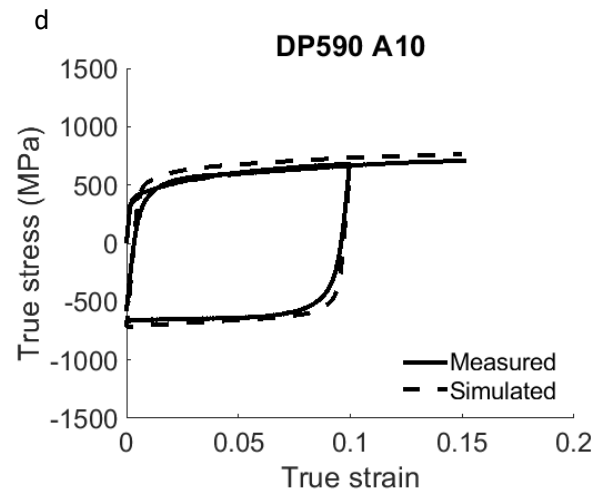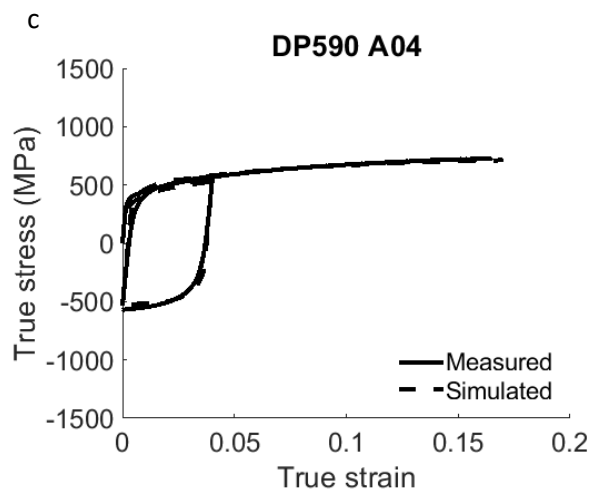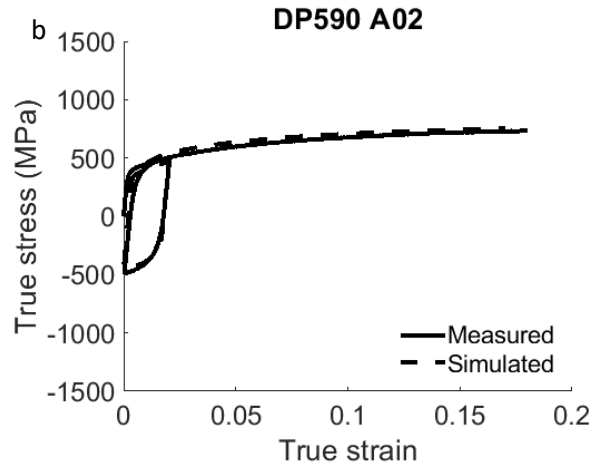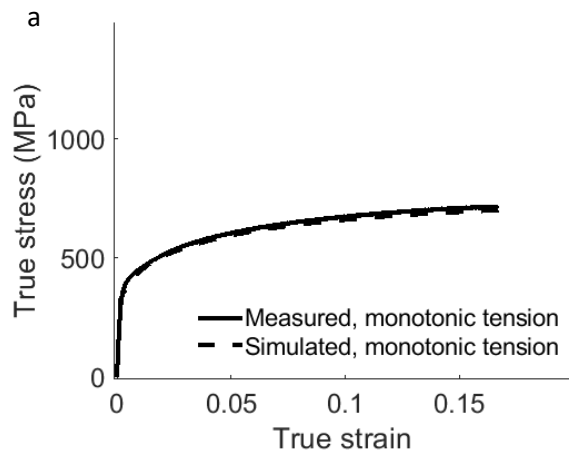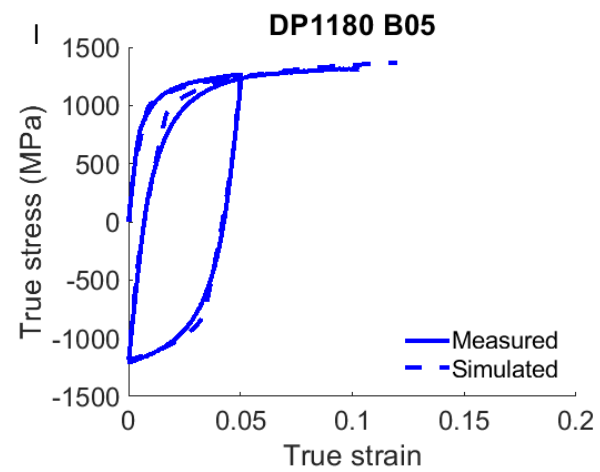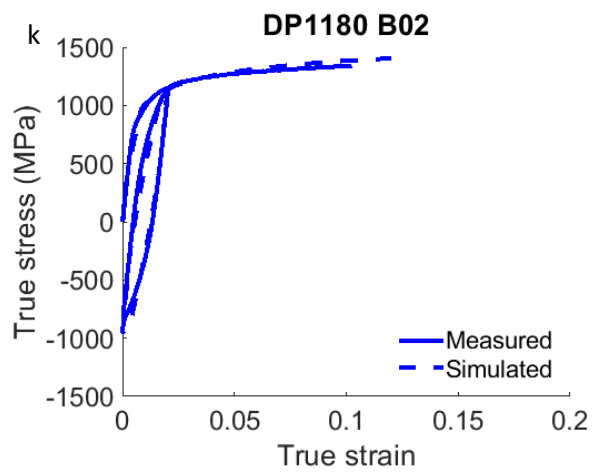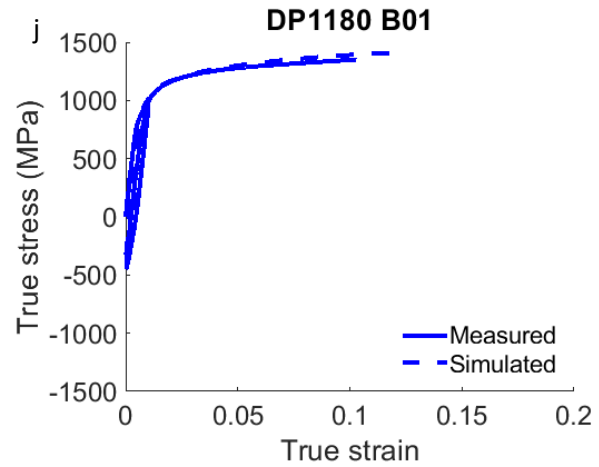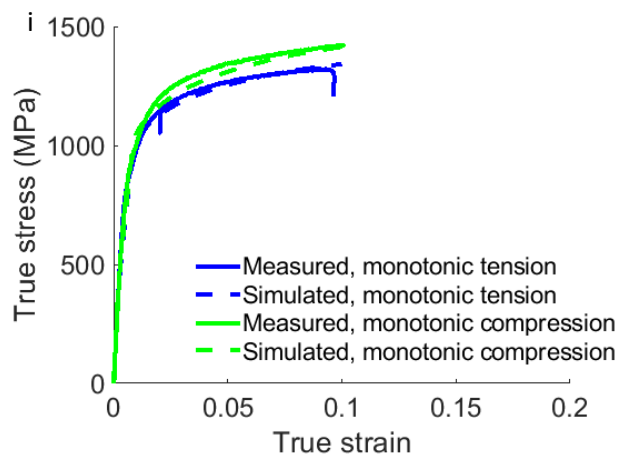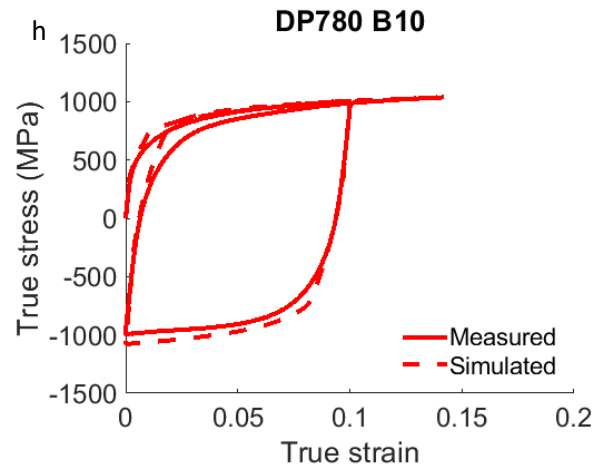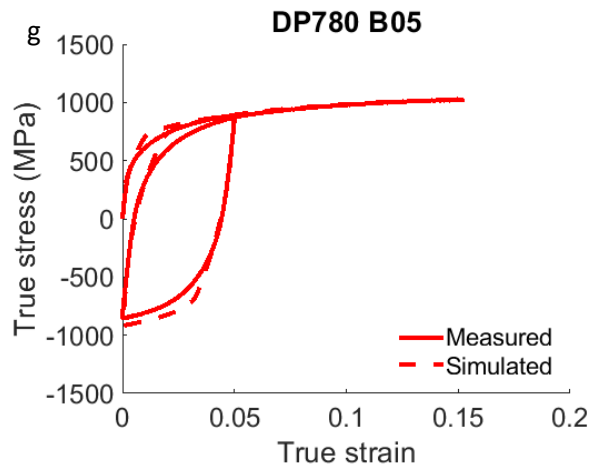
Fig. 5: Simulated and measured true stress-true strain response in monotonic and strain path reversal deformation for DP 590 (a-d), DP 780 (e-h), and DP 1180 (i-l).

Table 3a: Hardening parameters for $\{110\}\langle1\bar{1}1\rangle$ and $\{112\}\langle11\bar{1}\rangle$ slip modes in ferrite (F) and martensite (M) common for all steels. $L^{ss} = 1$ is for self-hardening, while $L^{ss'} = 1.05$ is for latent-hardening interactions (Kocks and Brown, 1966; Zecevic and Knezevic, 2018). The Burgers vector is $b^1 = b^2 = 2.48 \times 10^{-10}$m. The non-Schmid parameters are $c_1 = 0.01$, $c_2 = 0.01$, $c_3 = 0.01$, $c_4 = -0.01$ for all steels. Finally,

Parameter	F	M
$k_1^\alpha [m^{-1}]$	1.5e8	0.725e8
τ_{00}^α [MPa]	110	650
g^α	0.009	0.009
q^α	20	20

Table 3b. Hardening parameters for $\{110\}\langle1\bar{1}1\rangle$ and $\{112\}\langle11\bar{1}\rangle$ slip modes in ferrite (F) and martensite (M) per steel.

Parameter	DP 590 (F)	DP 590 (M)	DP 780 (F)	DP 780 (M)	DP 1180 (F)	DP 1180 (M)
$\sum_s \rho_{initial}^s [m^{-2}]$	1.2e9	4.08e9	3.4e10	5.08e10	3.14e12	1.47e13

τ_0^α [MPa]	110.5	651	112.5	654	136	718
D^α [MPa]	625	700	700	750	750	800

Table 3c. Fitting parameters pertaining to the evolution of backstress in ferrite per steel.

Parameters	DP 590 (F)	DP 780 (F)	DP 1180 (F)
$\tau_{bs}^{sat}[MPa]$	15	45	85
ν	100	100	100
γ_b	0.001	0.009	0.001
A	1	5	2

Table 4: Single crystal elastic stiffness values in GPa for ferrite and martensite taken from (Cantara et al., 2019).

	C_{11}	C_{12}	C_{44}
Ferrite	218.37	113.31	105.34
Martensite	282.31	116.19	78.57

6 Simulation results for hat-shaped draw-bending
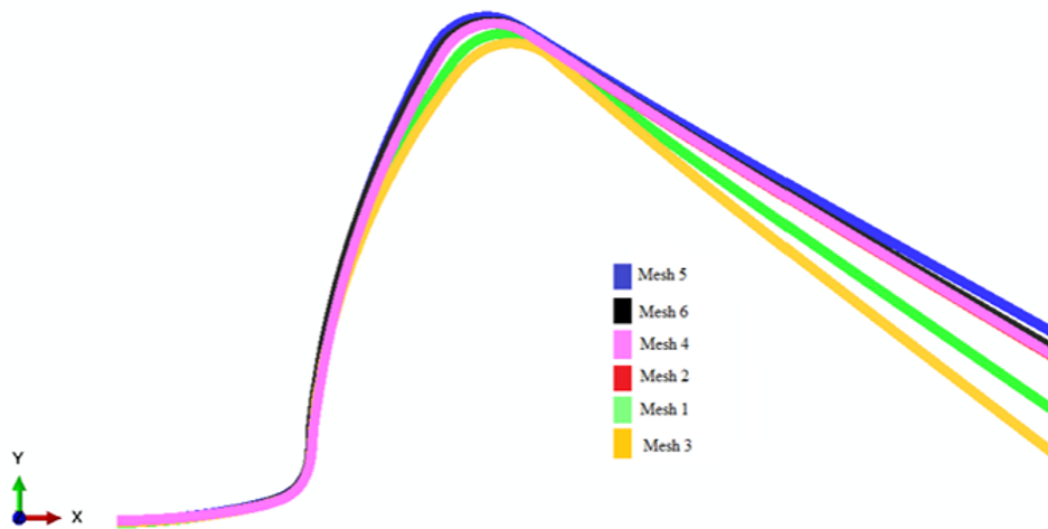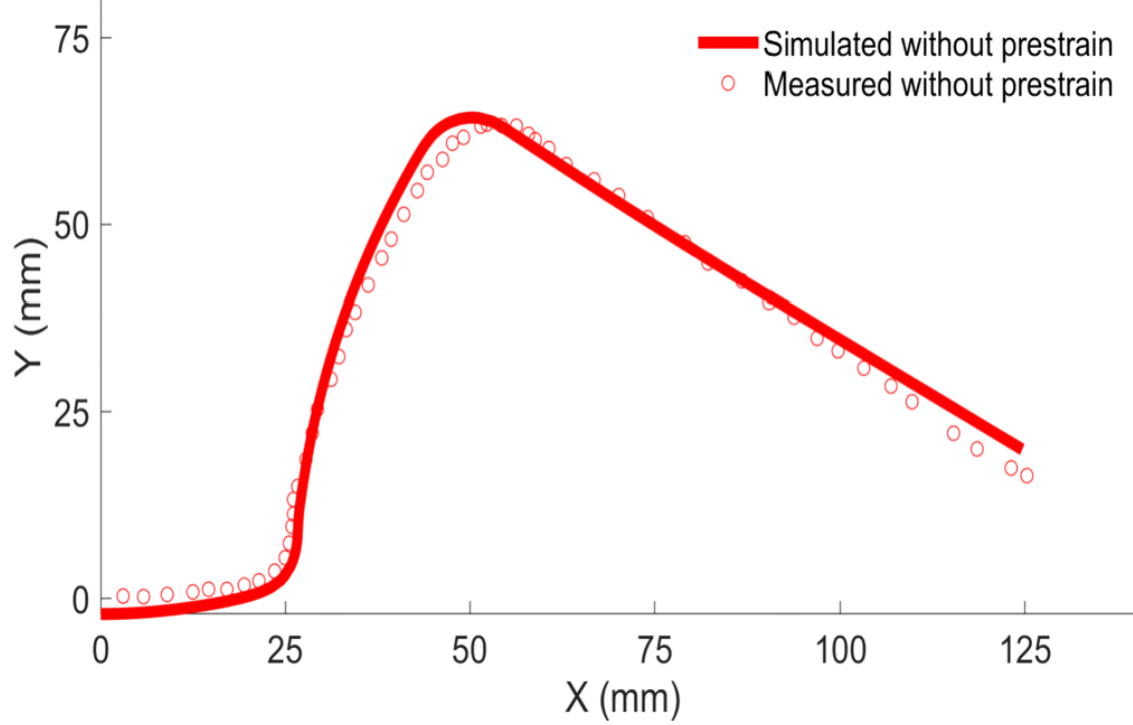
Fig. 6: (a) Effect of mesh on predicted springback for DP 780. (b) Comparison of measured and simulated springback after hat-shaped draw-bending of DP 780. The simulation was performed using mesh 2.

Table 5: FE meshes used for the hat-shaped draw-bending simulations and simulation times.

Mesh #	Element type	# of elements in through thickness	Total # of elements	Simulation time in hours
Mesh 1	CPE4	2	514	78
Mesh 2	CPE4	4	1028	96
Mesh 3	CPE4R	2	514	59
Mesh 4	CPE4R	4	1028	72
Mesh 5	CPE8R	2	514	84
Mesh 6	CPE8R	4	1028	102
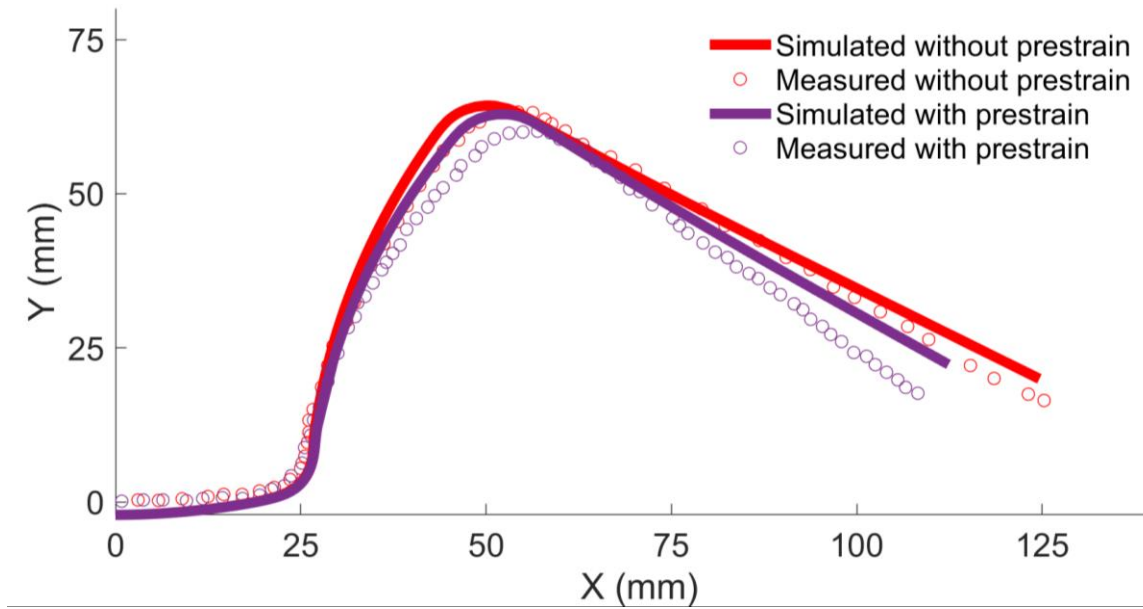
Fig. 7: Comparison of measured and simulated springback after hat-shaped draw-bending of DP 780 with specimen pre-strained axially in tension to 7.8%. The results from Fig. 6b are shown for reference. The simulations were performed using mesh 2.

a
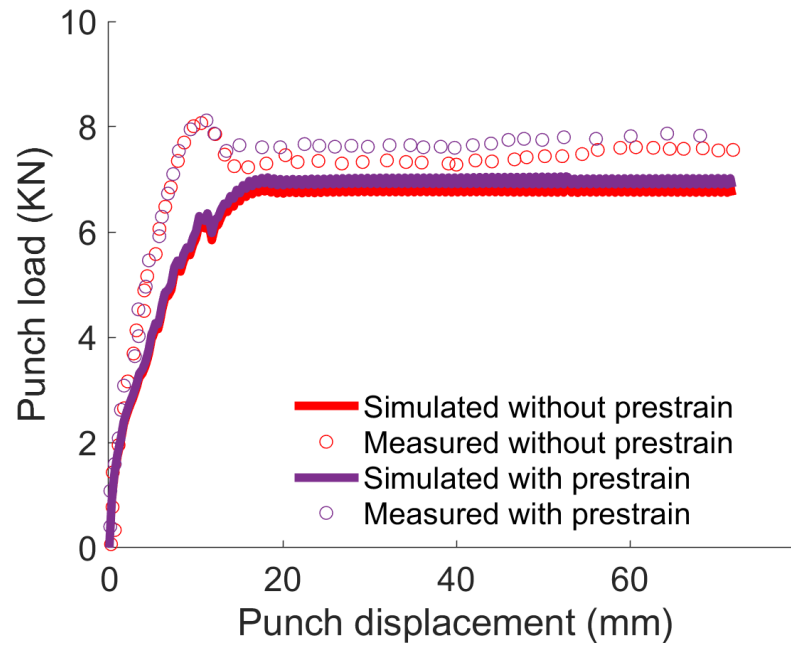
Fig. 8: Comparison of measured and simulated punch load vs punch displacement in hat-shaped

draw-bending tests, simulated with mesh 2 for DP 780, where the final displacement of the

punch was 71.8 mm.

Fig. 9: Contours of von Mises stress and effective strain after the springback for DP 590, DP 780, and DP 1180 simulated using mesh 2. Evidently the steels show different springback effect after the hat-shaped draw-bending processing.
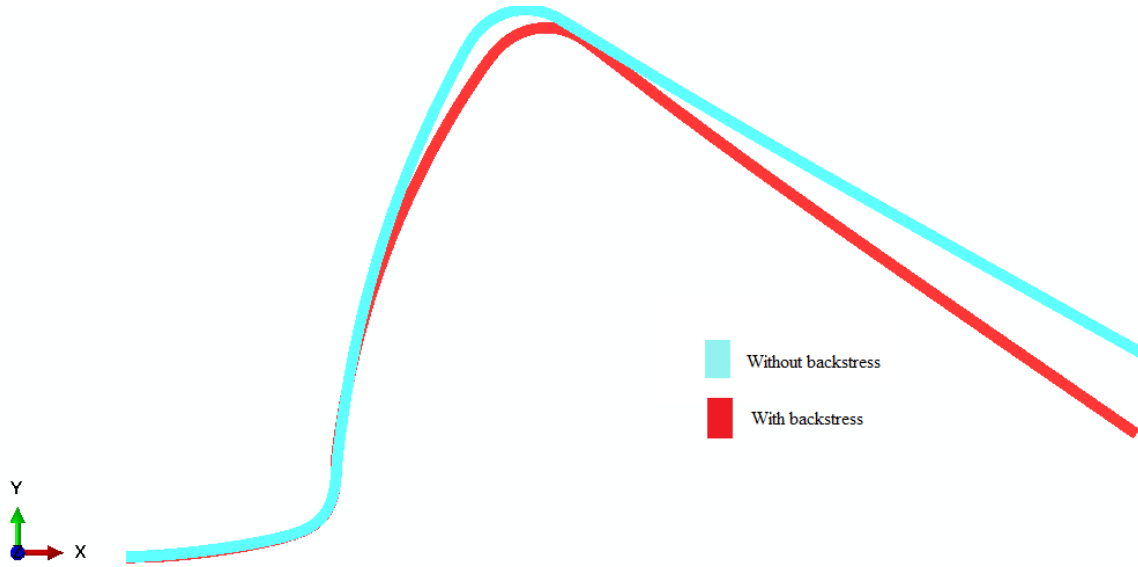
Fig. 10: Comparison of hat-shaped draw-bending simulation results for DP 780 using mesh 2 with and without accounting for backstress.

7 Summary and conclusions

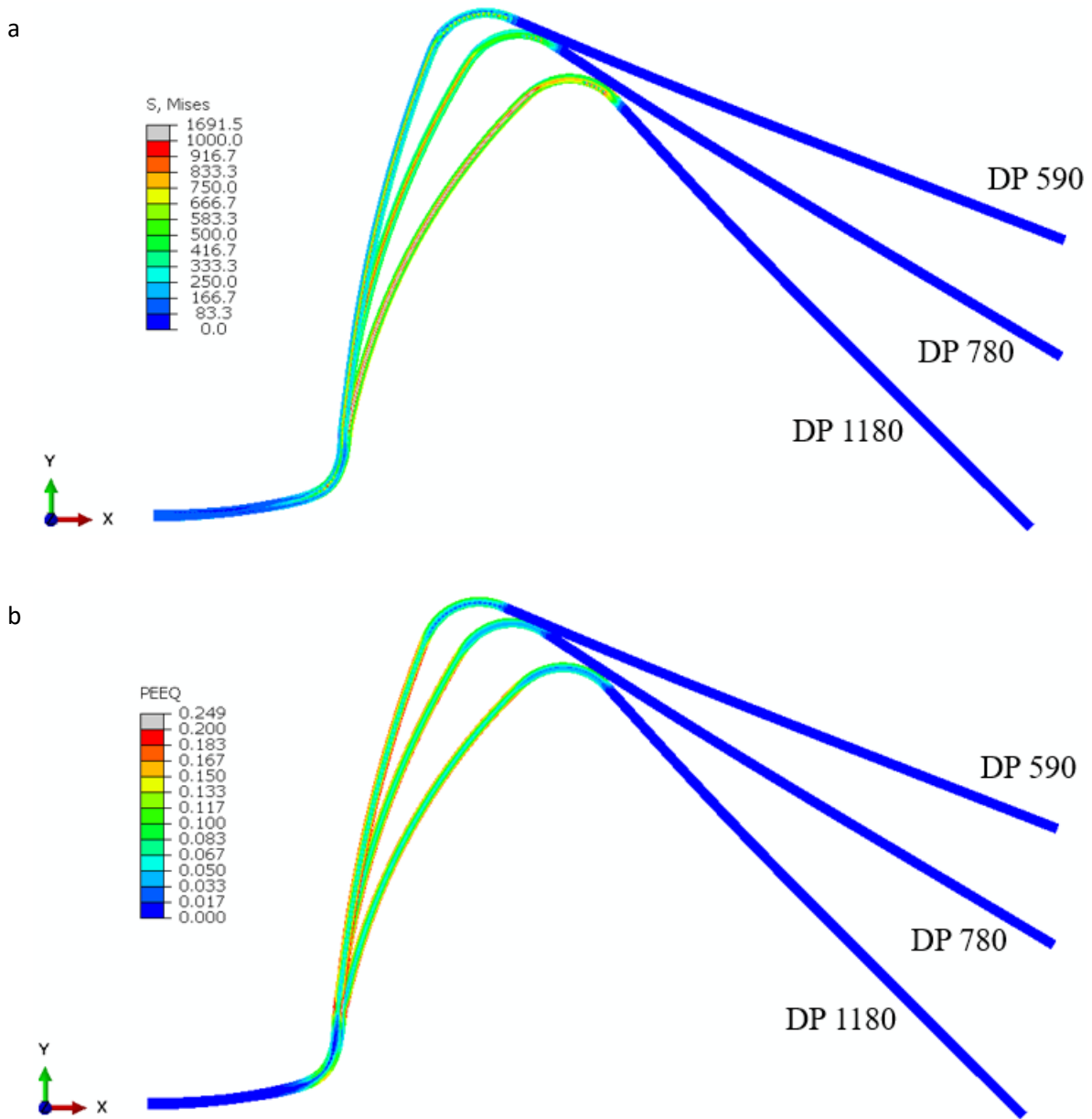In this work, a multi-level modeling framework linking the single crystal-level response to polycrystalline aggregate-level response to the component-level response is used to simulate hat-shaped draw-bending and b-pillar stamping. The crystal-level response is governed by sub-models including a strain-path sensitive hardening law for the evolution of dislocation density and a slip system-level kinematic hardening law for back-stress. The polycrystal model is the EPSC formulation homogenizing crystal-level responses of two-phases. The EPSC model is coupled with the implicit FEM to form the FE-EPSC framework in which every integration point of an FE mesh is a polycrystal that deforms by anisotropic elasticity and plastic slip allowing for the heterogeneous deformation across a sample as a result of geometry, boundary conditions, and

133

material anisotropy. A comprehensive set of monotonic and load reversal true stress-true strain curves for DP 590, DP 780, and DP 1180 was used to calibrate and then critically validate FE-EPSC using one element simulations. It was shown that the model successfully captures the flow response of the steels using a single set of parameters per phase except for one parameter, which varied from steel to steel. In particular, the model reproduced the phenomena pertaining to the load reversal deformation, the typical decreasing hardening rate during forward tension, a linear and then a non-linear unloading, followed by the BE, and a slight shift in the hardening rate during continuous straining. Such good performances of the model were primarily a consequence of accounting for kinematic hardening at the slip system-level through the evolution law for backstress, inter-granular stresses, and dislocation generation and annihilation during strain-path reversals.

As capturing the phenomena pertaining to the load reversal deformation have major implications on the accuracy of simulations in the sheet metal forming, the calibrated model is further evaluated on a case study of hat-shaped draw-bending of DP steels. The objective was to predict the final geometry of the part after the draw-bending and subsequent springback/unloading, consistent with experimental measurements available for DP 780. The dimensional changes of the part in the free state were successfully predicted. Comparison of the experimentally measured and predicted geometry revealed that accounting for backstress is essential for the accurate prediction of the part. Subsequently, the same hat-shaped draw-bending process was simulated for a pre-strained sheet of DP 780 revealing the role of strain hardening in predicting the part geometry. Finally, the same process was simulated for DP 590 and DP 1180 to further confirm the increase in the level of deflection with strength. The work has shown that the FE-EPSC simulation framework can be used to predict phenomena pertaining to material

behavior and resulting geometrical changes important for optimizing sheet metal forming

processes. Future work will focus on lessening the computational time requirements by taking

advantage of specialized high performance computing hardware to make the model more

practical.

Acknowledgments

References

Abel, A., 1987. Historical perspectives and some of the main features of the Bauschinger effect, Materials Forum. Institute of Metals and Materials Australasia, pp. 11-26.
Armstrong, P.J., Frederick, C.O., 1966. A mathematical representation of multiaxial Bauschinger effect. Berkeley nuclear laboratories.
Barrett, T.J., Takagi, S., Islam, N., Kuwabara, T., Hassan, T., Kinsey, B.L., Knezevic, M., Korkolis, Y.P., 2020. Material modeling and simulation of continuous-bending-under-tension of AA6022-T4. Journal of Materials Processing Technology, 116658.
Bathe, K.-J., 1996. Finite element procedures. Englewood Cliffs, N.J.: Prentice Hall.
Beyerlein, I.J., Tomé, C.N., 2008. A dislocation-based constitutive law for pure Zr including temperature effects. Int. J. Plast. 24, 867-895.
Bhargava, M., Chakrabarty, S., Barnwal, V.K., Tewari, A., Mishra, S.K., 2018. Effect of microstructure evolution during plastic deformation on the formability of Transformation Induced Plasticity and Quenched & Partitioned AHSS. Mater. Des. 152, 65-77.
Bhattacharyya, A., Knezevic, M., Abouaf, M., 2015. Characterization of Crystallographic Texture and Intra-Grain Morphology in Cross-Rolled Tantalum. Metall. Mater. Trans. A 46, 1085-1096.
Boger, R., Wagoner, R., Barlat, F., Lee, M., Chung, K., 2005. Continuous, large strain, tension/compression testing of sheet material. Int. J. Plast. 21, 2319-2343.
Brown, L.M., Stobbs, W.M., 1971. The Work-Hardening of Copper-Silica: I. A Model Based on Internal Stresses, With No Plastic Relaxation. Philosophical Magazine 23, 1185–1199.
Calcagnotto, M., Adachi, Y., Ponge, D., Raabe, D., 2011. Deformation and fracture mechanisms in fine- and ultrafine-grained ferrite/martensite dual-phase steels and the effect of aging. Acta. Mater. 59, 658-670.
Calcagnotto, M., Ponge, D., Demir, E., Raabe, D., 2010. Orientation gradients and geometrically necessary dislocations in ultrafine grained dual-phase steels studied by 2D and 3D EBSD. Materials Science and Engineering: A 527, 2738-2746.

Calcagnotto, M., Ponge, D., Raabe, D., 2012. Microstructure control during fabrication of ultrafine grained dual-phase steel: characterization and effect of intercritical annealing parameters. ISIJ international 52, 874-883.

Cantara, A.M., Zecevic, M., Eghtesad, A., Poulin, C.M., Knezevic, M., 2019. Predicting elastic anisotropy of dual-phase steels based on crystal mechanics and microstructure. International Journal of Mechanical Sciences 151, 639-649.

Chaboche, J., Rousselier, G., 1983. On the plastic and viscoplastic constitutive equations—Part I: Rules developed with internal variable concept. Journal of Pressure Vessel Technology 105, 153-158.

Chaboche, J.L., 1977. Viscoplastic constitutive equations for the description of cyclic and ansiotropic behavior of metals, In: XVIIth Polish solid mechanics conference, Bulletin de l'Académie Polonaise des Sciences, Série Sciences et Techniques, pp. 33-41.

Chaboche, J.L., 2008. A review of some plasticity and viscoplasticity constitutive theories. Int. J. Plast. 24, 1642-1693.

Chun, B.K., Jinn, J.T., Lee, J.K., 2002. Modeling the Bauschinger effect for sheet metals, part I: theory. Int. J. Plast. 18, 571-595.

Dao, M., Asaro, R.J., 1993. Non-Schmid effects and localized plastic flow in intermetallic alloys. Mater. Sci. Eng. A 170, 143-160.

Daroju, S., Kuwabara, T., Knezevic, M., 2022. Experimental characterization and crystal plasticity modeling of dual-phase steels subjected to strain path reversals. Mechanics of Materials.

Demir, E., Raabe, D., 2010. Mechanical and microstructural single-crystal Bauschinger effects: Observation of reversible plasticity in copper during bending. Acta. Mater. 58, 6055-6063.

Deng, N., Kuwabara, T., Korkolis, Y.P., 2015. On the non-linear unloading behavior of a biaxially loaded dual-phase steel sheet. (in preparation).

Dotsenko, V.I., 1979. Stress Relaxation in Crystals. physica status solidi (b) 93, 11-43.

Eghtesad, A., Barrett, T.J., Knezevic, M., 2018. Compact reconstruction of orientation distributions using generalized spherical harmonics to advance large-scale crystal plasticity modeling: Verification using cubic, hexagonal, and orthorhombic polycrystals. Acta. Mater. 155, 418-432.

Eshelby, J.D., 1957. The determination of the elastic field of an ellipsoidal inclusion, and related problems. Proc R. Soc. Lond. A 241, 376-396.

Feng, Z., Yoon, S.-Y., Choi, J.-H., Barrett, T.J., Zecevic, M., Barlat, F., Knezevic, M., 2020. A comparative study between elasto-plastic self-consistent crystal plasticity and anisotropic yield function with distortional hardening formulations for sheet metal forming. Mechanics of Materials 148, 103422.

Franciosi, P., Zaoui, A., 1982. Multislip in f.c.c. crystals a theoretical approach compared with experimental data. Acta Metallurgica 30, 1627-1637.

Ghaei, A., Green, D.E., Aryanpour, A., 2015. Springback simulation of advanced high strength steels considering nonlinear elastic unloading–reloading behavior. Mater. Des. 88, 461-470.

Ghorbanpour, S., Alam, M.E., Ferreri, N.C., Kumar, A., McWilliams, B.A., Vogel, S.C., Bicknell, J., Beyerlein, I.J., Knezevic, M., 2020. Experimental characterization and crystal plasticity modeling of anisotropy, tension-compression asymmetry, and texture evolution of additively manufactured Inconel 718 at room and elevated temperatures. Int. J. Plast. 125, 63-79.

Ghorbanpour, S., Zecevic, M., Kumar, A., Jahedi, M., Bicknell, J., Jorgensen, L., Beyerlein, I.J., Knezevic, M., 2017. A crystal plasticity model incorporating the effects of precipitates in

superalloys: Application to tensile, compressive, and cyclic deformation of Inconel 718. Int. J. Plast. 99, 162-185.

Gong, H., Wang, S., Knysh, P., Korkolis, Y.P., 2016. Experimental investigation of the mechanical response of laser-welded dissimilar blanks from advanced- and ultra-high-strength steels. Mater. Des. 90, 1115-1123.

Gough, H., Hanson, D., Wright, S., 1927. The Behaviour of Single Crystals of Aluminium under Static and Repeated Stresses. Philosophical Transactions of the Royal Society of London. Series A, Containing Papers of a Mathematical or Physical Character, 1-30.

Harder, J., 1999. A crystallographic model for the study of local deformation processes in polycrystals. Int. J. Plast. 15, 605-624.

Holscher, M., Raabe, D., Lucke, K., 1994. Relationship between rolling textures and shear textures in F.C.C. and B.C.C. metals. Acta Metall. Mater. 42, 879-886.

Hosford, W.F., Caddell, R.M., 1993. Metal forming mechanics and metallurgy. Prentice-Hall, Inc.

Hu, Z., Rauch, E.F., Teodosiu, C., 1992. Work-hardening behavior of mild steel under stress reversal at large strains. Int. J. Plast. 8, 839-856.

Kadkhodapour, J., Schmauder, S., Raabe, D., Ziaei-Rad, S., Weber, U., Calcagnotto, M., 2011. Experimental and numerical study on geometrically necessary dislocations and non-homogeneous mechanical properties of the ferrite phase in dual phase steels. Acta Materialia 59, 4387-4394.

Kassner, M.E., Geantil, P., Levine, L.E., 2013. Long range internal stresses in single-phase crystalline materials. International Journal of Plasticity 45, 44-60.

Khadyko, M., Dumoulin, S., Cailletaud, G., Hopperstad, O.S., 2016. Latent hardening and plastic anisotropy evolution in AA6060 aluminium alloy. Int. J. Plast. 76, 51-74.

Kitayama, K., Tomé, C.N., Rauch, E.F., Gracio, J.J., Barlat, F., 2013a. A crystallographic dislocation model for describing hardening of polycrystals during strain path changes. Application to low carbon steels. International Journal of Plasticity 46, 54-69.

Kitayama, K., Tomé, C.N., Rauch, E.F., Gracio, J.J., Barlat, F., 2013b. A crystallographic dislocation model for describing hardening of polycrystals during strain path changes. Application to low carbon steels. International Journal of Plasticity in press.

Knezevic, M., Beyerlein, I.J., Lovato, M.L., Tomé, C.N., Richards, A.W., McCabe, R.J., 2014. A strain-rate and temperature dependent constitutive model for BCC metals incorporating non-Schmid effects: Application to tantalum–tungsten alloys. Int. J. Plast. 62, 93-104.

Knezevic, M., McCabe, R.J., Lebensohn, R.A., Tomé, C.N., Liu, C., Lovato, M.L., Mihaila, B., 2013. Integration of self-consistent polycrystal plasticity with dislocation density based hardening laws within an implicit finite element framework: Application to low-symmetry metals. J. Mech. Phys. Solids 61, 2034-2046.

Knezevic, M., Poulin, C.M., Zheng, X., Zheng, S., Beyerlein, I.J., 2019. Strengthening of alloy AA6022-T4 by continuous bending under tension. Mater. Sci. Eng. A 758, 47-55.

Knezevic, M., Zecevic, M., Beyerlein, I.J., Bhattacharyya, A., McCabe, R.J., 2015. Predicting Texture Evolution in Ta and Ta-10W Alloys Using Polycrystal Plasticity. JOM 67, 2670-2674.

Knockaert, R., Chastel, Y., Massoni, E., 2000. Rate-independent crystalline and polycrystalline plasticity, application to FCC materials. International Journal of Plasticity 16, 179-198.

Kocks, U.F., Brown, T.J., 1966. Latent hardening in aluminum. Acta Metall. 14, 87-98.

Kocks, U.F., Franciosi, P., Kawai, M., 1991. A Forest Model of Latent Hardening and its Application to Polycrystal Deformations. Textures and Microstructures 14, 1103-1114.

Kocks, U.F., Tomé, C.N., Wenk, H.-R., 1998. Texture and Anisotropy. Cambridge University Press, Cambridge, UK.

Kruml, T., Coddet, O., Martin, J., 2008. About the determination of the thermal and athermal stress components from stress-relaxation experiments. Acta. Mater. 56, 333-340.

Kudzal, A.D., McWilliams, B.A., Taggart-Scarff, J., Knezevic, M., 2020. Fabrication of a low alloy ultra-high strength (>1500 MPa yield) steel using powder bed fusion additive manufacturing. Mater. Sci. Eng. A 770, 138512.

Lavrentev, F.F., 1980. The type of dislocation interaction as the factor determining work hardening. Materials Science and Engineering 46, 191-208.

Lee, J.-Y., Lee, J.-W., Lee, M.-G., Barlat, F., 2012. An application of homogeneous anisotropic hardening to springback prediction in pre-strained U-draw/bending. International Journal of Solids and Structures 49, 3562-3572.

Lee, M., Kim, C., Pavlina, E., Barlat, F., 2011. Advances in sheet forming—materials modeling, numerical simulation, and press technologies. Journal of manufacturing science and engineering 133.

Li, K., Carden, W., Wagoner, R., 2002. Simulation of springback. International Journal of Mechanical Sciences 44, 103-122.

Lim, H., Weinberger, C.R., Battaile, C.C., Buchheit, T.E., 2013. Application of generalized non-Schmid yield law to low-temperature plasticity in bcc transition metals. Modelling and Simulation in Materials Science and Engineering 21, 045015.

Lipinski, P., Berveiller, M., 1989. Elastoplasticity of micro-inhomogeneous metals at large strains. Int. J. Plast. 5, 149-172.

Ma, B., Liu, Z.G., Jiang, Z., Wu, X., Diao, K., Wan, M., 2016. Prediction of forming limit in DP590 steel sheet forming: An extended fracture criterion. Mater. Des. 96, 401-408.

McDowell, D.L., 1992. A nonlinear kinematic hardening theory for cyclic thermoplasticity and thermoviscoplasticity. Int. J. Plast. 8, 695-728.

Mecking, H., Kocks, U.F., 1981. Kinetics of flow and strain-hardening. Acta Metall. Mater. 29, 1865-1875.

Mohebbi, M.S., Akbarzadeh, A., Yoon, Y.-O., Kim, S.-K., 2015. Stress relaxation and flow behavior of ultrafine grained AA 1050. Mechanics of Materials 89, 23-34.

Mompiou, F., Caillard, D., Legros, M., Mughrabi, H., 2012. In situ TEM observations of reverse dislocation motion upon unloading in tensile-deformed UFG aluminium. Acta. Mater. 60, 3402-3414.

Mughrabi, H., 1983. Dislocation wall and cell structures and long-range internal stresses in deformed metal crystals. Acta Metall. 31, 1367-1379.

Nagtegaal, J.C., Veldpaus, F.E., 1984. On the implementation of finite strain plasticity equations in a numerical model. Numerical methods in industrial forming processes, 351-371.

Neil, C.J., Wollmershauser, J.A., Clausen, B., Tomé, C.N., Agnew, S.R., 2010. Modeling lattice strain evolution at finite strains and experimental verification for copper and stainless steel using in situ neutron diffraction. Int. J. Plast. 26, 1772-1791.

Nesterova, E.V., Bouvier, S., Bacroix, B., 2015. Microstructure evolution and mechanical behavior of a high strength dual-phase steel under monotonic loading. Materials Characterization 100, 152-162.

Nieh, T.G., Nix, W.D., 1986. Unloading yield effects in aluminum alloys. Metallurgical transactions. A, Physical metallurgy and materials science 17 A, 121-126.

Pavlina, E., Lee, M.-G., Barlat, F., 2015. Observations on the Nonlinear Unloading Behavior of Advanced High Strength Steels. Metall. Mater. Trans. A 46, 18-22.

Poulin, C.M., Barrett, T.J., Knezevic, M., 2020a. Inferring Post-Necking Strain Hardening Behavior of Sheets by a Combination of Continuous Bending Under Tension Testing and Finite Element Modeling. Experimental Mechanics 60, 459-473.

Poulin, C.M., Korkolis, Y.P., Kinsey, B.L., Knezevic, M., 2019. Over five-times improved elongation-to-fracture of dual-phase 1180 steel by continuous-bending-under-tension. Mater. Des. 161, 95-105.

Poulin, C.M., Vogel, S.C., Korkolis, Y.P., Kinsey, B.L., Knezevic, M., 2020b. Experimental studies into the role of cyclic bending during stretching of dual-phase steel sheets. International Journal of Material Forming 13, 393-408.

Rabahallah, M., Bouvier, S., Balan, T., Bacroix, B., 2009. Numerical simulation of sheet metal forming using anisotropic strain-rate potentials. Mater. Sci. Eng. A 517, 261-275.

Savage, D.J., Beyerlein, I.J., Knezevic, M., 2017. Coupled texture and non-Schmid effects on yield surfaces of body-centered cubic polycrystals predicted by a crystal plasticity finite element approach. International Journal of Solids and Structures 109, 22-32.

Savage, D.J., Chandola, N., Cazacu, O., McWilliams, B.A., Knezevic, M., 2018. Validation of recent analytical dilatational models for porous polycrystals using crystal plasticity finite element models with Schmid and non-Schmid activation laws. Mechanics of Materials 126, 148-162.

Sharma, R., Poulin, C.M., Knezevic, M., Miles, M.P., Fullwood, D.T., 2021. Micromechanical origins of remarkable elongation-to-fracture in AHSS TRIP steels via continuous bending under tension. Mater. Sci. Eng. A 825, 141876.

Smith, A., Chen, Z., Lee, J.Y., Lee, M.G., Wagoner, R.H., 2014. Effective method for fitting complex constitutive equations. Int. J. Plast. 58, 100-119.

Sritharan, T., Chandel, R.S., 1997. Phenomena in interrupted tensile tests of heat treated aluminium alloy 6061. Acta. Mater. 45, 3155-3161.

Stout, M., Rollett, A., 1990. Large-strain Bauschinger effects in fcc metals and alloys. Metall. Mater. Trans. A 21, 3201-3213.

Tasan, C.C., Hoefnagels, J.P.M., Diehl, M., Yan, D., Roters, F., Raabe, D., 2014. Strain localization and damage in dual phase steels investigated by coupled in-situ deformation experiments and crystal plasticity simulations. Int. J. Plast. 63, 198-210.

Taupin, V., Pesci, R., Berbenni, S., Berveiller, S., Ouahab, R., Bouaziz, O., 2013. Lattice strain measurements using synchrotron diffraction to calibrate a micromechanical modeling in a ferrite–cementite steel. Materials Science and Engineering: A 561, 67-77.

Teodosiu, C., Raphanel, J.L., 1991. Finite element simulations of large elastoplastic deformations of multicrystals. Proceedings of the International Seminar MECAMAT91, 153-168.

Turner, P.A., Tomé, C.N., 1994. A study of residual stresses in Zircaloy-2 with rod texture. Acta Metall. Mater. 42, 4143-4153.

Verma, R.K., Kuwabara, T., Chung, K., Haldar, A., 2011. Experimental evaluation and constitutive modeling of non-proportional deformation for asymmetric steels. Int. J. Plast. 27, 82-101.

Wagoner, R.H., Lim, H., Lee, M.-G., 2013. Advanced Issues in springback. Int. J. Plast. 45, 3-20.

Wen, W., Borodachenkova, M., Tomé, C.N., Vincze, G., Rauch, E.F., Barlat, F., Grácio, J.J., 2015. Mechanical behavior of Mg subjected to strain path changes: Experiments and modeling. International Journal of Plasticity 73, 171-183.

Wilson, D.V., Zandrahimi, M., Roberts, W.T., 1990. Effects of changes in strain path on work-hardening in CP aluminium and an Al-Cu-Mg alloy. Acta Metall. Mater. 38, 215-226.

Wollmershauser, J.A., Clausen, B., Agnew, S.R., 2012. A slip system-based kinematic hardening model application to in situ neutron diffraction of cyclic deformation of austenitic stainless steel. Int. J. Fatigue 36, 181-193.

Woo, W., Em, V.T., Kim, E.Y., Han, S.H., Han, Y.S., Choi, S.H., 2012. Stress–strain relationship between ferrite and martensite in a dual-phase steel studied by in situ neutron diffraction and crystal plasticity theories. Acta. Mater. 60, 6972-6981.

Yaddanapudi, K., Knezevic, M., Mahajan, S., Beyerlein, I.J., 2021. Plasticity and structure evolution of ferrite and martensite in DP 1180 during tension and cyclic bending under tension to large strains. Mater. Sci. Eng. A 820, 141536.

Yoshida, F., Uemori, T., Fujiwara, K., 2002. Elastic–plastic behavior of steel sheets under in-plane cyclic tension–compression at large strain. Int. J. Plast. 18, 633-659.

Yoshida, T., Isogai, E., Sato, K., Hashimoto, K., 2013. Springback Problems in Forming of High-Strength Steel Sheets and Countermeasures.

Zecevic, M., Beyerlein, I.J., Knezevic, M., 2017. Coupling elasto-plastic self-consistent crystal plasticity and implicit finite elements: Applications to compression, cyclic tension-compression, and bending to large strains. Int. J. Plast. 93, 187-211.

Zecevic, M., Knezevic, M., 2017. Modeling of Sheet Metal Forming Based on Implicit Embedding of the Elasto-Plastic Self-Consistent Formulation in Shell Elements: Application to Cup Drawing of AA6022-T4. JOM 69, 922-929.

Zecevic, M., Knezevic, M., 2018. Latent hardening within the elasto-plastic self-consistent polycrystal homogenization to enable the prediction of anisotropy of AA6022-T4 sheets. Int. J. Plast. 105, 141-163.

Zecevic, M., Knezevic, M., 2019. An implicit formulation of the elasto-plastic self-consistent polycrystal plasticity model and its implementation in implicit finite elements. Mechanics of Materials 136, 103065.

Zecevic, M., Knezevic, M., Beyerlein, I.J., McCabe, R.J., 2016a. Texture formation in orthorhombic alpha-uranium under simple compression and rolling to high strains. Journal of Nuclear Materials 473, 143-156.

Zecevic, M., Knezevic, M., Beyerlein, I.J., Tomé, C.N., 2015. An elasto-plastic self-consistent model with hardening based on dislocation density, twinning and de-twinning: Application to strain path changes in HCP metals. Mater. Sci. Eng. A 638, 262-274.

Zecevic, M., Korkolis, Y.P., Kuwabara, T., Knezevic, M., 2016b. Dual-phase steel sheets under cyclic tension–compression to large strains: Experiments and crystal plasticity modeling. J. Mech. Phys. Solids 96, 65-87.

Zecevic, M., Upadhyay, M.V., Polatidis, E., Panzner, T., Van Swygenhoven, H., Knezevic, M., 2019. A crystallographic extension to the Olson-Cohen model for predicting strain path dependence of martensitic transformation. Acta. Mater. 166, 386-401.